Imperial College London

Instrument Tracking and Navigation for MRI-guided Interventions

Francesca Galassi

A thesis submitted in fulfillment of the requirements for the degree of Doctor of Philosophy

in the

Faculty of Engineering
Department of Mechanical Engineering

Declaration of Authorship

I, Francesca Galassi, declare that this thesis titled *Instrument Tracking and Navigation for MRI-guided Interventions* and the work presented in it are my own. I confirm that:

- This work was done wholly or mainly while in candidature for a research degree at this University.
- Where any part of this thesis has previously been submitted for a degree or any other qualification at this University or any other institution, this has been clearly stated.
- Where I have consulted the published work of others, this is always clearly attributed.
- Where I have quoted from the work of others, the source is always given. With the exception of such quotations, this thesis is entirely my own work.
- I have acknowledged all main sources of help.
- Where the thesis is based on work done by myself jointly with others, I have made clear exactly what was done by others and what I have contributed myself.

Copyright Declaration

The copyright of this thesis rests with the author and is made available under a Creative Commons Attribution Non-Commercial No Derivatives licence. Researchers are free to copy, distribute or transmit the thesis on the condition that they attribute it, that they do not use it for commercial purposes and that they do not alter, transform or build upon it. For any reuse or redistribution, researchers must make clear to others the licence terms of this work.

Abstract

Interventional MRI requires accurate and fast localization of medical instruments within the imaging volume of the MR scanner. Furthermore, in view of tissue motion and target dislocation, accurate intra-operative imaging is demanded. The research presented in this thesis addresses these issues with reference to a proposed MRI-guided transrectal prostate biopsy system.

As the instrument is not visible in the MR images, RF fiducial markers embedded within the instrument are used to determine its pose. A novel localization method to compute the location of N fiducial markers using 1D projections is presented. The method is shown to yield significant improvements over previously proposed methods. Computational complexity was significantly reduced by avoiding cluster analysis, while high accuracy was achieved by using a set of optimally chosen projections and by applying Gaussian interpolation in peak detection. The method was analyzed and validated using a combination of experiments and Monte Carlo simulations. Experiments in 1.5 T and 2.9 T MR scanners involved both water phantoms and volunteer subjects. High robustness and sub-pixel accuracy were demonstrated while the computational time showed an improvement of up to a factor of 100 over existing solutions.

This method was employed as the basis for tracking the endorectal probe during the prostate biopsy procedure. The probe was positioned by means of a remotely actuated manipulator. Miniature semiactive markers were embedded within the probe in a rigid known geometrical configuration and tracked by means of the localization method. At each position, Least-Squares fitting of the probe model with the localized one was performed in order to achieve more accurate tracking. Navigation of the probe and biopsy needle was realized through a dedicated graphical user interface. This interface displayed interpolated cross sections through the MR imaging volume and simplified graphical models of the instruments overlaid on the anatomy. Visual guidance was further improved by filtering of the markers' positions, which was enabled by the high tracking rate.

In order to improve intra-operative imaging a novel external receiver array was designed and a prototype was built, as an alternative to the more conventional endorectal and pelvic receivers. This new array coil was optimized for imaging of the prostatic area for a patient in the prone position by combining a butterfly coil and three single trapezoidal loops. The design is suitable for positioning the endorectal probe and does not introduce any spatial limitation to the range of movements. Experiments in a 1.5 T MR scanner and simulations demonstrated higher receiver sensitivity and homogeneity than conventional coils and also a significantly improved signal-to-noise ratio.

Contents

Declaration of Authorship 1

Copyright Declaration 2

Abstract 3

List of Figures 8

List of Tables 11

Acknowledgements 12

1 Introduction 15
- 1.1 The context of the research . . . 15
- 1.2 Research motivation . . . 16
- 1.3 Research outline . . . 17
  - 1.3.1 Instrument tracking and registration . . . 17
  - 1.3.2 Visualization and instrument guidance . . . 18
  - 1.3.3 Optimized receiver coil . . . 19
  - 1.3.4 Robotic device . . . 20
- 1.4 Aims and Objectives . . . 20
- 1.5 Structure of the thesis . . . 21

2 Background theory 22
- 2.1 The Phenomenon of Nuclear Magnetic Resonance . . . 22
- 2.2 Principles of Magnetic Resonance Imaging . . . 24
  - 2.2.1 Fourier Transform Imaging . . . 25
  - 2.2.2 Back Projection Imaging . . . 25
- 2.3 MR pulse sequences . . . 26
  - 2.3.1 Imaging parameters . . . 27
  - 2.3.2 Spin Echo . . . 27
  - 2.3.3 Inversion recovery . . . 28
  - 2.3.4 Gradient Echo . . . 29
- 2.4 MR scanner environment . . . 30
  - 2.4.1 Siemens MR scanner hardware . . . 30
  - 2.4.2 Siemens MR scanner software . . . 31
- 2.5 Basics of RF Receiver Coils . . . 32

2.5.1 Signal-to-Noise Ratio and Quality Factor . . . 32
2.5.2 Surface coils and Phased arrays . . . 33
2.5.2.1 Tuning and Matching . . . 33
2.5.2.2 Mutual coupling . . . 33
2.5.2.3 Decoupling in transmission . . . 34

3 Literature Review **35**
3.1 MRI-guided prostate biopsy . . . 35
3.1.1 The need for MRI-guided prostate biopsy . . . 35
3.1.2 Previously proposed MRI-guided prostate biopsy systems . . . 36
3.2 Localization methods . . . 39
3.2.1 MR markers localization . . . 40
3.2.1.1 Passive markers . . . 40
3.2.1.2 Active markers . . . 41
3.2.1.3 Semiactive markers . . . 43
3.3 Receivers for intraoperative prostate imaging . . . 45
3.4 Conclusion . . . 46

4 RF markers and 1D projection analysis **48**
4.1 RF semiactive markers . . . 48
4.2 MR sequence . . . 50
4.3 RF signal analysis . . . 52
4.3.1 Signal amplitude under repeated excitations . . . 52
4.3.2 Peak detection and sub-pixel localization . . . 55
4.3.3 Peak merging . . . 57
4.3.4 Orientation to the main field . . . 58
4.4 Suitability in interventional MRI . . . 60
4.4.1 RF markers heating . . . 60
4.4.2 Image artefacts . . . 62
4.5 Discussion and conclusions . . . 63

5 Localization of N RF markers from 1D projections **65**
5.1 Problem statement . . . 66
5.2 Algorithm . . . 68
5.2.1 Choice of the directions of 1D projection . . . 68
5.2.2 Definition of the reference projections . . . 69
5.2.3 Definition of the tolerance ϵ . . . 70
5.3 Performance assessment . . . 71
5.3.1 Monte Carlo simulations . . . 71
5.3.1.1 Robustness and Accuracy . . . 71
5.3.1.2 Computational time . . . 74
5.3.2 Experimental accuracy assessment . . . 74
5.3.2.1 Static tests . . . 75
5.3.2.2 Dynamic tests . . . 77
5.4 Comparison with previously proposed methods . . . 79
5.5 Discussion and conclusions . . . 80
5.5.1 Failure scenarios . . . 80

6 Tracking in MRI-guided transrectal prostate biopsy **82**
6.1 System layout . . . 82
6.1.1 Manipulator design . . . 83

6.1.2 Endorectal biopsy probe . . . 86
6.1.3 Biopsy needle . . . 87
6.1.4 Navigation workstation . . . 88
6.1.5 Intervention Workflow . . . 88
6.2 Tracking of the endorectal probe . . . 89
6.2.1 Paired-point assignment . . . 89
6.2.2 Alignment using Least-Squares method . . . 90
6.3 Targeting accuracy . . . 92
6.3.1 Expected targeting accuracy using more than three markers . . . 93
6.4 Discussion and Conclusion . . . 95
6.4.1 Failure scenario in probe localization . . . 95

7 Guidance in MRI-guided transrectal prostate biopsy 97
7.1 Visualization of the imaging volume . . . 97
7.2 Display of Endorectal probe and biopsy needle . . . 99
7.2.1 Markers coordinates in the imaging volume . . . 99
7.2.2 Graphical Display . . . 101
7.3 Enhanced guidance . . . 102
7.3.1 Target selection and suggested trajectory . . . 102
7.3.2 Updated plane and Distances from the target . . . 103
7.4 Filtering of the measured data . . . 104
7.5 Pre-clinical trials . . . 107
7.5.1 Targeting outcome . . . 110
7.6 Discussion and conclusions . . . 114

8 RF receiver array for MRI-guided Transrectal Prostate Biopsy 116
8.1 Design of the receiver . . . 117
8.1.1 Definition of the region of interest . . . 117
8.1.2 Geometry of the detector . . . 119
8.2 Overlapping of neighbouring coil elements . . . 121
8.3 Evaluation of the receiver . . . 125
8.3.1 Magnetic field . . . 125
8.3.2 Sensitivity and Homogeneity . . . 125
8.4 Manufacturing procedure . . . 131
8.4.1 Step 1: Tuning and Matching . . . 131
8.4.2 Step 2: Detuning in transmission . . . 133
8.4.3 Step 3: Preamplifier decoupling . . . 136
8.5 Results . . . 137
8.5.1 Results on the bench . . . 138
8.5.2 Results in the MR scanner . . . 143
8.6 Discussion and conclusions . . . 150

9 Conclusions and future work 151
9.1 Summary of the Achievements . . . 151
9.1.1 Localization method . . . 151
9.1.2 Tracking method . . . 152
9.1.3 Graphical user interface . . . 152
9.1.4 Optimized receiver coil . . . 153
9.2 Discussion . . . 153
9.3 Suggestions for future research . . . 156
9.4 Outcomes of this research . . . 157

A Derivation of the RF Signal **158**

B Magnetic Field Calculation **160**

Bibliography **162**

List of Figures

2.1 Zeeman splitting for ^1H nuclei. . . . 23
2.2 Relaxation process and MR signal detection. . . . 24
2.3 Radon Transform of an image. . . . 26
2.4 Spin Echo imaging sequence. . . . 28
2.5 Inversion Recovery imaging sequence. . . . 29
2.6 Gradient Echo imaging sequence. . . . 30
2.7 The MR Siemens system. . . . 31

3.1 TRUS and MRI prostate imaging. . . . 36
3.2 InVivo Germany GmbH, Schwerin, Germany [Beyersdorff et al., 2005] and [Engelhard et al., 2006]. . . . 37
3.3 MRI-guided transrectal biopsy device proposed by Krieger et al. [2011] . . . 38
3.4 MRI-guided transrectal biopsy device proposed by Susil et al. [2006] . . . 39
3.5 Passive tracking proposed by De Oliveira et al. [2008] . . . 41
3.6 Active marker circuit. . . . 42
3.7 Needle guide presented in Krieger et al. [2005] and Susil et al. [2006]. . . . 43
3.8 Localization of multiple semiactive markers in Thormer et al. [2012]. . . . 44
3.9 Receivers for prostate imaging. . . . 46

4.1 Constructed miniature RF wireless marker. . . . 49
4.2 Tracking sequence. . . . 51
4.3 RF signal amplitude under multiple excitations. . . . 54
4.4 1D projection for three markers in the MR scanner. . . . 55
4.5 Normal distribution of the variation of a peak position. . . . 57
4.6 Identification of close peaks. . . . 58
4.7 Signal amplitude at different angles to the main field. . . . 59
4.8 Marker rotation in XY plane. . . . 60
4.9 Setup to measure the marker heating. . . . 61
4.10 Local heating of the RF markers. . . . 62
4.11 Artefact generated by a marker in the images. . . . 63

5.1 The algorithm for N=2 markers. . . . 67
5.2 6-neighbourhood of a voxel in 3D. . . . 69
5.3 Accuracy of the localization method. . . . 73
5.4 Computational time of the localization method. . . . 74
5.5 MRI-compatible two degree of freedom platform. . . . 75
5.6 Distance error. . . . 76
5.7 Dynamic tracking at different speeds. . . . 78
5.8 Comparison in computational time with Flask et al. [2001]. . . . 80

6.1 System overview. . . . 83

6.2 MRI-compatible manipulator for transrectal prostate biopsy. 84
6.3 Manipulator mechanism. 86
6.4 Endorectal biopsy probe. 87
6.5 Configuration of N= 6 markers. 94

7.1 LPH coordinate system for patient in prone position. 98
7.2 Display of the MR anatomical images on the navigation workstation. . . . 99
7.3 RF marker within the image coordinate system. 100
7.4 Graphical user interface. Display of the probe and needle. 102
7.5 Graphical user interface. Suggested trajectory. 104
7.6 Filtering of the measured data. 106
7.7 MRI-guidance set-up, navigation workstation. 107
7.8 MRI-guidance set-up, shielded monitor. 108
7.9 Manipulator and MRI prostate phantom in the MR scanner. 109
7.10 Inner section of the male pelvic phantom. 109
7.11 Targets in the prostate phantom. 110
7.12 Screenshots of the graphical user interface while performing pre-clinical trials. 113
7.13 MRI-guided targeting trials. 114
7.14 Confirmation MR image after firing. 114

8.1 Pelvic anatomy. 118
8.2 Design of the array. 120
8.3 3D view of the array. 121
8.4 Integration of the array with a device for MRI-guided transrectal prostate biopsy. 121
8.5 Segment conductor as defined in the input file to FastHenry. 122
8.6 Overlapping evaluation. 124
8.7 Envisaged setup of proposed coil and pelvic coil in the MR scanner. . . . 126
8.8 Sensitivity maps in a sagittal plane. 128
8.9 Sensitivity maps in an axial plane. 129
8.10 Variation of the magnetic field. 130
8.11 RF circuit element coil. 131
8.12 Circuit equivalent to an RF element coil. 132
8.13 Detuning network. 135
8.14 Real impedance in reception and in transmission stages. 135
8.15 Block diagram for testing of decoupling in transmission on the bench. . . 136
8.16 Example of coupling between far-away neighbours. 137
8.17 Low impedance preamplifier added in parallel to the element coil. 137
8.18 Coil manufacturing. (a) Manufacturing the butterfly element and (b) all element assembled. 139
8.19 Details of the receiver. 140
8.20 Response of each element. 141
8.21 Response in transmission and reception stages. 142
8.22 Tube phantom. 144
8.23 Setup of the proposed receiver in the MR scanner. 144
8.24 Comparison proposed coil and pelvic coil in transversal plane. Orange. . . 146
8.25 Comparison proposed coil and pelvic coil in sagittal plane. Orange. 147
8.26 Comparison proposed coil and pelvic coil in transversal plane. Tube phantom. 148
8.27 Comparison proposed coil and pelvic coil in sagittal plane. Tube phantom. 149

8.28 Signal to noise ratio. 150

B.1 Current-carrying wire arbitrarily oriented. 160

List of Tables

4.1 RF markers electrical properties. Larmor frequency $123.5MHz$. 50
4.2 RF markers electrical properties. Larmor frequency $63.87MHz$. 50
4.3 Directions of the acquired 1D projections. 52
4.4 Parameters of the sequence Turbo Spin Echo. 61

5.1 Robustness of the algorithm. Successfully reconstructed points (%). . . . 71
5.2 Positional error. 76
5.3 Distance error statistic: mean error, standard deviation and maximum error. The analysis was performed along x and z directions. 77
5.4 Distance error for increasing speed. 79
5.5 Comparison between Flask et al. [2001] and the proposed method, for $N = 3$ markers. Statistics for 10^6 simulations. 79

6.1 Targeting accuracy using up to 6 markers. Length of the needle equal to 60 mm. Standard deviation equal to 0.08 mm. 94
6.2 Targeting accuracy using up to 6 markers. Length of the needle equal to 120 mm. Standard deviation equal to 0.08 mm. 95

7.1 Parameters of the sequence Turbo Spin Echo. 111

8.1 Anatomical distances. 117
8.2 Prostate dimensions. The distances are defined as: CC dim: craniocaudal dimension, AP dim: anteroposterior dimension, TR dim: transverse dimension. 126
8.3 Estimated values of the added components. 133
8.4 Values of the electrical components and electrical properties of each element. 138
8.5 Parameters of the sequence Turbo Spin Echo. 145

Acknowledgements

I would like to express my sincerest gratitude to my supervisor, Dr. Mike Ristic, for the support, the encouragement and advice he has provided throughout these years as his student. I am profoundly grateful to Dr. Djordje Brujic, whose selfless time and care were sometimes my strongest motivation. With him I had the most insightful and encompassing discussions about the work and anything else. From him I have learnt about simplicity, balance and determination. Thank you for being such a unique mentor and, above all, a sensitive and dedicated friend.

I would like to extend my gratitude to Dr. John McGinley, whose remarkable advice and contagious commitment made the completion of Chapter 8 possible, and Prof. Richard Syms, who taught me about RF electronics and challenges in achieving a Ph.D. during my first months at Imperial. I would also like to thank all the other fellows from the research group, especially Marc and Enrico, who helped me in understanding various issues and running numerous experiments.

I would like to thank my mates from the office. In particular, Adam, whose affectionate sense of humour kept me smiling and sane in front of the most absurd situations, and Tom, whose genuine friendship lighted up many days. I would also like to thank Fidelis, from the neighboring office, for the chatty glasses of good red wine and for the inspirational dancing nights.

I would like to thank all the other friends with whom I have shared these intense years in London. Hector, for the remarkable faith and encouragement. He has been a steady influence throughout all my Ph.D. offering me a sincere hug in the toughest moments and contributing to the revision of my papers and thesis with exemplary care and generosity. Alonso, for being the male friend any woman wishes. He has the awesome and exceptional asset of being sensitive, reassuring and present with the greatest naturalness. Samira and Tatiana, in whom I have found fulfilling mutual complicity. And Andrea, Sebastian, Giuseppe and many others, who have been there in some way or another and have been part of this memorable fervent time.

A huge thank you to my friends back home; in particular, Valentina, Eleonora, Adriano and Marco. They gave me that sense of stability and foundation that sometimes I desperately need being away from my home country.

Finally, I would like to deeply thank my family. My parents, from whom I have learnt that love can actually be infinite and respectful. My darling brother Matteo and sister Chiara, for the unbreakable crystalline bond.

Now, if somebody would ever come and ask an advice about doing a Ph.D., I would perhaps answer: *Start by doing what's necessary; then do what's possible; and suddenly you are doing the impossible.* This is a quote stolen from Dr. Djordje Brujic dissertation and these words were pronounced a very long time ago by San Francesco d'Assisi.

Dedicated to my grandmothers, from whom I have learnt about will, courage and genuineness.

Chapter 1

Introduction

Magnetic Resonance Imaging (MRI) is an imaging technique extensively used for diagnostic purposes as it offers comprehensive assessment of anatomical structures and functions with no ionising radiation exposure [Pompili et al., 2013][Jarnum et al., 2009][Henzler et al., 2010]. In view of these benefits, in the last twenty years, there has been an increasing effort in transferring interventional procedures to the MRI environment. The excellent soft-tissue contrast of MR imaging not only yields more reliable localization of target lesions but also enables image-based navigation of medical instruments within the patient's body [Moore, 2005][Mortele et al., 2003][Reither et al., 2000].

In parallel, the introduction of robotic devices to assist clinicians has enabled the accessibility to the patient inside the MR scanner and minimized operational hazards [Lee et al., 2010]. The integration of robotic assistant devices with image-based guidance has the potential to improve accuracy and efficiency of interventions, and to reduce patient's trauma [Busse et al., 2007][Lee et al., 2010]. There are many potential applications of robot-assisted interventional MRI in the field of surgery including percutaneous neurosurgery, needle-based interventions, orthopedic surgery and intracavity interventions, such as transrectal prostate biopsy [Kuo and Dai, 2009].

1.1 The context of the research

The research presented in this thesis is part of the project *MRI Guided Endoscope*. The project was funded by The Wellcome Trust and aimed to develop two MRI-guided systems suitable for the following interventional procedures: prostate biopsy for the diagnosis of suspected cancer and hepatobiliary procedures involving MR-guided cholangiopancreatography. The project involved a close collaboration between the Mechanical Engineering and Electrical and Electronic Engineering departments at Imperial College

London, while the clinical input was provided by The Institute of Cancer Research, Royal Marsden Hospital (Prof. Nandita Desouza) in regard to the prostate biopsy intervention, and by St Mary's Hospital (Prof. Simon Taylor-Robinson) in regard to the hepatobiliary procedures.

The focus of the work presented in this thesis has been the development of the MRI-guided prostate biopsy system. The goal was to achieve higher accuracy, reduced interventional time, superior success rate and reduced training requirements than those using previously proposed systems. With these aims, two main objectives were identified. The first objective was the design and manufacture of an MRI-compatible remotely operated device. The device included an endorectal probe for safe and accurate positioning of the biopsy needle and an elongated biopsy gun for collection of the target sample within a closed-bore MR scanner. This work was done by fellow Ph.D. student Nicholas Lambert and its key aspects are outlined in Chapter 6 in order to improve understanding and completeness of the thesis. The second objective was the development of a navigation system to enable accurate, fast and reliable guidance of the biopsy needle to the target. This work and its integration with the MRI system is the scope of the research presented in this thesis. In particular, the navigation system included both software and hardware components. The software components were localization and tracking algorithms and graphical user interface; the hardware components were fiducial markers for instrument tracking and a receiver coil array for intra-operative imaging of the target lesions. Furthermore, the work presented here on instrument tracking and visualization is relevant in the general context of tracking and guidance in interventional MRI.

1.2 Research motivation

Prostate cancer is the second most common cause of cancer death in men worldwide, after lung cancer [Jemal et al., 2011]. The organization Prostate Cancer UK reports a mortality rate of around 35 prostate cancer deaths for every 100,000 men [Lane et al., 2010]. The American Cancer Society estimates that about 240,000 new cases of prostate cancer will be diagnosed in the United States in 2013 and about 30,000 men will die of prostate cancer [Wolf et al., 2010]. Mortality rate might be reduced with earlier diagnosis of this disease, improved monitoring of cancer staging and identification of an optimal treatment.

MRI is currently the golden standard for detection of prostate cancer, owing to its excellent soft tissue contrast and functional imaging capabilities. However, MRI's low specificity has limited its role in prostate cancer diagnosis and tissue biopsy is still an indispensable tool. Nevertheless, current biopsy strategies present limitations which result in inadequate prostate cancer staging and treatment [Susil et al., 2003].

Transrectal ultrasound biopsy (TRUS) is the technique routinely used to perform prostate biopsy [Presti, 2000]. Since the target lesions cannot be distinguished in the ultrasound images the needle is fired into regions of the gland where the targets are expected to be on the basis of the previously acquired diagnostic MR images. This results in a relatively low probability of sampling the suspect tissue and the need to collect multiple samples, with consequent distress for the patient and risk of spreading cancer cells [Terris, 1999].

A system which could enable prostate biopsy within a high-field MR scanner would provide for reliable identification of the suspect lesions. As a result, detection and staging of prostate cancer could be more accurate and the overall procedure less distressful for the patient [Susil et al., 2003].

Several approaches to MRI-guided prostate biopsy within a closed-bore scanner have been investigated [Beyersdorff et al., 2005][Susil et al., 2006][Krieger et al., 2007]; however, there is still no consensus regarding an optimal interventional system. The reason lies in the complexity of such a system, whose performance depends equally and critically on several components, namely the biopsy probe tracking performance and the visualization capabilities combined with control of the instrument positioning mechanism. In order to achieve accurate targeting, optimization of these components is essential and this need provides the motive of this thesis.

1.3 Research outline

The key challenges in achieving efficient and accurate navigation of the biopsy probe are fast and robust instrument tracking, accurate registration and reliable and effective intra-operative visualization of both instrument and target. The significance of these issues is outlined here and the solutions presented in this thesis are introduced. Key aspects in developing the robotic device are also presented.

1.3.1 Instrument tracking and registration

MRI-guided interventions within closed-bore MR scanners do not allow direct view of the medical instrument. As a result, the interventions rely on visual feedback, which entails a computer-generated model representative of the instrument and displayed within the imaging volume [Moche et al., 2008] [Fichtinger et al., 2008]. Pre-requisite for an effective eye-hand coordination is accurate, robust and fast tracking of the medical instrument within the MR scanner.

As the medical instrument itself is not directly visible on the MR images, fiducial

markers that are both MR visible and which do not affect the image quality are embedded within the instrument [Garnov et al., 2011]. Fiducial markers usually represent points in space, the position of which can be determined by combining MR imaging and signal processing. In order to establish the 3D position of the instrument (rigid body) in the imaging space, a minimum of three markers is needed; however, more markers may be employed in order to improve the accuracy of the localization [Rachinger et al., 2006].

Several solutions involving different markers and localization methods may be found in the literature and they are discussed in Chapter 3. The most relevant work found was presented by Flask et al. [2001] and this aimed to localize semiactive fiducial markers using 1D projections. The use of 1D projections led to a significantly higher localization rate than solutions involving image processing. In the work presented in this thesis, a new method for 3D localization of semiactive markers (or active markers when a single receiver channel is used) using 1D projections was developed, offering significant improvements in speed, robustness and accuracy over the previous ones. The benefits are the significantly improved accuracy and update rate in instrument tracking and a more reliable visual feedback.

A requirement for intra-operative visualization is to display correctly, in real-time, the instrument position in relation to the patient's anatomy. If the procedure involves withdrawal of the patient from the MR scanner then the computed fiducial markers and the patient need to be registered by some method [Beyersdorff et al., 2005] [Engelhard et al., 2006] [Krieger et al., 2011]. The aim of this research was to provide the means for performing the entire procedure in one set-up, without moving the patient out of the scanner, with consequent shorter procedure time, simpler workflow and more accurate outcome. This also meant that both the anatomical images and the instrument position were directly provided in the same coordinate system and registration was greatly simplified.

1.3.2 Visualization and instrument guidance

The manipulator is remotely controlled by the clinician on the basis of image feedback provided on a monitor positioned in the scanner room. Previously proposed MRI-guided systems generally use a 2D visualization, which makes 3D guidance of the instrument difficult due to the lack of information [Krieger et al., 2011] [Susil et al., 2006]. Also, it is very challenging to devise a truly generic 3D visualization technique and the solution almost inevitably needs to be tailored for the specific application. This thesis presents a new form of graphical user interface which provides 3D image feedback for the specific positioning mechanism and procedure described here.

In view of possible tissue movements during the intervention, intra-operative update

of the anatomical images should also be provided to enable accurate targeting [Fichtinger et al., 2008]. However, the acquisition of MR images may considerably slow down the procedure, especially if multiple slices are required. If a single slice is acquired then its selection needs to be adequately controlled. Also, it is highly beneficial if the visualization technique requires little or no interaction from the clinician, leaving him/her free to operate. The solution sought in this work involved a combination of pre-operative and intra-operative imaging. Pre-operative images provided a road-map for guiding the instrument to the identified lesion and the intra-operative images, acquired before firing the biopsy needle, provided a verification of the actual location of the target. If the suspect lesion had moved, the needle was re-aligned accordingly.

In addition, intra-operative guidance may be enhanced through the implementation of additional navigation aids specific to the intervention [Zhang et al., 2000] [Patil et al., 2009]. In this work several visualization functionalities were developed in close consultation with clinical staff. These included automatic update of the preferred targeting trajectory, of the distance from the tip of the biopsy needle to the target and of the visualized plane containing the needle.

1.3.3 Optimized receiver coil

It is challenging to obtain a sufficient intra-operative image quality such that the suspect lesions can be accurately differentiated [Fichtinger et al., 2008]. The main issue is to achieve high signal-to-noise ratio over the entire prostate region. Particularly, clinicians pose the requirement of high sensitivity over the peripheral zone of the prostate, where there is highest probability of cancer [Center, 2013].

Diagnostic imaging of the prostate conventionally involves the use of an endorectal balloon coil in combination with a standard pelvic coil array [Bloch et al., 2004]. However, this solution is unsuitable for the biopsy procedure due to the need to accommodate the endorectal biopsy probe. It is also difficult to incorporate an adequate receiver coil within the biopsy probe itself; the receiver coil may limit the range of movements of the probe and its sensitivity may not be adequate due to acceptable coil size [DeSouza and Gilderdale, 1996]. If the standard pelvic coil array alone is used, then the image quality may not be adequate, especially if its position has to be compromised in order to allow interventional access to the patient [Elhawary et al., 2010].

In this work a solution was sought in the design of a new type of external coil array. Its geometry was optimized for improved image quality over the entire prostate region while allowing adequate access to the patient during the procedure. This receiver would also serve as an attractive alternative to the endorectal coil for diagnostic imaging.

1.3.4 Robotic device

In order to overcome the spatial limitation within a closed-bore MR scanner and to remotely control the medical instrument, a robotic device is needed [Lee et al., 2010] [Fichtinger et al., 2008]. A major potential challenge in designing the robotic device is the MR compatibility of sensors and actuators. The device developed in this project was purely mechanical, remotely operated using flexible cables and on the basis of image feedback.

In general, the design of a robotic device needs to be tailored for the specific intervention [Fichtinger et al., 2008]. In many procedures the instrument is moved about a single point and thus a *remote-centre-of-motion* mechanism design is often employed [Lee et al., 2010]. According to this approach, the instrument rotates about a point which decouples rotational and translational movements. The remote-centre kinematics of the manipulator developed in this project provides three degrees of freedom that follow the natural motion of the endorectal probe during the procedure [Lambert et al., 2012]. In order to minimize tissue movements and maximize patient safety, the manipulator was designed to be positioned such that the centre of motion coincides with the entry point into the patient's body. This also meant that the controls were intuitive for the clinician.

1.4 Aims and Objectives

The research presented in this thesis aims to develop an optimized navigation system suitable for performing MRI-guided transrectal prostate biopsy. As outlined above, this includes fast, accurate and robust tracking of the instrument, real-time visual feedback of the location of the instrument in relation to the target and improved intra-operative image quality. The specific objectives were as follows:

- Development and validation of a method for 3D localization of three or more fiducial markers. The aim was to achieve sub-millimeter accuracy and faster update rate than previously proposed methods.
- Development of a fast and accurate method for tracking the endorectal biopsy probe. As target lesions can have dimension as small as 5 mm and the image resolution is about one millimetre, the objective was a targeting error of one millimetre.
- Development of a visualization software which enables effective guidance of the instrument. The aim was to provide reliable and automatic 3D visual feedback of the position of the endorectal probe in relation to the identified target.

- Development of an external receiver coil which leads to improved intra-operative imaging and is suited for the biopsy procedure. The purpose was to achieve superior signal to noise ratio compared to the standard pelvic array coil, especially over the peripheral region of the prostate.

1.5 Structure of the thesis

Chapter 2 presents background theory and information on MR imaging, including the hardware and software components of MR scanners.

Chapter 3 reviews the current literature, covering previous work in instrument tracking and target imaging, with focus on MRI-guided prostate biopsy.

Chapter 4 describes the construction of miniature RF semiactive fiducial markers and the development of the MR tracking sequence for acquisition of 1D projections. An analysis of the signal peaks involving experiments in the MR scanner is presented and the suitability of the markers for the specific application is investigated.

Chapter 5 presents the algorithm for localization of N markers in 3D using 1D projections. Validation of the algorithm is reported, including Monte Carlo simulations and experiments in the MR scanner.

Chapter 6 presents the method for tracking the endorectal prostate biopsy probe. This is based on the proposed localization method and comprises paired-point assignment and Least-Squares method. Tracking of the probe is preceded by a description of the prostate biopsy system and probe design. An analysis of the targeting accuracy when three or more markers are used is presented.

Chapter 7 describes the visualization software which was developed to provide image-based guidance of the endorectal probe and needle within the patient's body to the clinician. Pre-clinical trials performed by clinical staff at Royal Marsden Hospital are reported.

Chapter 8 describes the novel external receiver array prototype for intra-operative imaging of the prostatic area. The design of the receiver is illustrated and an analysis of sensitivity and homogeneity is presented. This involves simulations and imaging in the MR scanner.

Chapter 9 concludes the thesis with a review of the work done, a look at future developments and a list of the outcomes of the research.

Chapter 2

Background theory

In this Chapter the background theory relevant to the thesis is provided. Initially, the principles of magnetic resonance and the fundamental imaging modalities are described. Then, the MR sequences employed in this work are illustrated. Since the research was conducted on Siemens MR scanners, basics of hardware and software in a Siemens MR environment are then reported. Finally, key concepts in RF electronics are described.

2.1 The Phenomenon of Nuclear Magnetic Resonance

MRI is based on the principles of Nuclear Magnetic Resonance (NMR), a phenomenon that was discovered by Bloch and Purcell in 1950 and which occurs when nuclear spins are placed in a static magnetic field and exposed to a second oscillating magnetic field [Hornack, 1996]. If nuclear spins are immersed in a static magnetic field B_0, an interaction between B_0 and the magnetic moments of the spins occurs. This interaction is called *Zeeman Interaction* and causes a splitting of the spins energy levels into the *Zeeman levels*. The energy associated with each level is $E_m = -\gamma\hbar m B_0$, where γ is the gyromagnetic ratio, $\hbar$ is the reduced Planck's Constant ($\hbar = \frac{h}{2\pi}$) and m is the magnetic quantum number. Also, each level satisfies the relation $-I \leq m \leq I$, where I is the spin quantum number.

Clinical MRI is normally based upon ^1H nuclei, since ^1H is the most abundant nucleus in the human body and it has a relatively strong magnetic moment, which result in a large MR signal. For ^1H nuclei, $I = \frac{1}{2}$ and $m = \pm\frac{1}{2}$. The two energy levels correspond to two possible spins orientations; one orientation is parallel to B_0 (lowest energy) and the other orientation is antiparallel to B_0 (highest energy), as shown in Figure 2.1. The energy difference between the two levels is equal to:

$$\triangle E_m = \hbar\gamma B_0 \tag{2.1}$$

Therefore, a photon of energy $E = h\nu_0 = \Delta E_m$ can stimulate a transition between the two energy levels, which corresponds to the *resonance condition*:

$$\omega_0 = \gamma B_0 \tag{2.2}$$

with $\omega_0 = 2\pi\nu_0$.

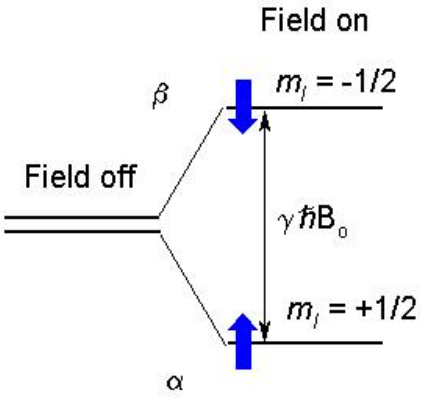


FIGURE 2.1: Zeeman splitting for ^1H nuclei.

The population of spins in each level is given by the *Boltzmann Distribution* function [Hornack, 1996]:

$$\frac{N^+}{N^-} = e^{-\frac{\Delta E_m}{kT}} \tag{2.3}$$

where k is the Boltzmann constant and T is the temperature. Equation 2.3 states that the number of spins parallel to B_0, N^+, is higher than the number of spins antiparallel to B_0, N^-. It follows that the vector sum of spins is non-zero and points in the direction of B_0. This vector was introduced to describe a system of spins from a macroscopic point of view and is known as *net magnetization vector* or, simply, *magnetization* M.

The MR signal is generated from a system of spins by applying a *pulsed magnetic field* B_1 having the same frequency as the resonance frequency ν_0. While B_1 is applied, M rotates by an angle α, which is called *flip angle*, proportionally to the duration of B_1. When B_1 is switched off, M returns to its equilibrium position by precession around the static field B_0. This process is called *relaxation*.

Relaxation consists of an exponential decay of the transverse component of M, M_{xy}, through a gradual dephasing of the spins described by the time constant T_2, along with an exponential growth of the longitudinal component of M, M_z, to the initial value described by the time constant T_1. The values of the time constants T_1 and T_2 depend on the specific molecular environment of the spins. The presence of inhomogeneities in

the static field causes an additional dephasing effect which makes the effective dephasing time constant equal to T_2^*, which is always less than T_2.

If during relaxation a receiver coil is placed perpendicularly to the transverse plane, the transverse component M_{xy} induces a voltage in the coil due to its precessional motion, as shown in Figure 2.2. This induced voltage is known as *Free Induction Decay* (FID) and is the MR signal.

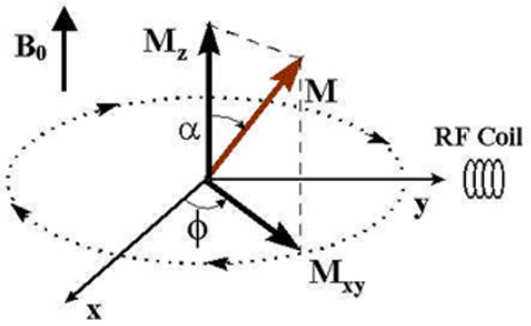


FIGURE 2.2: Relaxation process and MR signal detection.

2.2 Principles of Magnetic Resonance Imaging

The extension of the NMR concept to imaging follows from the spatial encoding of the MR signal described above using magnetic field gradients. Spatial encoding of the MR signal is the key concept in MRI. The magnetic field B_0 is made linearly dependent on the spatial position of the spins by applying a one-dimensional constant magnetic field gradient G [McRobbie, 2003]. For instance, if a field gradient is applied along the x axis, G_x, then the magnetic field at the location x, $B_0^{'}$, becomes

$$B_0^{'} = B_0 + G_x x \tag{2.4}$$

and, therefore, the resonance Equation 2.2 becomes

$$\omega_0^{'} = \gamma(B_0 + G_x x). \tag{2.5}$$

Equation 2.5 states that the resonance angular frequency of a spin depends on its position along the gradient field direction.

In MRI, the first step is the localization of the Radio Frequency (RF) excitation to a region of space, which is accomplished by application of an RF pulse in conjunction with a gradient, known as *slice selection gradient* [Brown, 2005]. The direction of the slice selection gradient determines the slice orientation, whereas the gradient amplitude together with the RF pulse bandwidth determines the slice thickness. Once the slice has

been selected, two different main imaging modalities can be used: Fourier Transform Imaging or Back Projection Imaging.

2.2.1 Fourier Transform Imaging

In a conventional Fourier Transform Imaging sequence, the selection of a slice is followed by the application of other two different gradients, called *phase encoding gradient* and *frequency encoding gradient*. A *phase encoding gradient* is applied along one direction of the slice before data are collected. When the gradient is switched on, the resonance frequencies of the spins are altered according to the spin locations along the gradient direction. As the gradient is switched off, the frequencies return to the same value but the phases are different. The amount of induced phase shift depends on the magnitude and duration of the phase encoding gradient that the spin experiences and on the spin location. An MR acquisition consists of multiple repeated applications of the phase encoding gradient until all the spatial frequencies are interrogated. At each repetition the magnitude of the phase encoding gradient is changed in equal steps between the maximum and the minimum value of the gradient.

A *frequency encoding gradient* is applied along the other direction of the slice during signal acquisition. The frequency encoding gradient causes the spins to precess at a frequency which depends on their location along the direction of the gradient. The acquired signal therefore contains a mixture of different frequencies. A Fourier Transform determines the frequency components of the signal in the frequency encoding gradient direction, at each phase gradient step. In order to spatially locate the spins along both the directions of the slice, a Fourier Transform is also applied along the phase encoding direction.

As the Fourier Transform converts the acquired data into signal amplitude versus its frequency, it is possible to associate a gray level to each data and to identify its location in the image matrix. The Fourier Transform is applied once all the data are acquired and collected into a matrix, known as *k-space*. All the information necessary to reconstruct an image is contained within the k-space. Although each data point contributes to all aspects (frequency, phase and amplitude) of every location within the slice, some data points emphasize different features in the final image. Contrast in the image is primarily determined by data in the center, whereas edge definition is primarily determined by data at the edges of the k-space [McRobbie, 2003] [Hornack, 1996].

2.2.2 Back Projection Imaging

Most of current imaging techniques are based on the Fourier Transform and they fill the Cartesian grid of points in the k-space using a sequence of gradients. In Back

Projection Imaging, a radial filling of k-space is performed by applying a one dimensional field gradient at different angles.

At each gradient orientation, the MR frequency spectrum is recorded. The variation of the angle is accomplished by the application of a linear combination of two gradients. Once all the data are acquired, the projections are radially back projected by applying the inverse Radon Transform [Deans and Roderick, 1983]. The Radon Transform is the integral of a function over a straight line. Each 1D projection is the line integral $g(s, \varphi)$ of the image along a line at distance s from the origin of the coordinates system and at angle φ off the x axis, as shown in Figure 2.3. The collection of the line integrals $g(s, \varphi)$ at all the angles φ is called the Radon Transform of the image [Hornack, 1996].

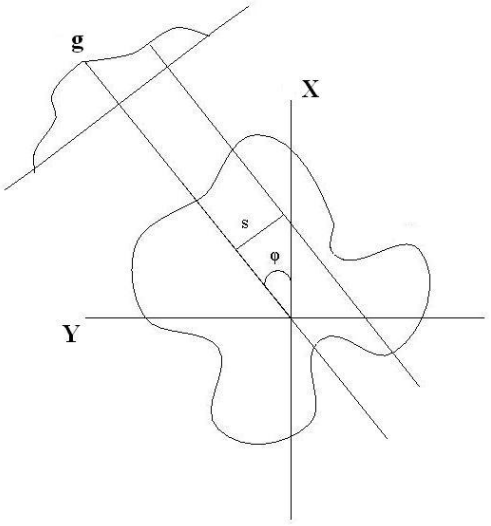


FIGURE 2.3: Radon Transform of an image. A 1D projection is the line integral $g(s, \varphi)$ of the image along a line at distance s from the origin and at angle φ off the x axis.

1D projections are used in this thesis in order to localize RF fiducial markers; however, since the intent was to determine the location of the fiducial markers without the need to produce an image, the method does not involve the inverse Radon Transform. The projections of the fiducial markers will be simply back projected in space and their intersections will be computed in order to eventually determine the original markers' coordinates.

2.3 MR pulse sequences

A pulse sequence is the specific order of excitation pulses and magnetic field gradients which control the MR signal and hence the acquired image. MR sequences are generally divided into two categories on the basis of the type of echo, namely Spin Echo and Gradient Echo.

2.3.1 Imaging parameters

In addition to the flip angle, the main parameters used to control the evolution of the magnetization and hence the final image contrast are the Echo Time (TE) and the Repetition Time (TR). TE is the time from the centre of the RF excitation pulse to the centre of the received echo signal; TR is the time between repeated acquisitions, which is also equal to the time between successive excitation pulses.

Another important parameter is the receiver bandwidth, RBw, which determines the amount of noise collected during the acquisition of the signal. Some disadvantages of excessively lowering the RBw are that it lengthens the time required to obtain data, which can lead to lower signal levels, increased scan times and an increase in the appearance of chemical shift artifacts.

2.3.2 Spin Echo

In a Spin Echo (SE) sequence a 90° pulse is applied, followed by a 180° pulse at time $\frac{TE}{2}$ to refocus the dephasing transverse magnetization. The refocusing pulse causes the signal to form an echo at time TE (Figure 2.4). This echo is detected by the receiver coil during the application of a frequency encoding gradient and forms a single line of spatially encoded data. The inversion of transverse magnetization by the 180° pulse causes cancellation of the increased relaxation due to field inhomogenieties, hence the amplitude of the echo will depend on constant T_2, and not on $T_2^\star$. A Turbo Spin Echo (TSE) sequence applies a train of 180° refocusing pulses for as long as the remaining transverse magnetization is sufficient to form an echo, acquiring multiple lines of spatially encoded data. This speeds up the scan time by a factor called the turbo-factor, which is the number of repeated refocusing pulses, or the number of echoes formed per excitation. By setting a long TR and a long TE, T_2-weighted images can be obtained, in which tissues with long T_2 give the highest signal intensities. T_2-weighted images are often used for pathology scans since abnormal fluid will be bright against dark tissue. In this thesis, T_2-weighted Turbo Spin Echo will be employed for prostate imaging.

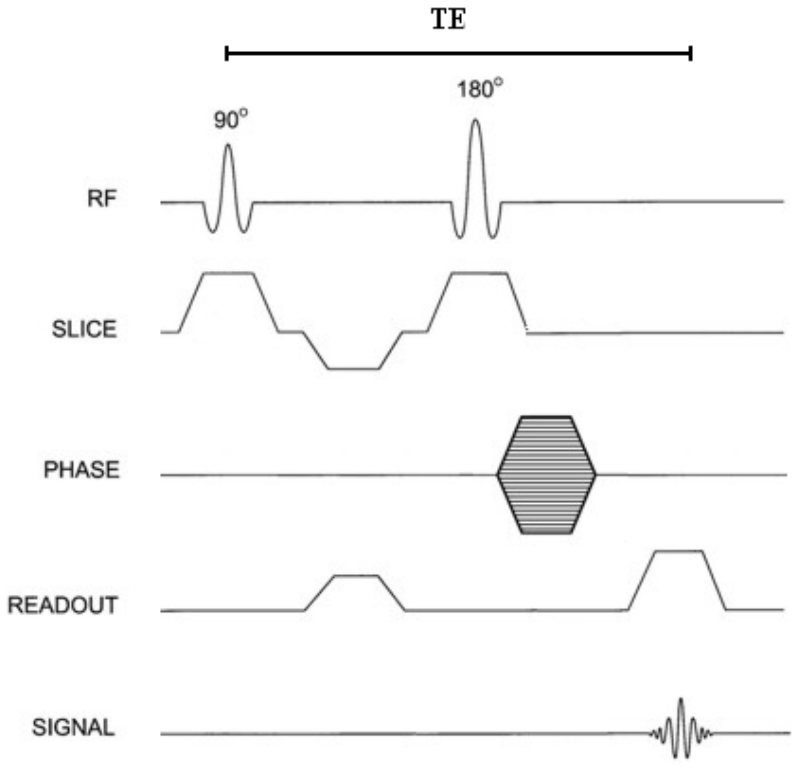


FIGURE 2.4: Sequence diagram of a basic Spin Echo (SE) imaging sequence [McRobbie, 2003].

2.3.3 Inversion recovery

Inversion Recovery (IR) is a SE sequence with an additional RF 180° pulse applied before the 90° pulse, as shown in Figure 2.5. This inversion pulse flips the magnetization by 180°, such that the magnetization must now travel through zero back to M_0. Because different tissues have different T_1 values, the Inversion Time (TI) can be selected so that the signal from some tissue is prepared with zero initial magnetization, a state which is called saturation. This removes the tissue from the final image. By varying TI, an IR sequence can be employed to measure the relaxation time T_1.

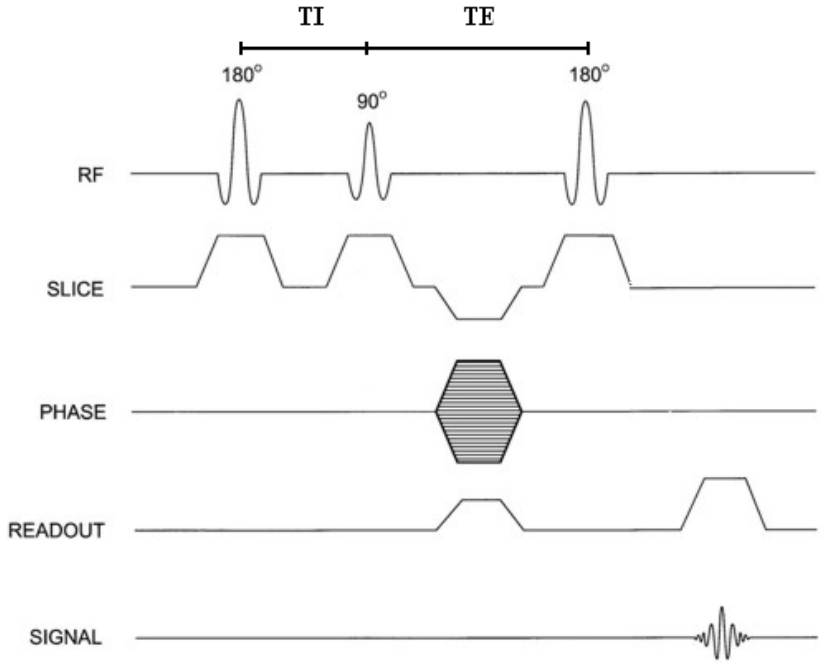


FIGURE 2.5: Sequence diagram of an Inversion Recovery (IR) imaging sequence [McRobbie, 2003].

2.3.4 Gradient Echo

A Gradient Echo (GE) sequence uses gradients to dephase the transverse magnetization faster than would happen naturally and to rephase the signal in a shorter time than a SE sequence. This, combined with a low excitation pulse, results in a significantly reduced scan time.

A standard GE sequence is shown in Figure 2.6. In a GE sequence, TR may be less than T_2 and, therefore, transverse magnetization may remain between consecutive excitations; this may cause additional echoes which would affect the image quality. In order to avoid this effect, the remaining transverse magnetization is normally destroyed by the application of spoiling gradients. Alternatively, the remaining magnetization is *rewound* by reversing the gradients, in which case the remaining signal adds to the signal acquired in the next measurement (*balanced* sequences).

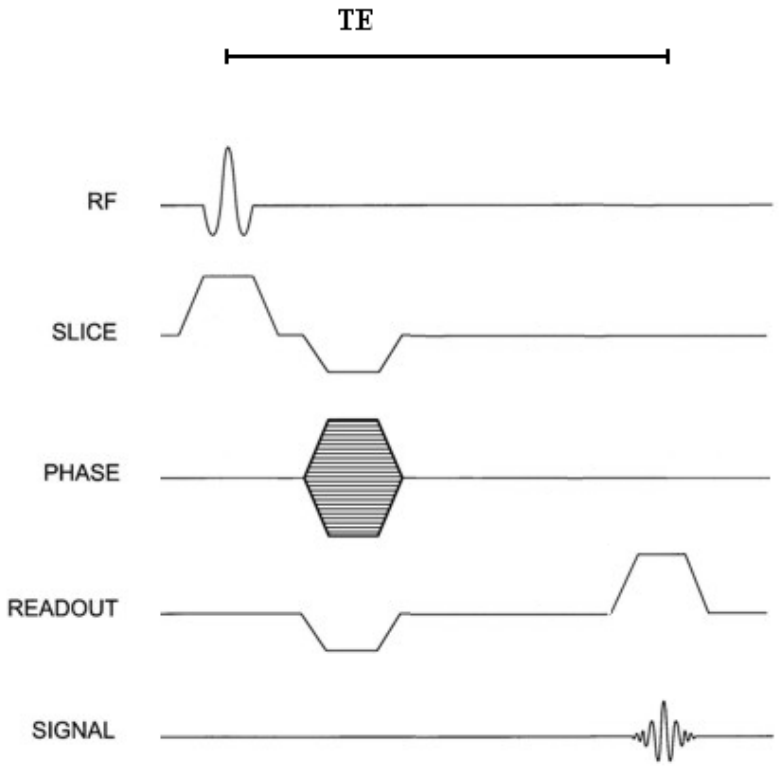


FIGURE 2.6: Sequence diagram of a basic Gradient Echo (GE) imaging sequence [McRobbie, 2003].

2.4 MR scanner environment

The development of the MRI-guided prostate biopsy system was primarily based on the Siemens MR system. This choice was motivated by the collaboration with The Institute of Cancer Research (Sutton, London, UK), where prostate biopsies are performed in Siemens MR Scanners.

2.4.1 Siemens MR scanner hardware

The Siemens MR system comprises three computers connected via 1 Gbit/s Ethernet network, as shown in Figure 2.7:

- *Host.* This computer is used to drive the MR scanner and to visualize and store the acquired MR images.
- *MPCU (Measurement and Physiological Control Unit).* This computer controls the gradient coils, the RF coils and any additional devices. MR sequences not included in the system can be programmed by the user and run on the MPCU.

- *Image processor*. This computer is responsible for initial storage of the acquired raw data and processing of the data to produce images.

Further information on MRI scanner hardware is given in [McRobbie et al., 2003].

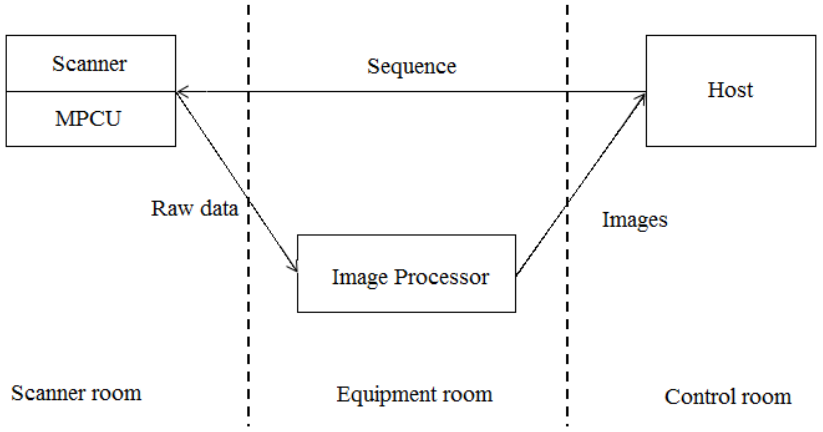


FIGURE 2.7: The MR Siemens system is composed by three Ethernet networked computers: Host, MPCU and Image processor.

2.4.2 Siemens MR scanner software

The Siemens MR System is based upon the Syngo interface and the Integrated Development Environment for Applications (IDEA) platform. The IDEA platform includes two main packages: (i) the Sequence Development Environment (SDE) package for programming pulse sequences and (ii) the Image Calculation Environment (ICE) for processing of the data acquired by the scanner. The IDEA software also includes a compiler and a simulation package which allow researchers to develop new sequences and image reconstruction methods on a separate Windows PC. Programming is done using C++ language.

The Sequence Development Environment (SDE) package enables to program and customize the imaging sequences. Strength of the gradients, RF pulses, and data acquisition can be set by the user. Templates of standard sequences are available and can be customized to obtain a specific result. The Image Calculation Environment (ICE) package provides the framework to implement the image calculation steps. Each sequence in the scanner has a reference to an ICE program file which determines the steps to be applied to the raw data. Each step is described by a *functor*. Functors are grouped together by *configurators* that combine multiple functors into the image processing pipeline. The steps taken in the pipeline can be programmed by the user. These features and more are further explained in the IDEA documentation [Wertherner, 2006][Zwanger, 2006].

2.5 Basics of RF Receiver Coils

The quality of the MR images depends on the quality of the detected MR signal, which can be optimized by placing the receiver Radio Frequency (RF) coil in proximity of the source. In electronics, *resonance* occurs when an inductance L and a capacitance C are combined in an LC circuit. When a signal with a certain frequency is applied, a large quantity of stored energy will continually transfer between the capacitive reactance and inductive reactance, resulting in signal amplitudes much higher than that of the original applied signal. The circuit is said to resonate at the particular frequency at which the resultant amplitude is greatest [Terman, 1943].

A resonant circuit can be classified as a parallel or a series resonant circuit. A parallel resonant circuit appears as an open circuit to an incident signal at the resonant frequency, while higher or lower frequencies will find it easy to pass through one of the two branches. Alternatively, a series resonant circuit appears as a short circuit to an incident signal at the resonant frequency, while higher or lower frequencies will be blocked by one of the two components [Terman, 1943].

2.5.1 Signal-to-Noise Ratio and Quality Factor

A critical issue in the reception of the MR signal is the SNR, which determines the quality of the MR image. The higher the SNR, the higher the quality of the image. In order to maximize the SNR, it is necessary to maximize the received signal and minimize the background noise.

The SNR may be expressed as [Fujita et al., 2013]:

$$\frac{S}{N}\alpha\frac{B_{xy}(\vec{r})}{\sqrt{R_c+R_s}} \tag{2.6}$$

where $B_{xy}(\vec{r})$ is the transverse magnetic field induced by the coil at the point $\vec{r}$, R_c is the coil resistance and R_s is the sample resistance. In order to optimize the SNR, $B_{xy}(\vec{r})$ may be maximized by placing the coil closer to the source of signal and perpendicularly to B_0 while R_c and R_s may be minimized, respectively, by increasing the coil Q-factor and by choosing the coil size to match the region of interest.

In particular, the noise due to the coil can be modelled as *Johnson noise* [Terman, 1943]:

$$V_n=\sqrt{\frac{4R_cK_BT}{\Delta\omega_0}} \tag{2.7}$$

where T is the environmental absolute temperature, K_B is the Boltzmann constant, ω_0 is the resonance angular frequency of the coil and $\Delta\omega_0$ is the bandwidth of the coil. The noise associated with the sample is due to the random thermal and induced molecular

motion within it; since this noise is very hard to control, it is desirable that the noise due to the coil is as low as possible.

The bandwidth $\Delta\omega_0$, which appears in Equation 2.7, is related to the *quality factor* Q of the coil:

$$Q = \frac{\omega_0}{\Delta w_0} \tag{2.8}$$

The *quality factor* Q of a resonant circuit is a measure of the selectivity of the resonant circuit [Terman, 1943]. A higher value of Q corresponds to a more narrow bandwidth, which is desirable. A coil with high Q has a small bandwidth, therefore produces less noise and gives higher SNR than a coil with lower Q.

2.5.2 Surface coils and Phased arrays

Surface coils are simple loop coils, which can be either flat or flexible. The simplest type of surface coil is a single loop coil; multiple surface coils may be combined to create a phased array coil. A phased array coil generally consists of a number of mutually decoupled surface coils that detect MR signals simultaneously; by combining these signals, an image can be obtained with more uniform sensitivity and higher SNR than an individual coil having the same diameter [Roemer, 1990].

2.5.2.1 Tuning and Matching

The MR signal is detected by receiver coils tuned at the same frequency of ^1H protons to ensure greater MR signal amplitudes from the anatomy [Hoult, 1978]. For instance, at 1.5 T, the receiver coil must be *tuned* at $\nu_0 = 63.87MHz$.

Once detected, the signal is transmitted to the MR scanner receiver port by means of a 50 Ω transmission line. According to the *Maximum Power Transfer theorem*, in order to maximize the power transfer from the receiver RF coil to the transmission line, the impedance of the receiver RF coil (source) must be *matched* to that of the 50 Ω transmission line (load) [Terman, 1943].

2.5.2.2 Mutual coupling

The most important recognized requirement in designing phased array coils is to minimize the mutual coupling that exists between neighbouring surface coils [Roemer, 1990]. Mutual coupling causes transfer of signal from an element to another, which results in splitting of the resonance frequencies and disrupts the phased array receive pattern.

Three techniques are normally employed in order to minimize mutual coupling. These

are *inductive decoupling*, *capacitive decoupling* and *preamplifier decoupling* [Fujita et al., 2013]. *Inductive decoupling* consists in partial overlapping of neighboring elements so that the total magnetic flux between them is cancelled. This method is the most often used because it is geometrically fixed and does not require tuning. *Capacitive decoupling* is used when topology and position of the element cannot be changed. It consists in the introduction of a decoupling capacitor in series with the mutual inductance of the two elements. *Preamplifier decoupling* is the most modern decoupling method and consists in presenting a low impedance preamplifier to the coil and inserting it into a parallel resonance trap which is in series with the coil. The parallel resonant trap blocks the current from flowing in the coil due to the high impedance, even though the coil is receiving and faithfully transmitting MR signal to the preamplifier. This method allows decoupling of the elements placed far from each other, which cannot be decoupled by other means [Taracila et al., 2008].

2.5.2.3 Decoupling in transmission

Coupling of the receiver RF coils with the transmitter RF coil during RF excitation may cause significant induced currents in the receivers and hence significant disturbances in the local field, damage to the electronic components and excess of the Specific Absorption Rate (SAR) [Rea et al., 2009]. This may be prevented by detuning the receiver during the transmission phase by employing *passive detuning* or *active detuning*. Both approaches make use of PIN diodes which, when forward biased, cause a parallel LC network to resonate. This leads to high impedance across the parallel circuit and therefore prevents significant current from flowing in the receiver. In *active detuning* the signal required to forward bias a PIN diode is supplied, whereas *passive detuning* relies on the property of the transmit field to forward bias a pair of crossed PIN diodes. The pair of PIN diodes limits the maximum voltage that can develop across the capacitor C to 0.5 V while it permits reception of the MR signal, since the voltage during reception does not exceed this threshold.

Chapter 3

Literature Review

The field of interventional MRI has significantly expanded in the last twenty years thanks to the advances in MRI technology, computing power and MR-compatible robotics [Cleary and Peters, 2010]. There are many potential applications of interventional MRI and research is ongoing towards faster and more accurate approaches [Moche et al., 2008]. As prostate biopsy is the focus of this thesis, this Chapter begins with a review of previously proposed systems for MRI-guided prostate biopsy, including tracking, robotic and visualization solutions. The Chapter goes then more deeply into the broad existing literature in instrument tracking. Finally, receiver coils currently available for diagnostic and intra-operative imaging of the prostatic area are discussed.

3.1 MRI-guided prostate biopsy

3.1.1 The need for MRI-guided prostate biopsy

Prostate cancer normally increases the production of prostate-specific antigens (PSA) and, therefore, screening for increased PSA level in the blood is the first test for prostate cancer detection in its early stages. However, the test is problematic, since a small percentage of men who do have prostate cancer will not have a raised PSA level and PSA levels tend to rise in all men as they get older. A second test to detect prostate cancer is digital rectal examination (DRE). The rectum is close to the prostate gland, so the clinician can feel for any abnormalities in the prostate by inserting a gloved finger into the rectum. If cancer is present, the gland may feel hard and knobbly, whereas with benign prostatic conditions the gland is usually enlarged, firm and smooth [from: http://www.macmillan.org.uk/]. However, in some cases, the cancer causes no changes to the gland and a DRE may not be able to detect the cancer.

Because the PSA and DRE tests are indicators of cancer but not diagnostic, other

tests are needed to complete the cancer diagnosis. Imaging of the prostate is used for a more accurate diagnosis and localization of prostate cancer tissues. MR imaging is currently the best imaging modality for prostate cancer detection, owing to its higher soft tissue contrast than other imaging techniques. However, because diagnosis by MR imaging alone is not sufficiently robust, biopsy is ultimately necessary for confirmation of suspected cancer and to determine the optimal treatment.

Transrectal Ultrasound-guided biopsy (TRUS) is the standard technique for prostate biopsy, owing to its low cost, simplicity and wide availability [Presti, 2000]. However, because it suffers from poor soft tissue contrast and therefore cannot differentiate previously identified suspected cancer lesions [Terris, 1999], TRUS is normally performed with the support of the previously acquired diagnostic MR images (Figure 3.1) and it requires the collection of several samples, with the risk of spreading the cancer cells and high distress for the patient. Alternatives to TRUS-based guidance are therefore needed. MRI offers high sensitivity, high spatial resolution and excellent soft tissue contrast. Using MRI for guidance has hence been a natural choice and several MRI-guided prostate biopsy approaches have been reported.

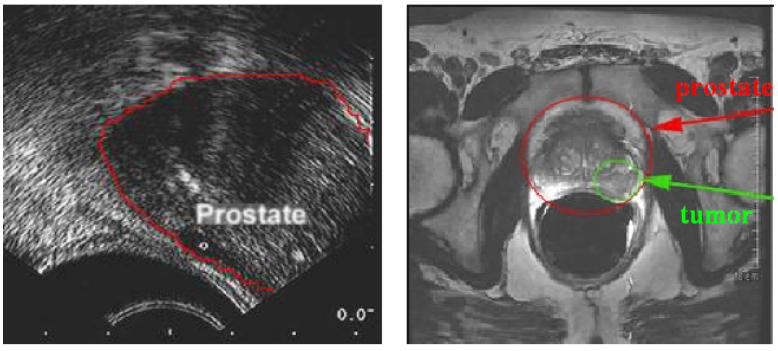


FIGURE 3.1: TRUS (left) and MRI (right) images of the prostate.

3.1.2 Previously proposed MRI-guided prostate biopsy systems

The main challenges in developing an MRI-guided prostate biopsy system are the spatial limitation inside conventional closed-bore MR scanners and the MR compatibility of the components. In order to overcome the spatial limitation, first MRI-guided prostate biopsy systems were designed for open scanners [Cormack and D'amico, 2000][Tempany and D'amico, 2000]. Unfortunately, open scanners suffer from reduced SNR, due to low field strength, and consequently from low image quality. Therefore, for a reliable identification of the targets, MRI-guided prostate biopsy should be preferably performed in a higher field closed-bore scanner and robotics may assist in overcome the limited space problem.

Proposed MRI-guided prostate biopsy systems are normally classified according to

the access to the prostate: transperineal, transrectal or transguteal. The transrectal approach is considered the less invasive, it does not require anaesthetics and it is technically straightforward [Di Maio and Fisher, 2006]. For these reasons, transrectal biopsy is generally preferred.

Beyersdorff et al. [2005] and Engelhard et al. [2006] described the use of a stereotactic device for MRI-guided transrectal prostate biopsy (InVivo Germany GmbH, Schwerin, Germany) in a closed-bore MR scanner, with the patient in the prone and in the supine position, respectively. The device has three degrees of freedom (rotation, insertion and height) and a needle guide filled with Gadolinium for passive tracking (Figure 3.2). Once the patient is in the scanner, MR images of the prostatic area are acquired by using a pelvic coil. The target is then selected and two perpendicular slices are acquired to determine the needle guide location in relation to the target. Dedicated software computes the needed adjustment in position and angulation of the needle guide in order to reach the target. Initial trials were reported as successful, however quantification of the targeting error was not found in the literature. The main disadvantage of these systems is that localization of the material-filled needle guide is performed using two perpendicular imaging planes resulting in a time-consuming localization technique. Also, the patient has to be withdrawn from the scanner to perform the biopsy, which results in a cumbersome procedure which takes time and limits the accuracy of the MRI-guidance.

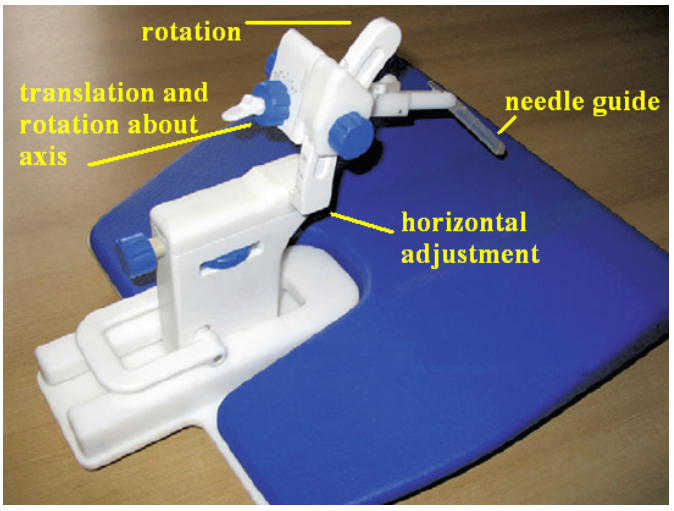
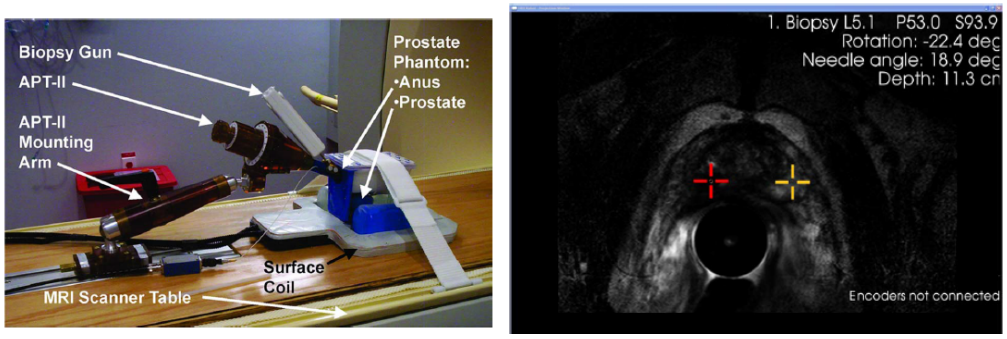


FIGURE 3.2: MRI-guided transrectal prostate biopsy device. InVivo Germany GmbH, Schwerin, Germany [Beyersdorff et al., 2005] and [Engelhard et al., 2006].

[Elhawary et al., 2010] proposed a robotic system with piezoceramic motors for a patient in the lateral position. The whole procedure was intended to be performed with the patient inside the scanner. The biopsy probe incorporated a surface coil and two semiactive markers. The system used two scan planes, sagittal plane and plane through the markers, for automated tracking of the probe. An update rate of about 0.5 frames

per second was reported. Unfortunately, clinical results showed that the targets located in the peripheral zone of the prostate were not accessible because of the limitations in the angular movements of the probe due to the mechanical design of the robot and probe design.

Recently, Krieger et al. [2011] reported an endorectal probe with integrated single-loop imaging coil, a steerable needle channel and four passive markers, as shown in Figure 3.3. Initial registration of the device within the imaging space was accomplished by segmenting in volumetric sagittal MR images four passive markers, two incorporated into the probe and along its axis, and two placed coaxially with the needle guide. Dedicated software provides the parameters for placement of the needle and it tracks orientation and position provided by fiber-optic sensors, while the needle guide is moved towards the target. Similarly to Beyersdorff et al. [2005] and Engelhard et al. [2006], after target selection on the acquired MR images, the patient table is withdrawn from the scanner and the biopsy is performed out of the magnet bore. Targeting error was about 3 mm while the average procedure time was about 76 minutes. Such long procedure (TRUS procedure time is about 20 minutes [Tru, 2012]) was probably due to the time-consuming localization technique as well as to the workflow of the procedure which requires withdrawing of the patient from the scanner.

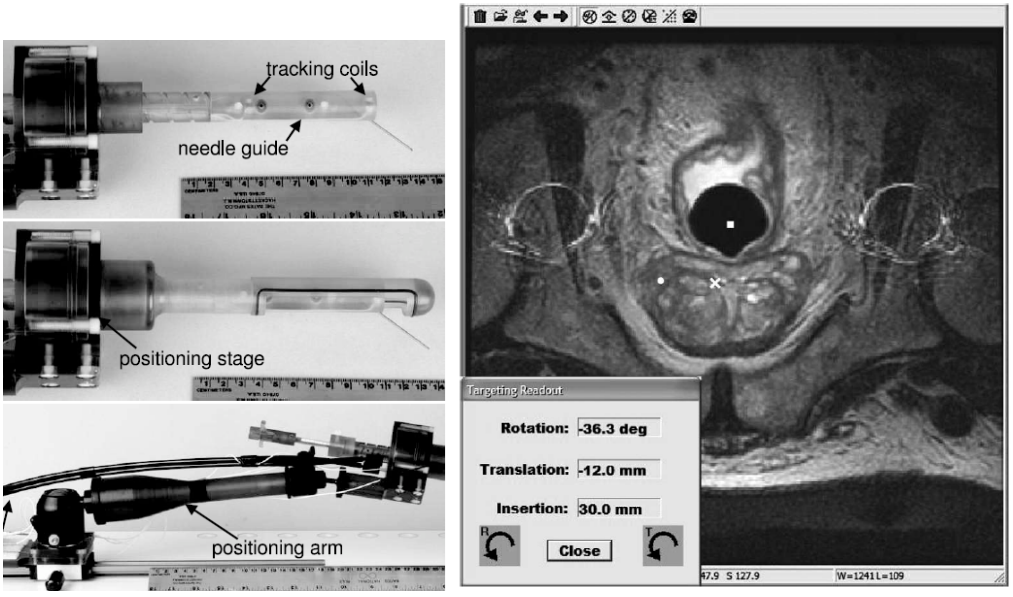


(a) (b)

FIGURE 3.3: MRI-guided transrectal device for MRI-guided transrectal biopsy [Krieger et al., 2011].(a) The device is shown inserted in a prostate phantom. (b) Targeting program. The red cross is the currently selected target. Rotation, needle angle, and insertion depth are displayed to reach the current target. The yellow cross is another target.

Previously, Susil et al. [2006] employed active markers localization for a similar device. Three active markers were embedded within the probe and a 1D projection tracking sequence was employed for their localization, as shown in Figure 3.4(a). By knowing the position of the target and the pose of the needle guide, necessary rotation and translation to bring the needle trajectory through the target were calculated by dedicated software and displayed, as shown in Figure 3.4(b). While the clinician moved the probe, by

means of extended knobs, the targeting parameters were updated. A targeting accuracy of about 2 mm was reported. However, once the probe was in the correct position, the patient table was withdrawn from the scanner to allow insertion of the biopsy needle. Also, the use of active markers introduced complexity and safety hazards. More details about the employed tracking method are reviewed in Section 3.2.



(a) (b)

FIGURE 3.4: MRI-guided transrectal device for MRI-guided transrectal biopsy [Susil et al., 2006]. (a) The tracking coils, the imaging coil and the positioning arm are shown. (b) Graphical user interface. Rotation, translation, and insertion depth to reach the target are displayed.

3.2 Localization methods

Localization of a medical instrument within the MR imaging volume is essential to provide MRI-guidance. A number of different approaches has been reported in the last 30 years as a result of the increased interest in MRI-guided interventions [Wendt and Wacker, 2000]. These may be classified in mechanical digitizers, optical systems and MR fiducial markers.

Mechanical digitizers, consisting of a mechanical arm equipped with joint position sensors, were the main technology adopted in early tracking of devices [Maciunas et al., 1992]. However, due to the cumbersome handling of such devices, optical position sensors using a camera to detect infrared light emitted by markers mounted on the device quickly replaced them [Khadem et al., 2000] [Schmerber and Chassat, 2001] [DiMaio et al., 2007].

Optical systems are considered to be more flexible and accurate than mechanical

digitizers but they do require an unobstructed line of sight between the sensor and the markers; this is difficult to ensure within a conventional closed-bore MR scanner and, especially, in tracking of instruments within the patient's body. This key limitation led to investigation of alternative solutions which might be employed to localize internal medical devices with minimal restrictions in setup and range of movements of devices. Efforts have been undertaken towards a localization method which could benefit from simple interfacing with the MR scanner, MRI technologies and MR properties of materials. The current approaches to localization by using MRI are generally classified on the basis of the employed MR fiducial markers: passive, active and semiactive markers.

3.2.1 MR markers localization

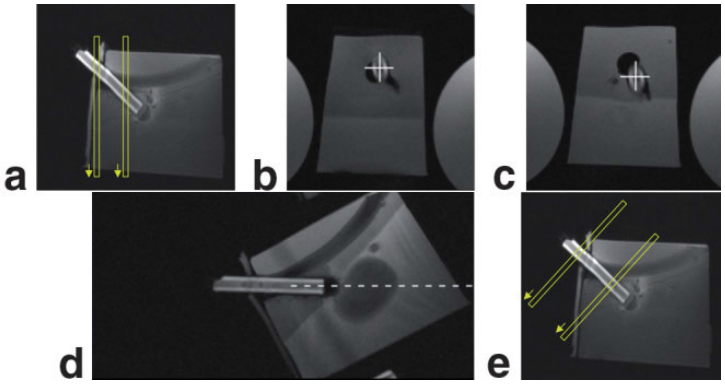
3.2.1.1 Passive markers

This approach attempts to locate a device by means of its associated signal voids or by incorporating passive fiducial markers into the device to generate susceptibility inhomogeneity or positive contrast (e.g. using GD-DTPA) [Smits et al., 1999] [Omary et al., 2000] [Susil et al., 2003] [Seppenwoolde et al., 2003] [De Oliveira et al., 2008] [Beyersdorff et al., 2005]. The major advantage of employing passive markers is that there is no wire connection to the MR scanners and hence there is no risk of induced RF heating and no interference with the interventional procedure. However, this approach generally suffers from low contrast and low resolution and it depends upon the imaging sequence, resulting in a time-consuming localization scheme.

Beyersdorff et al. [2005] reported an MRI-guided transrectal needle biopsy system which employs a passive fiducial marker sleeve coaxial with the biopsy needle. The biopsy needle was guided by using half-Fourier rapid acquisition (RARE) with acquisition in two perpendicular scan planes. De Oliveira et al. [2008] developed a biopsy needle holder which includes a cylindrical template filled with contrast agent identified by means of phase-only-cross-correlation algorithm (POCC) in two slices perpendicular to the biopsy needle. Figure 3.5 shows the passive marker and the stages of the localization method. This approach resulted in an improved tracking speed and permitted automatic scan plane update at a rate of about one image per second. Seppenwoolde et al. [2003] exploited the idea of gradient compensation for depiction and tracking of paramagnetic susceptibility markers. The positive contrast was the result of dephasing of background signal by slice selection gradients, whereas signal in proximity to the marker was maintained by a dipole field induced by the marker which compensates for the dephasing gradients.



(I)



(II)

FIGURE 3.5: Passive tracking in De Oliveira et al. [2008]. (I) The biopsy needle is inserted into the passive marker, which is a cylinder-shaped tube filled with Gd-DPTA. (II) (a) Two FLASH images are initially acquired along the needle axis to localize the marker; (b)(c) The position of the marker in the two images is computed by using POCC (white cross); (d) Real-time trueFISP image showing the estimated biopsy needle direction (dotted line); (e) Tracking slices are repositioned on the basis of the computed location.

3.2.1.2 Active markers

Active markers are resonant coils embedded within a device and connected to a dedicated receiver channel of the MR scanner. A circuit representative of an active marker is shown in Figure 3.6. MR sequences used in localization of active markers employ a frequency-encoding gradient only to acquire a single line of k-space. Since the spatial sensitivity of the micro coil is limited to a small volume, a signal peak is obtained by Inverse Fourier Transform of the acquired line. The position of a peak along the projection indicates the position of the miniature coil along that direction. Localization of one marker in 3D is achieved through acquisitions of an orthogonal set of three 1D projections [Dumoulin et al., 1993].

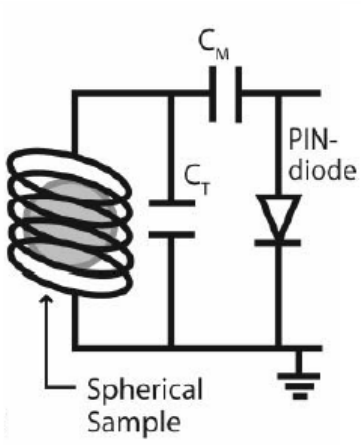


FIGURE 3.6: Active marker circuit. C_m and C_t are respectively the matching and tuning capacitors. The PIN-diode is employed in order to create a decoupling circuit for active-decoupling of the marker in transmission mode.

Active localization is a time-efficient method because only three readouts are needed for localizing one coil. Multiple active markers may be easily localized as each of them is connected to a dedicated receiver channel. Incorporating three or more active markers into an interventional device permits one to determine the position and orientation of the device within the coordinate system of the MR imaging volume.

Connection of the miniature coil to a receiver channel of the scanner provides also a means for active detuning during RF excitation, which ensures that markers do not compromise images. However, potential RF heating due to standing waves along the conductive cables represents an important issue which has limited the use of active markers in the clinical environment [Konings et al., 2000]. In addition, cabling introduces additional complexity in the workflow of the procedure, and challenges in the design of the devices, especially in the case of miniaturized devices such as biopsy needles and catheters. Also, localization of three or more markers requires availability of three or more dedicated channels on the MR scanner in order to connect the miniature coils.

Krieger et al. [2005] and Susil et al. [2006] presented a MRI-guided transrectal biopsy system which uses localization of three active markers integrated within the needle guide and connected to three independent channels (Figure 3.7). To determine the location of the markers, twelve dodecahedally-spaced 1D projections were acquired in about 60 ms. The obtained over-determined linear system was solved by using a Least-Squares algorithm. Data communication and localization were performed in about 150 ms.

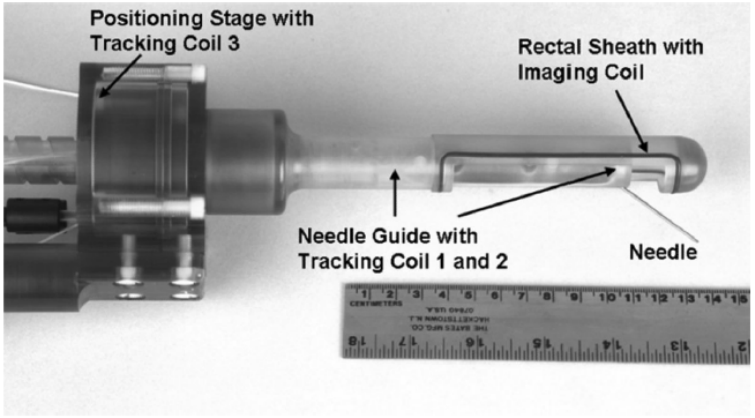


FIGURE 3.7: Needle guide presented in Krieger et al. [2005] and Susil et al. [2006]. The picture shows the imaging coil integrated within the needle guide and the three active markers for localization of the device. Two miniature coils were integrated within the needle guide, the third miniature coil is attached to the rotating part for the positioning stage.

3.2.1.3 Semiactive markers

Semiactive markers are resonant circuits embedded within the device which are not connected to the scanner. They include a miniature coil which is tuned to the Larmor frequency of the MR scanner and filled with an MR visible material having short relaxation time T_1. Similarly to passive markers, semiactive markers may be localized by processing of acquired 2D MR images, with the advantage of significantly higher contrast with respect to the background signal. By applying a fast imaging sequence with low flip angle, high amplitude signal can be generated from the sample within the micro coil, due to local amplification of the B_1 field, in combination with relatively low background signal [Burl et al., 1996].

The use of semiactive markers simplifies design and manufacturing of medical devices, especially miniature internal devices, as well as the workflow of the procedure. Importantly, avoiding multiple conductive structures entering the patient's body with the device minimizes the risk of local heating around the device in high-field MRI systems [Zhang et al., 2001] [Luechinger et al., 2001]. However, semiactive markers might cause increased local specific absorption rate (SAR) values due to their resonant coupling with the RF field during transmission and hence a passive decoupling method may be required [ASTM, 2011]. A major challenge in using semiactive markers is to achieve a sufficient SNR, particularly when the marker is located within the body, as a result of tissue loading.

Thormer et al. [2012] presented a method for simultaneous localization of semiactive markers by image processing. 3D localization was performed with the analysis tool presented in Busse et al. [2007]. The software identifies a marker in an MR image by using

Least-Squares 2D Gaussian template fitting of the signal profiles in segmented regions of the acquired slice. Marker and non-marker signal profiles are distinguished on the basis of SNR and peak shape parameters. 3D localization is performed by identifying signal profiles in 2D on three orthogonal planes and then matching the computed peaks' coordinates to a 3D set of points. Update rate was one per second with an accuracy of 1 mm.

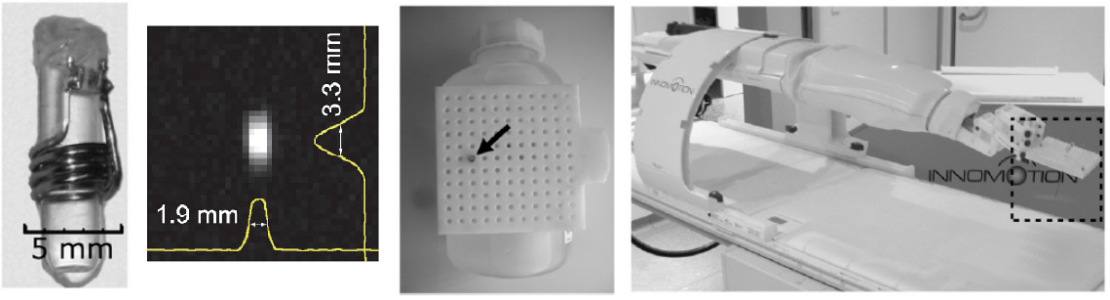


FIGURE 3.8: Localization of multiple semiactive markers in Thormer et al. [2012]. From the left: semiactive marker consisting of a water-tube, a solenoid and a chip capacitor; marker MR image and signal profile (TrueFISP, flip angle 0.3, transversal view); setup for accuracy measurement showing a marker board mounted on a robotic manipulator (Innomotion).

Similarly to active markers, semiactive RF markers may also be localized using 1D projections [Flask et al., 2001]. The use of 1D projections lends itself to much faster high-resolution data acquisition and processing than image processing; however, more complex algorithms are needed in order to reconstruct the original positions of multiple wireless markers.

Flask et al. [2001] implemented an algorithm for localization of N semiactive makers which uses a limited set of five 1D projections in two orthogonal scan planes. Semiactive markers were made of plastic screws with an internal oil sample and an external resonant circuit. A radial k-space FISP non-selective sequence was designed with a low-flip-angle non-selective pulse. N peaks were identified in each 1D projection by means of discrete differentiation formula and minimum SNR requirement. If any of the N peaks did not meet the requirement, the entire projection was discarded and a new one acquired instead.

The location of all potential markers were reconstructed in 2D by back projecting the identified peaks. N^2 intersections were selected as reference points on the basis of the largest distance separating two closest peaks and closest-points sets were generated around each reference point by searching for the closest intersection points. The centroids of the N densest closest-point sets were used to represent the locations of the N markers in the plane. Finally, the 3D coordinates were determined by pair-matching of the points having common coordinate in the two orthogonal planes, a solution which would arise issues in the case of multiple points with the same coordinate.

A maximum error of 3 mm was reported for a low-field strength of 0.2 T and the time needed to acquire a set of data was about 200 ms. Computational time may be considerably reduced by finding a faster solution than cluster analysis and which does not reject 1D projections with less than N peaks. The work presented by Flask et al. [2001] will be the main reference in the localization algorithm proposed in this thesis.

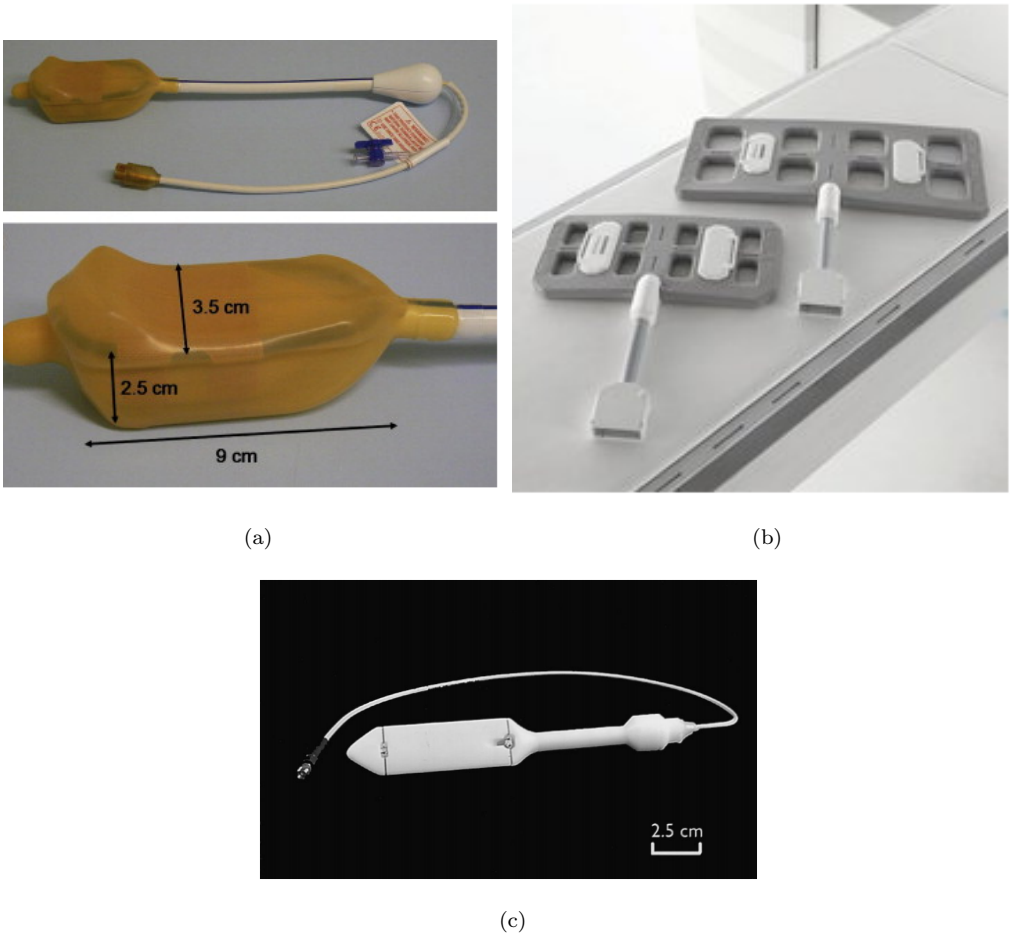
3.3 Receivers for intraoperative prostate imaging

Completion of MRI-guided transrectal prostate biopsy requires tracking of the biopsy needle overlaid on anatomical MR images of the prostatic area. Also, when the biopsy needle tip is at about the suspect lesion, tracking should be interleaved with anatomical imaging, in view of the tissue movements [Tadayyon et al., 2011]. In order to complete successfully the intervention, high resolution imaging is essential and hence an optimized receiver is desirable.

The combination of an endorectal balloon RF coil with an external pelvic coil is the standard for highest quality diagnostic imaging of the prostate (Figure 3.9 (a) and Figure 3.9 (b)). Endorectal balloon coils are inflatable coils which can be easily inserted and comfortably placed in proximity of the prostate before inflation [Bloch et al., 2004]. The inflation of the balloon after internal positioning increases the sensitivity and the mechanical rigidity of the coil, although this alters the coil configuration and therefore re-tuning and matching in situ are required. Unfortunately, endorectal balloon coils are unsuitable for MRI prostate biopsy procedure because of the incompatibility of their design with the requirement of a biopsy needle channel and also because of the significant restrictions they would pose to the range of movements of an endorectal probe [DeSouza and Gilderdale, 1996].

Surface rectangular coils which are solid and reusable were proposed by DeSouza and Gilderdale [1996] as detectors in MRI diagnosis of prostate cancer (Figure 3.9(c)). Compared to the inflatable coils, they ensure fewer artefacts, less position alteration and exclude the necessity of external tuning and matching as there is no change in their configuration. In addition, they are suitable as detectors in MRI prostate biopsy, as they can be easily incorporated into the head of an endorectal probe containing a needle channel [Krieger et al., 2011] [Elhawary et al., 2010] [Susil et al., 2006]. While their sensitivity is lower than the sensitivity of balloon coils, due to acceptable coil sizes within a probe, they have the advantage of generating fewer artefacts and of higher rigidity. Also, external tuning and matching are not needed as there is no change in their configuration. Unfortunately, they have the important disadvantage of restricted range of movements of the probe, making it difficult to reach targets located in the peripheral zone of the prostate.

In order not to limit the range of movements of the endorectal probe, the alternative of using the pelvic coil alone has been considered by numerous groups [Beyersdorff et al., 2005] [Engelhard et al., 2006]. This is however not ideal because of the low sensitivity over the prostatic area. The sensitivity is furthermore reduced by the fact that the back element of the array is to be positioned higher along the back of the patient than in diagnostic imaging, in order to give space for insertion of the endorectal probe.



(a) (b)

(c)

FIGURE 3.9: Receivers for prostate imaging.(a) Endorectal balloon coil, (b) Flexi-elements and (c) Solid endorectal coil [DeSouza and Gilderdale, 1996].

3.4 Conclusion

The use of MR imaging in prostate biopsy not only yields excellent soft-tissue contrast to localize target lesions but can also help in guiding the needle. In addition, the use of robotic devices to perform the intervention can be valuable to overcome the spatial constraints within the MR scanner and to align the needle guide with the target lesion. A limitation common to numerous previously proposed MRI-guided prostate biopsy systems is that the patient has to be withdrawn from the scanner in order to

perform the biopsy. This means a cumbersome procedure which takes time and limits the accuracy of the MRI guidance. In terms of visualization software, reviewed systems provide a 2D display with functionalities such as target selection, distance to the target and movements required in order to align the needle along a preferred trajectory. These functionalities may be sufficient to complete the procedure; however, the lack of depth and dynamic functionalities result in a slow nonintuitive manipulation of the probe.

Several methods for instrument tracking within the MR scanner have been developed in the last twenty years and research is ongoing towards optimized solutions. A fast localization method is crucial to minimize inaccuracies due to target and instrument movements and to enable navigation functionalities. Passive markers offer enhanced safety and flexibility; however their localization requires time-consuming image processing algorithms, primarily because of the low signal against the background. Active markers have the advantage of providing high signal against the background noise; however, they have found limited application in the clinical environment, due to safety hazards and design considerations. Similar to active markers, semiactive markers may be localized at a high update rate using 1D projections and a low flip angle, with the advantage of safety and flexibility; however, so far, only a few efforts have been made to employ 1D projections for semiactive marker tracking, probably because of the difficulty in achieving a fast and robust localization concept.

A major challenge in designing an endorectal probe for transrectal prostate biopsy intervention is the accessibility to the suspected lesions located at the inferior end of the prostate gland. This is a fundamental issue, as patients with such lesions are considered by the specialists to be the most important candidates that would benefit from MRI-guided biopsy. The main cause of this limitation is the use of surface receiver coils placed within the probe. Endorectal surface coils inevitably restrict the mechanical movements of the probe because of their diameter and need for stability. In many cases clinicians use the pelvic array only; however, this does not provide sufficient sensitivity in the region of interest and tends to obstruct placement of the manipulator and insertion of the endorectal probe.

Chapter 4

RF markers and 1D projection analysis

In interventional MRI, RF fiducial markers are employed to locate the medical instrument within the imaging volume. Semiactive markers are normally preferred over active markers, owing to their higher safety and flexibility; however, localization of semiactive markers is most often based on time-consuming 2D image processing [Thormer et al., 2012]. Methods involving 1D projections have so far been poorly explored and faster and more accurate solutions might be developed [Flask et al., 2001]. In this thesis, a novel method for localization of N semiactive markers using 1D projections is presented. In addition, the method may be employed to localize active markers when only one receiver channel is used.

This Chapter describes the construction of the RF semiactive markers and the MR sequence which was developed to acquire 1D projections. The algorithm implemented for detection of the signal peaks along a 1D projection is explained and an analysis of the peaks' amplitude and accuracy in various conditions is presented. The suitability of the constructed markers in the clinical application is also investigated, in terms of safety and possible artefacts due to coupling of a marker with the transmitter. The results presented in this Chapter were obtained in a 1.5 T Siemens Avanto MR Scanner (MRI unit, Royal Mardsen Hospital, London) and in a 2.9 T Siemens Verio MR Scanner (MRI unit, Hammersmith Hospital, London).

4.1 RF semiactive markers

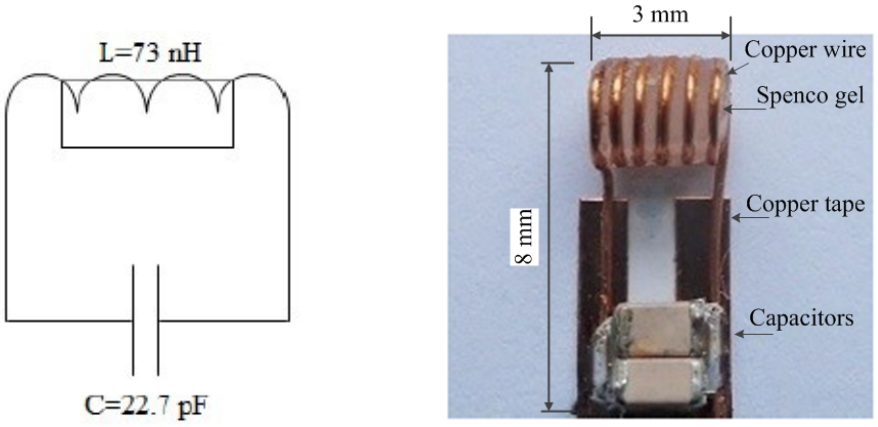
RF semiactive markers were constructed similarly to Garnov et al. [2011] and Rea et al. [2009], consisting of 3 mm diameter wireless miniature coils tuned to the Larmor

frequency of a 2.9 T MR scanner and filled with high ^1H density material. The miniature resonant circuit was constructed by hand-winding 6 turns of insulated copper wire (diameter=0.4 mm) around a 2.0 mm diameter cylindrical former. To allow fine tuning, small gaps were left between the turns. The resulting solenoid, having an inductance of about 73 nH, was soldered to two narrow thin copper strips and a non-magnetic chip capacitance of about 22.7 pF was connected in parallel to produce a resonance in the region $\nu = 42.58 \times 2.9 = 123.5MHz$ (Equation 2.2).

$$f = \frac{1}{2\pi\sqrt{LC}} = \frac{1}{2\pi\sqrt{73 \times 10^{-9} \cdot 22.7 \times 10^{-12}}} = 123.64MHz \tag{4.1}$$

In order to generate MR signal, the solenoid was filled with vinyl plastisol gel material (vinyl plastisol gel, Spenco Healthcare, Horsham, UK). The solid gel was cut into approximately a 1.5 mm-sided cube and inserted into the centre of the solenoid. Because of the loading due to the gel, the resonance frequency generally decreased of about 0.1 MHz.

A Vector Network Analyzer (Anritsu MS 2026A VNA Master) was used to fine tune the RF marker to 123.5 MHz by using inductively coupled test coils connected to reflection and transmission channels, respectively. The miniature coil was gently squeezed before fixing it and sealing it using superglue. The complete RF marker measured around $3 \times 3 \times 8$ mm and a sample is shown in Figure 4.1.



(a) (b)

FIGURE 4.1: Miniature RF wireless marker. (a) Circuit and (b) Constructed marker.

Several RF markers were constructed following this procedure and their properties are summarized in Table 4.1.

TABLE 4.1: RF markers electrical properties. Larmor frequency 123.5MHz.

RF marker	1	2	3	4	5	6
ν(MHz)	123.7	123.2	123.5	123.6	123.2	123.3
Q	120	123	126	125	125	119

The majority of the experiments presented in this thesis were carried out on a 2.9 T MR scanner due to scanner availability. However, as the MRI-guided transrectal prostate system was intended to be demonstrated in a 1.5 T Siemens Avanto MR scanner (Royal Marsden Hospital, Sutton, London, UK), markers for 1.5 T were also constructed. In this case, a non-magnetic chip capacitance of about 106.8 pF was connected in parallel to a solenoid to produce a resonance in the region $\nu = 42.58 \times 1.5 = 63.87MHz$. The electrical properties of the RF markers are summarized in Table 4.2. It can be noticed that the Q-factor for these markers is slightly lower due to the lower resonance frequency.

TABLE 4.2: RF markers electrical properties. Larmor frequency 63.87MHz.

RF marker	1	2	3	4	5	6
ν(MHz)	63.75	63.85	63.65	63.71	63.80	63.82
Q	97	101	108	95	100	98

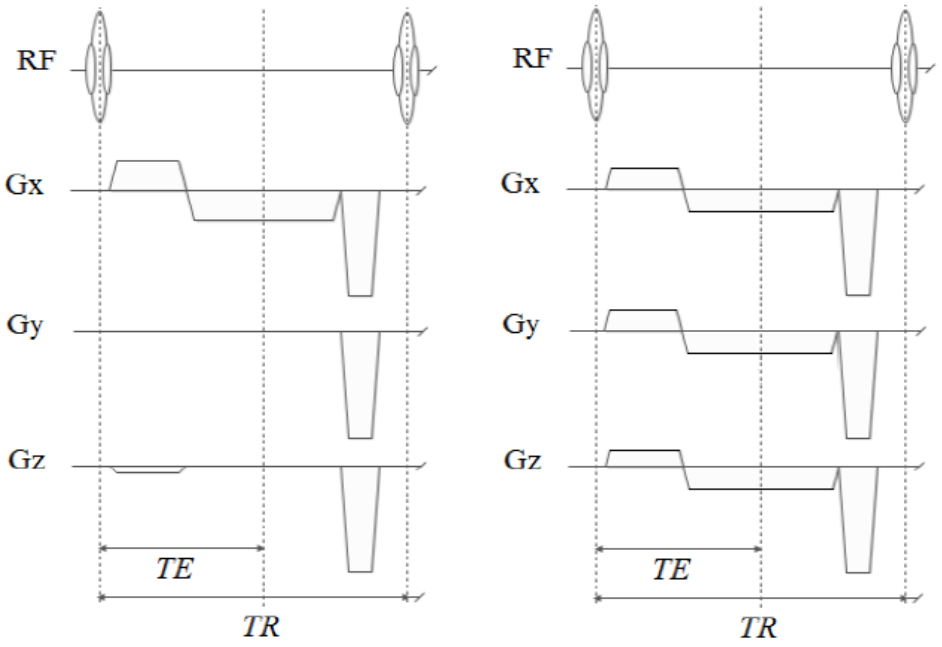
4.2 MR sequence

The code of a 2D imaging Gradient Echo sequence (FLASH sequence on Siemens MR scanners) was modified in order to acquire a predefined set of 1D projections in space. The image reconstruction pipeline of the MR scanner was programmed to send the acquired data to the host computer just after Inverse Fourier Transform.

The customized MR sequence includes a number of RF pulses which is equal to the number of pre-defined 1D projections. In Figure 4.2, selected parts of the sequence diagram are presented. The two sections shown were implemented to acquire, respectively, a 1D projection along the x axis (Figure 4.2(a)) and a 1D projection along an oblique line (Figure 4.2(b)). Each RF pulse is followed by a bipolar gradient which is applied along the direction of projection. A dephaser gradient is also applied in a direction orthogonal to the projection to reduce the signal from the background. Before the next RF pulse, spoiler gradients are applied along the three main axis to cancel residual transverse magnetization. For each 1D projection, $TR = 5.6$ ms.

The complete set of 1D projections is reported in Table 4.3. This set was chosen because it maximizes robustness and accuracy in markers localization, as explained in Section 5.2.1. The complete set of projections is acquired in 72.8 ms.

The customized MR sequence allows setting of additional parameters from the user interface of the MR host computer. These are: flip angle of values lower than 1°, amplitude of the dephaser gradient and time interval in between 1D projections. While the latter parameter was useful in developing and testing the localization method, the first two parameters must be adjusted for different magnetic field strengths, for markers with different electrical properties and for different phantoms or patients.



(a) (b)

FIGURE 4.2: Sections of the MR sequence. Acquisition of a 1D projection along (1, 0, 0) (a)and along (1, 1, 1) (b). The signal is sampled during the gradient echo, which is generated by applying a bipolar gradient along the direction of projection. An orthogonal dephaser gradient ((0, 0, 1) and (1,1,-2) respectively) is also applied in order to reduce the signal from the background; its amplitude is adjustable from the user interface. Spoilers are applied before the next pulse in order to eliminate residual transverse magnetization.

TABLE 4.3: Directions of the acquired 1D projections.

x	y	z
1	0	0
0	1	0
0	0	1
1	1	1
-1	1	1
1	-1	1
-1	-1	1
1	1	0
1	0	1
0	1	1
1	-1	0
-1	0	1
0	-1	1

4.3 RF signal analysis

4.3.1 Signal amplitude under repeated excitations

In order to correctly detect the signal peaks along a 1D projection, the peaks' amplitude must be above the background noise. It is well known that the resonating miniature coil locally amplifies the excitation field [Burl et al., 1996] and that an applied flip angle α results in an effective flip angle $\alpha_{eff} = Q\alpha$, where Q is the *quality factor* of the miniature coil. By applying a low flip angle α, high amplitude signal can thus be generated from the RF marker, in combination with relatively low background signal.

Simulations were performed in order to investigate the amplitude of the signal peaks, under multiple excitation, in relation to the background noise, for a varying flip angle α. Simulations involved derivation of the transverse component of the magnetization vector at time *TE*, which is directly proportional to the amplitude of the signal peak. Similarly to Hargreaves et al. [2001], the magnetization vector was derived as:

$$\mathbf{M}_{TE} = \mathbf{A} \times \mathbf{M}_i + \mathbf{B} \tag{4.2}$$

where $\mathbf{M}_i$ is the magnetization vector just before an i-RF pulse, $\mathbf{A}$ and $\mathbf{B}$ are matrices representing the RF nutation about the x axis, the precession about the z axis and T_1 and T_2 relaxation processes of the RF marker. Derivation of Equation 4.2 is shown

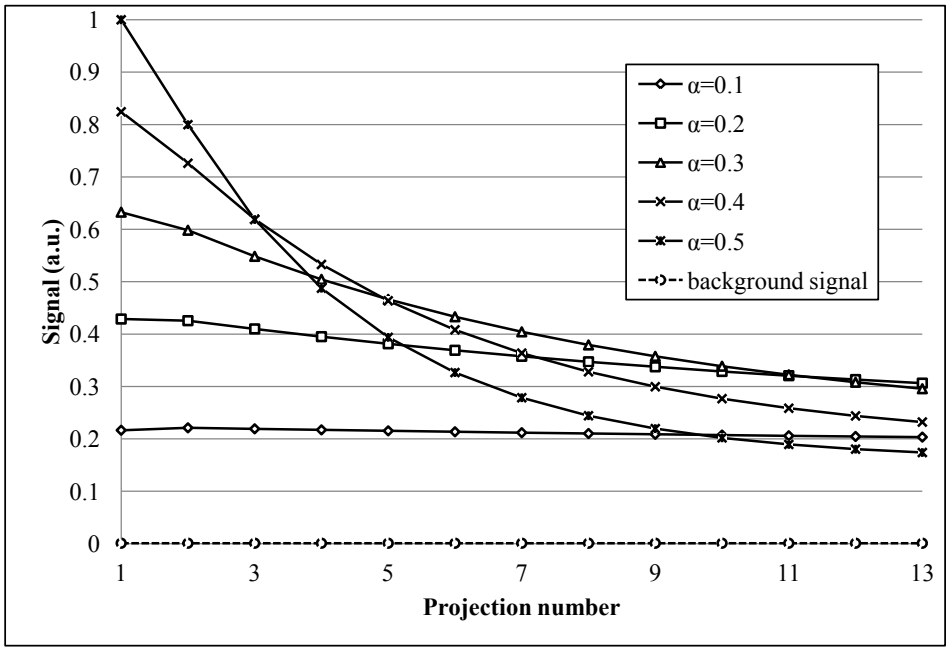
in Appendix A.

The transverse component of the magnetization was computed as magnitude of a vector whose components are $\mathbf{M}_{TE_X}$ and $\mathbf{M}_{TE_Y}$, $\mathbf{M}_{TE_{XY}} = \sqrt{\mathbf{M}_{TE_X}^2 + \mathbf{M}_{TE_Y}^2}$. $\mathbf{M}_{TE_{XY}}$ was simulated for a complete set of 1D projections and for different flip angles α ($T_1 = 190ms$, $T_2 = 14ms$, $TE = 3.5ms$, $TR = 5.6ms$).

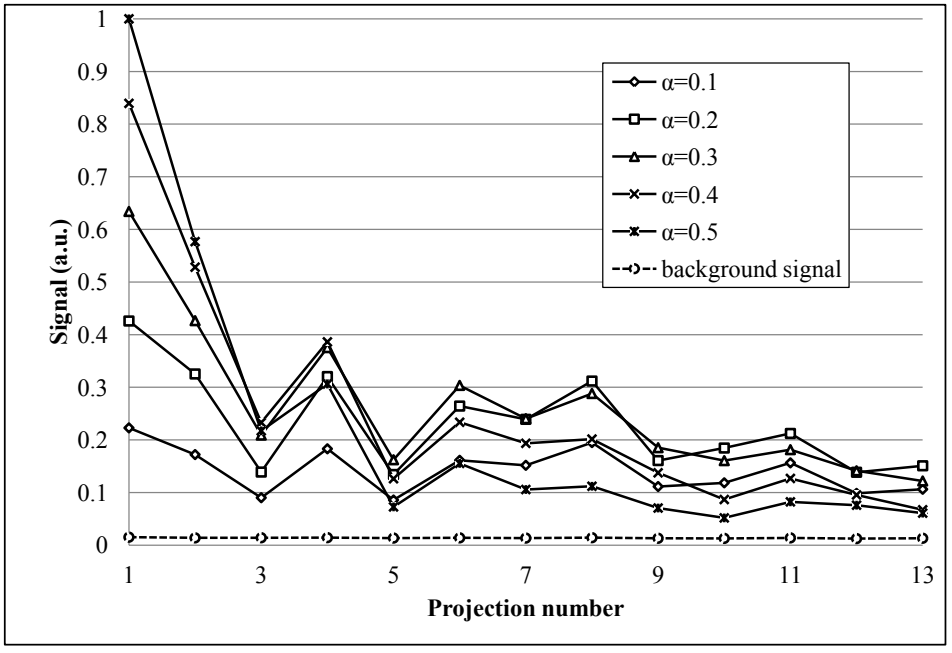
Experimental data were also obtained in a 2.9 T MR Siemens Verio scanner. The marker was placed on top of a 1L water flat phantom and four 1L water bottle phantoms were placed in its proximity to generate higher background signal. The signal was acquired using the body coil. Repeated measurements of a set of 1D projections were acquired with the marker in a fixed position. The amplitude of a signal peak along a projection was computed as average amplitude of the signal peaks over repeated measurement.

Figure 4.3 shows the results of simulations and experiments. It can be noticed that the amplitude of the signal peak approaches the steady state over a set of projections. This is due to the repetition time TR much lower than the longitudinal relaxation time T_1 [Bernstein et al., 2004]. For higher α, the amplitude appears initially larger; however, for the subsequent projections, it quickly drops and reaches values similar to the background signal. For $\alpha = 0.2°$, the amplitude shows the highest minimum value. This was valid for both experiments and simulations and very similar results were obtained for all the manufactured markers. In addition, the experiments show a noticeable oscillating trend. This was found to be highly repeatable and dependent on the direction of projection, therefore it was attributed to an asymmetry of the markers.

Importantly, in the clinical environment, the loading due to a person may result in a decrease in the amplitude of the signal peaks and, consequently, may affect the performance of the system. This situation was tested in a 2.9 T MR scanner by placing three semiactive markers inside the biopsy probe developed within the project (Chapter 6), which was, in turn, tightly held by a volunteer in between his legs. An overall decrease in the peaks amplitude was observed; nevertheless, the signal peaks were well above the background signal and the trend was highly similar to the trend observed with the previous setup.



(a)



(b)

FIGURE 4.3: RF signal amplitude under multiple excitations. (a)Simulated and (b) Experimental RF signal for different applied flip angles α. Each point in (b) represents an average of 20 measurements. For values of α lower than $\alpha = 0.8°$, the background signal did not show any significant increase.

4.3.2 Peak detection and sub-pixel localization

Inverse Fourier transform of a 1D projection produces a signal with peaks that correspond to the positions of the markers. An example of 1D projection is shown in Figure 4.4. Correct identification of the peaks is essential for the success of the localization algorithm.

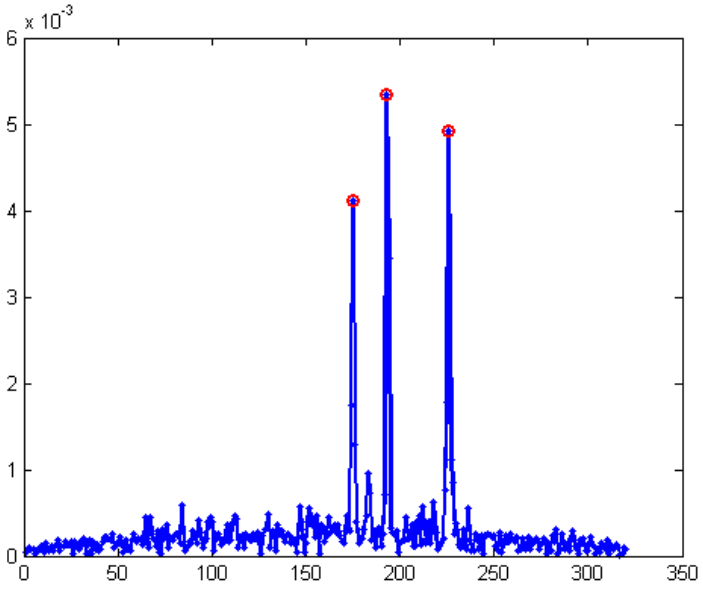


FIGURE 4.4: 1D projection for three markers in the MR scanner. The direction of projection is (-1,1,1). The three detected peaks correspond to the location of the RF markers along the direction.

The presence of background noise in the acquired MR signal makes simple thresholding inadequate for robust peak detection. Following the method suggested by Flask et al. [2001], peak detection starts with a search through the sequence of values in a 1D projection to identify local maxima using discrete differentiation. The N largest peaks, with N equal to the number of employed RF markers, are checked against an experimentally determined threshold equal to 2.5×maximum background noise. The maximum background noise is computed after removing each of the N peaks and their adjacent four points on either side. Only the peaks satisfying the threshold are accepted.

In order to achieve higher accuracy in peak detection, the location of a peak is then corrected by applying an algorithm for sub-pixel peak detection. This was achieved using Gaussian interpolation, as suggested by Fisher and Naidu [1996]. The Gaussian interpolation uses signal amplitude value b at the location of the highest signal amplitude, x, and the signal amplitudes a and c at the adjacent positions on the left and on the right side of it, respectively [Fisher and Naidu, 1996]:

$$\hat{X} = x - \frac{1}{2}\frac{ln(c) - ln(a)}{ln(a) + ln(c) - 2ln(b)} \tag{4.3}$$

The variation in the location of a peak over repeated acquisitions, with the marker fixed in the same position, was explored. This analysis was considered necessary for the subsequent assessment of accuracy and robustness of the localization algorithm and definition of a tolerance value in removing candidate points, explained in Chapter 5.

Chi-square goodness-of-fit test of the null hypothesis that the deviations of the peak location are from a normal distribution [Teukolsky et al., 1986] was performed over repeated acquired 1D projections of a marker using Equation 4.4 [Utts and Heckard, 2006]:

$$\chi^2 = \sum_{i=1}^{N} \frac{(O_i - E_i)^2}{E_i} \tag{4.4}$$

where O_i is the observed frequency and E_i is the expected frequency of bin i.

A marker was placed on top of a 1L water flat phantom and at 8 different distances from the isocentre of the MR scanner, along the x direction and on either side, at consecutive steps of 10 mm. For each position 20 repeated sets of 1D-projections were acquired. Peak localization was performed using the sub-pixel peak detection algorithm. For each projection, the mean position of a peak and the deviations from this value were computed.

The Chi-square goodness-of-fit test proved that the deviations, over repeated acquisitions, are normally distributed. Figure 4.5 shows the expected and the obtained distribution for a sample of acquired data. The standard deviation σ_{peak} of the normal distribution, for the marker at different positions, varied between 0.03 and 0.075 mm. The test was then repeated for a volunteer in the scanner and a marker placed inside the biopsy probe, as in Section 4.3.1; in this situation, the standard deviation was 0.08 mm.

On the basis of this analysis, Monte Carlo simulations of the algorithm, reported in Chapter 5, involved values of σ_{peak} between 0.05 (average value $\bar{\sigma}_{peak}$) and 0.08 mm. It was however recognized that the occurrence of merging of two peaks into a unique peak may present a different situation. This occurrence was therefore investigated.

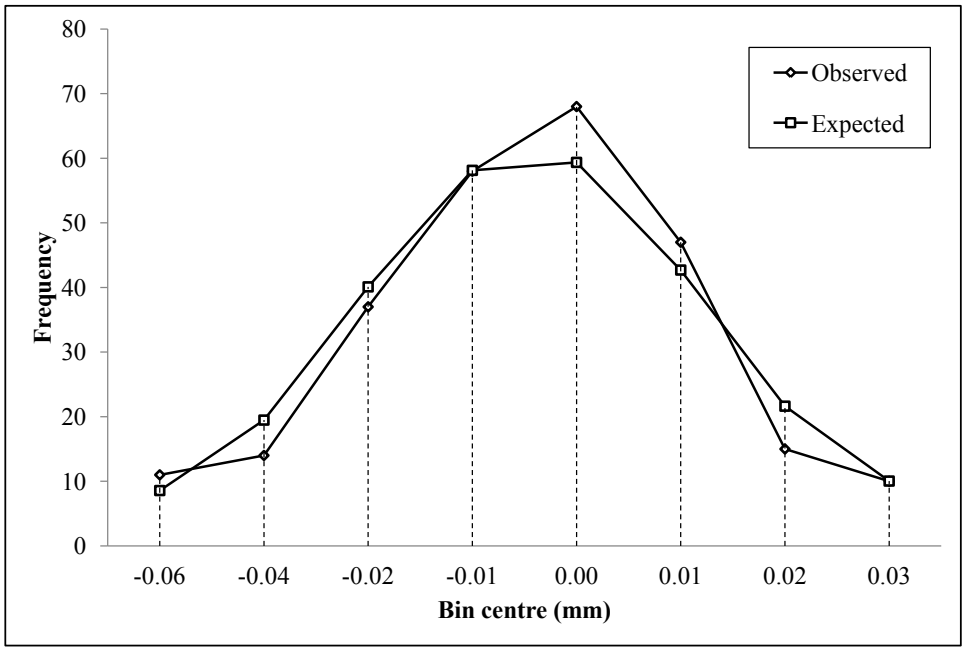


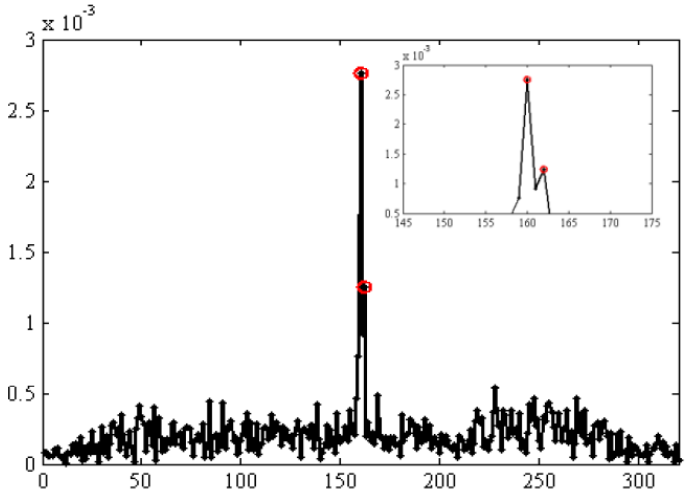
FIGURE 4.5: Normal distribution of the variation of a peak position. A sample of expected and observed frequency of variations from (20 measurements)*(13 1D projections) data is plotted. The expected distribution was given by the expected counts for each bin given the mean value and the standard deviation of the observed variations. The standard deviation of the observed distribution was about 0.06 mm.

4.3.3 Peak merging

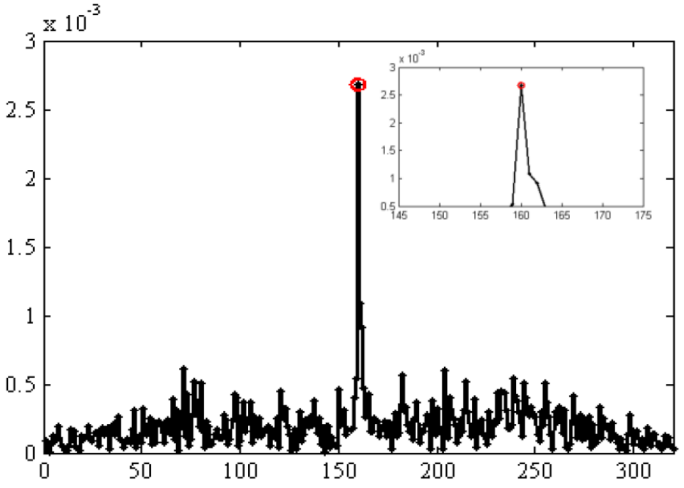
The signal generated by N RF markers along a 1D projection shows multiple peaks which correspond to the locations of the markers along the corresponding gradient direction. The number of peaks may be however smaller than the number of RF markers due to merging of close peaks. Two markers which have the same coordinate along a gradient direction induce signals at a similar frequency [Zhang et al., 2001]; in this situation, the normally separate multiple peaks may be at the limit of the spectral resolution of the system and hence their peaks may merge in some acquisitions and not in others. This occurrence was investigated in order to optimize the choice of the tolerance in the localization algorithm.

A situation of two close peaks is illustrated in Figure 4.6, where two projections on the same direction were acquired while the markers were static. In Figure 4.6(a) two high intensity peaks are evident while in Figure 4.6(b) these peaks have merged into one. It was found that peak merging may happen when peaks are within 2 pixels from one another and that the position of the peak is not affected by merging. In order to

accommodate peak merging, the tolerance was automatically enlarged to two pixels size whenever fewer than N peaks were detected.



(a)



(b)

FIGURE 4.6: Identification of close peaks. (a) Two distinct peaks detected and (b) Single peak detected.

4.3.4 Orientation to the main field

Orientation of the marker to the main field is an important factor to be considered when designing interventional instruments [Burl et al., 1996] [Schenck, 1996]. The signal generated by a marker is the highest when its axis is perpendicular to the main field and reduces as the angle decreases. This is due to the fact that the coupling of the solenoid to the transmit field, and therefore the amplification of the excitation field in its proximity, depends on the orientation of the solenoid; an adverse orientation results into induced signal loss [Garnov et al., 2011]. At some angles, the amplitude of the

signal may be comparable with the background signal and hence peak detection may become unreliable. This was investigated experimentally using a custom made rotary holder to position the marker at various measured angles to the main field.

A marker was placed at the isocentre on top of a 1L water flat phantom and rotated in steps of 10° in the XZ plane. At each step, 20 measurements were acquired and the average amplitude of a peak was calculated and compared to the background signal, as shown in Figure 4.7. For angles up to 50° peaks were always correctly detected for all the projections. At 60° the amplitude of the peak was comparable with the amplitude of the background signal and the peak was correctly detected in about 60% of the cases. The standard deviation in peak location was estimated below 0.07 mm for angles up to 60°.

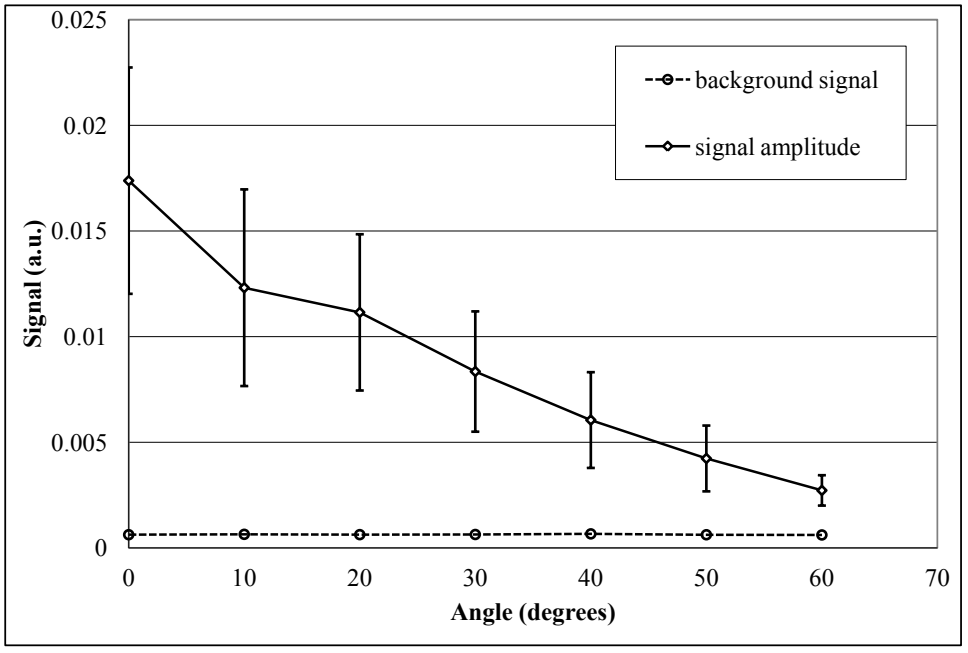


FIGURE 4.7: Signal amplitude at different angles to the main field. The amplitude of a peak decreases for increasing angles. For angles higher than 50° the detection starts to be not consistent.

Accuracy in localizing a marker was also assessed when a marker was rotated in the XY plane, as shown in Figure 4.8. A marker was mounted on a custom-made rotary holder, placed beside a 1L water flat phantom. The marker was rotated through 5 positions in the range $0° - 90°$ and scanned 20 times in each position. A circle was fitted to the resulting 100 points and the distances of the estimated positions from it were calculated.

For the fitted circle goodness of fit was computed as [Utts and Heckard, 2006]:

$$R^2 = 1 - \frac{\sum_{i=1}^{n}(y_i - f_i)^2}{(y_i - y_{avg})^2} \tag{4.5}$$

where f_i is the predicted value from the fit and y_{avg} is the mean of the observed data y_i. The computed value $R^2 = 0.9979$ proves good fitting.

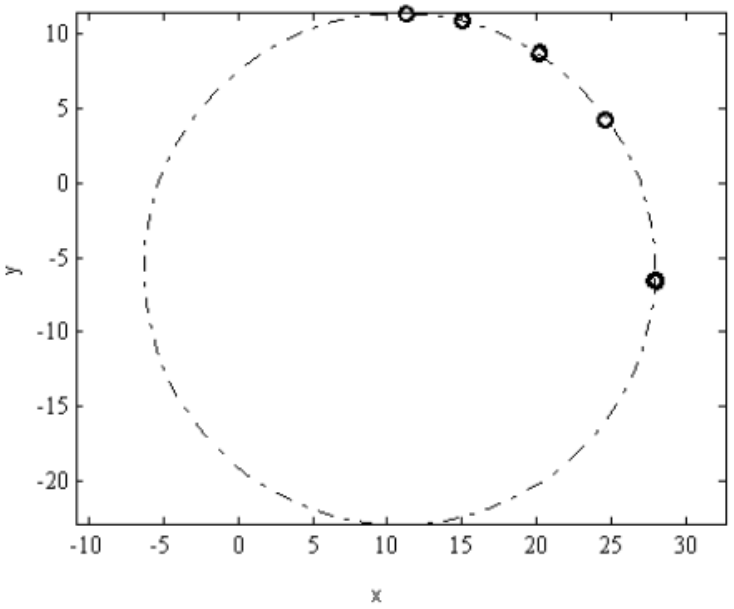


FIGURE 4.8: Marker rotation in XY plane about a fixed centre and fitted circle. Each position is given by 20 points.

4.4 Suitability in interventional MRI

4.4.1 RF markers heating

The potential local heating due to electromagnetic coupling is an important issue to be considered when using RF markers in the clinical environment [Garnov et al., 2011]. Tests were performed in order to verify the temperature rise due to marker heating.

An optic fibre thermometer (Luxtron 812, LumaSense) with accuracy $0.1°C$ was used. Similarly to Garnov et al. [2011], the optic fibre sensor was taped directly on the marker, as shown in Figure 4.9. The marker was placed on top of a 1L water flat phantom and the test was performed in a 1.5 T MR Siemens scanner. The temperature was recorded over 11 minutes, with no RF excitation during the first minute (base line) and RF excitation during the subsequent 10 minutes. The test was performed for a T2-weighted Turbo Spin Echo (TSE) sequence ($SAR = 0.7W/kg$ as reported by the MR scanner), which is the imaging sequence routinely used for prostate imaging, and for the tracking

sequence ($SAR < 0.001W/kg$). The parameters of the TSE sequence were set according to the protocol for prostate imaging at Royal Marsden Hospital (Sutton, London, UK) and they are reported in Table 4.4. The room temperature was equal to 19 ± 0.1 C.

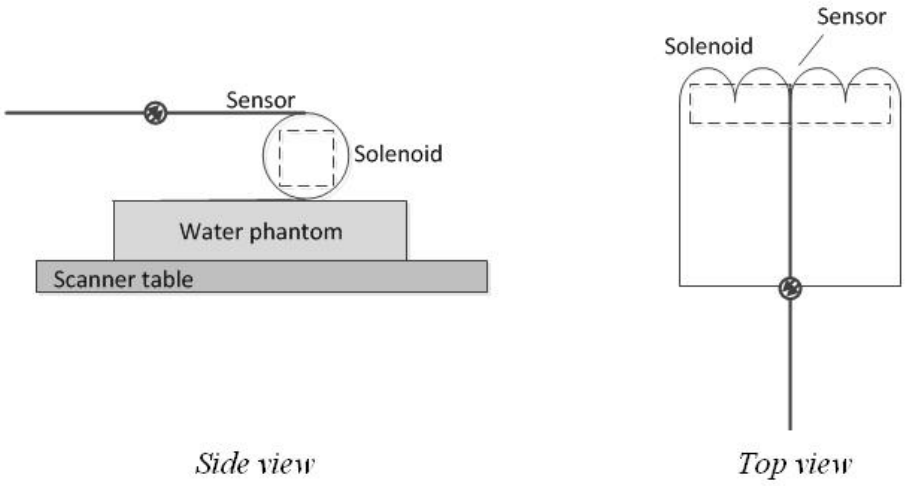


FIGURE 4.9: Setup to measure the marker heating. The optic fibre sensor was taped on top of the microcoil at about its centre.

TABLE 4.4: Parameters of the sequence Turbo Spin Echo.

TR (ms)	3670
TE (ms)	121
Flip angle (°)	137
Slice thickness (mm)	3
Distance factor (%)	10
Base resolution	320
Phase resolution (%)	70
Turbo factor	23

Results are shown in Figure 4.10. The dashed vertical line indicates the start of the RF excitation. The two plots are independent from one another and temperature values must be independently interpreted. It can be observed that for the tracking sequence the temperature drops of about 0.2 C, indicating cooling of the marker towards the scanner room temperature. For the imaging sequence a temperature rise of about 0.2 C at about 360 sec can be observed. The temperature again decreases to the initial values at 600 sec, which indicates that the rise was probably due to a variation in the scanner room temperature.

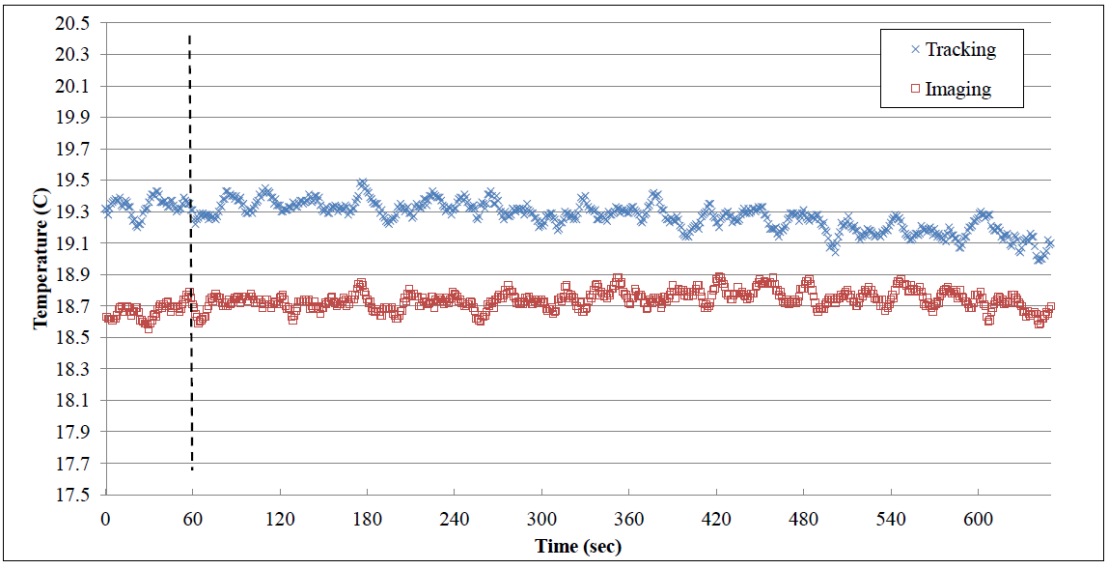
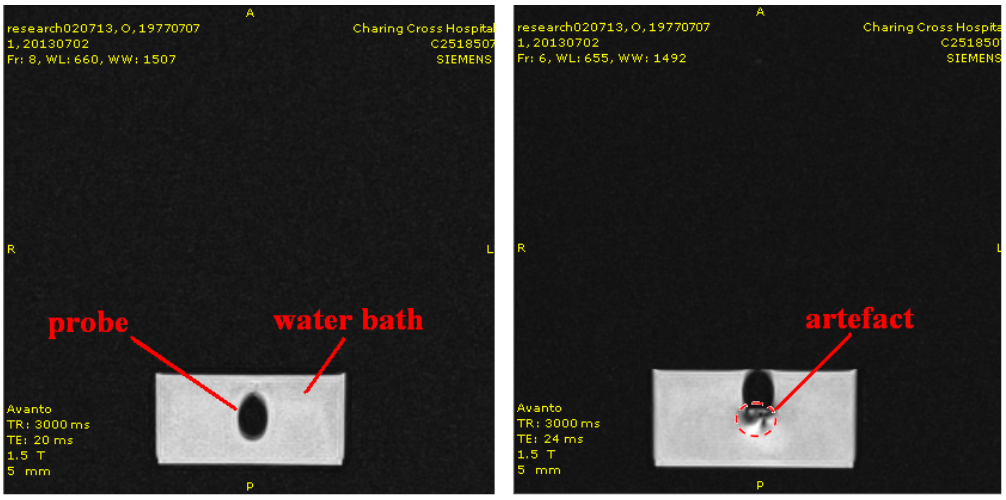


FIGURE 4.10: Local heating of the RF markers. The temperature was measured for tracking and imaging sequences. Sampling time was 1 sec.

4.4.2 Image artefacts

Coupling between markers and the transmitter may cause over-excitation not only of the material within the marker coil but also of signal sources that are in proximity to the solenoid. As a result, anatomical images may present artefacts in the region of the marker. The spatial extent of the perturbation of the local magnetization was investigated.

A marker was placed inside a biopsy probe of diameter 15 mm which was, in turn, immersed into a bath of water. Slices were acquired using T_2-weighted TSE sequence as by prostate imaging protocol without and with the marker inside the probe. Results are shown in Figure 4.11. An artefact can be clearly noticed in Figure 4.11 (b). The artefact radius was estimated about 25 mm from the centre of the marker.



(a) (b)

FIGURE 4.11: Artefact generated by a marker in the images. (a) Transversal slice acquired with no marker and (b) Transversal slice acquired after placing a marker inside the probe.

4.5 Discussion and conclusions

This Chapter described the RF semiactive markers which were constructed for localization of the instrument within the MR scanner. The dimension and flexibility of the markers make them particularly suitable for MRI-guided interventions involving the use of small devices, such as biopsy needle guide. The Gradient Echo sequence which was modified to acquire a set of 1D projections was illustrated. The sequence comprises 13 pre-defined 1D projections and each 1D projection takes about 5.6 ms.

An analysis of the acquired 1D signal, involving both simulations and experiments, was presented. It was found that at 2.9 T the MR signal is maximized when a flip angle of about 0.2° is applied. This value may change for different field strengths and Q-factor; for this reason, it is important that all RF markers that are tracked simultaneously (e.g. during instrument tracking) have similar electrical properties.

Peak detection along a 1D projection was performed using a discrete differentiation formula and by applying an experimentally defined threshold. In order to achieve sub-pixel accuracy Gaussian interpolation was implemented. The variation in the peak position over repeated measurements due to noise was investigated for both a phantom and a person in the MR scanner. In the second situation, higher variation in the peak position was observed. This analysis was essential to assess the localization accuracy and define the tolerance value in the tracking algorithm, as later explained in Chapter 5. For a similar reason, the occurrence of peak merging when two markers are close to each other was explored.

all Analysis of the signal peaks for different orientations of a marker to the main field in the XZ plane showed reliability of peak detection for angles up to about 60°. Reliability for any angle with respect to the z axis in the XY plane was also demonstrated.

Suitability of the markers in the clinical environment was assessed in terms of marker heating and artefact in the anatomical images. Temperature tests were performed for both tracking and imaging sequence and were proved to show a temperature rise within 1 C, which was considered acceptable by the clinical staff. Artefacts generated by a marker on anatomical images had a spatial extent of about 25 mm from the marker centre when a T_2-weighted TSE sequence is used. For the specific application and probe design (Chapter 6), this was considered acceptable by radiographers involved in the project (Royal Marsden Hospital, Sutton, London, UK). In general, artefacts may be minimized by employing a decoupling method, e.g. crossed diodes; however, decoupling would also reduce the signal generated by the marker itself, with consequent low contrast of the signal peak against the background. Another solution might be relocating the marker so that the artefact radius does not extend over the region of interest.

Chapter 5

Localization of N RF markers from 1D projections

Localization of RF fiducial markers within the MR scanner using 1D projections requires an algorithm for reconstruction of the coordinates from the signal peaks. Flask et al. [2001] proposed a method for localizing N semiactive markers in 3D using 1D projections in two orthogonal planes and cluster analysis. Their algorithm requires at least five 1D projections per plane; however, projections with less than N peaks are rejected, so new projections need to be acquired, with a consequent delay in acquisition. Krieger et al. [2007] proposed a method for tracking three active markers in 3D using 12 1D projections and Least-Squares algorithm. The computational time was reported to be 50 ms and the acquisition time 60 ms. It was recognized that a higher update rate could be achieved by developing a localization method which avoids the complexity of cluster analysis, while higher accuracy could be attained by using an optimal, pre-defined set of 1D projections and by improving the peak detection function.

In this Chapter, a novel algorithm for localization of N markers using 1D projections is proposed. The method may be applied to localize either semiactive or active markers, when only one receiver channel is used. More than three markers may be employed in order to improve the localization accuracy. Performance has been characterized through Monte Carlo simulations and experimental studies. Monte Carlo simulations were implemented on the basis of the characteristics of the signal presented in Chapter 4; the experiments were performed in a 2.9 T Siemens Verio MR scanner, involving an MR-compatible moving platform, the constructed RF semiactive markers and the customized tracking sequence.

5.1 Problem statement

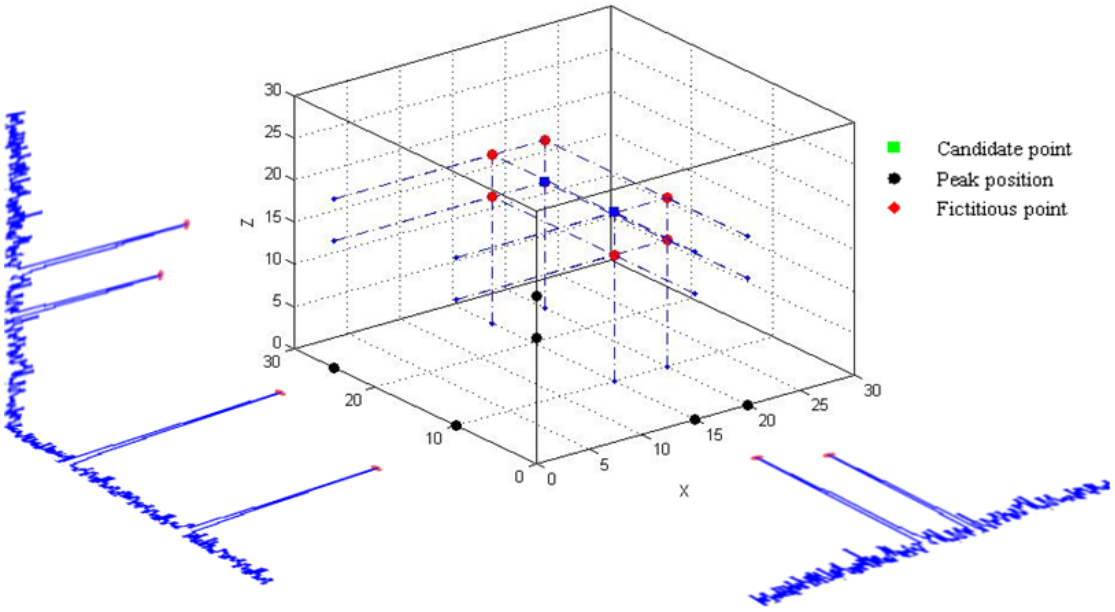
N markers generate N or fewer peaks along a 1D projection. The problem is to compute the 3D coordinates of N markers within a volume by using n 1D-projections.

In 3D, each marker position is defined by the intersection of three planes. Three planes whose normals are not co-planar intersect at a point P [Glassner, 1998]:

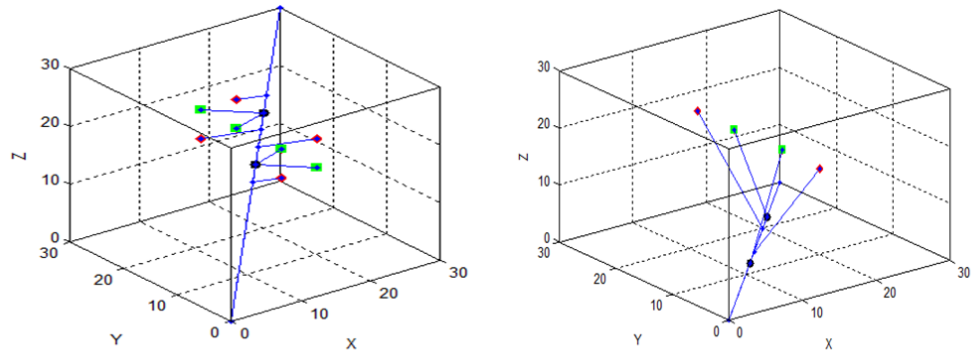
$$P = \frac{p_1(N_2 \times N_3) + p_2(N_3 \times N_1) + p_3(N_1 \times N_2)}{det(N_1, N_2, N_3)} \tag{5.1}$$

where N_k, $(k = 1, 2, 3)$, is the direction of a projection and p_k is the position of the peak along this direction.

Each detected peak defines a plane perpendicular to the corresponding projection direction (i.e. it defines one unpaired coordinate of the markers). In general, three 1D projections of N points define $3N$ planes which intersect at N^3 points; as a result $(N^3 - N)$ points are fictitious and must be discarded. This can be done by using additional projections, as shown in Figure 5.1.



(a)



(b) (c)

FIGURE 5.1: The algorithm for N=2 markers. $N^3 = 8$ intersection points are computed as candidates (a); by using a fourth projection 4 fictitious points are eliminated (b) and by using a fifth projection (c) only the true points are left.

5.2 Algorithm

The method for localizing N markers consists of four main steps, which are summarized below and further details are provided in the subsequent sections.

1. The process starts with the acquisition of a predefined set of 1D projections, involving excitation of the whole imaging volume. The number and directions of these 1D projections have been optimized, as presented below.

2. Peak detection is performed for each projection; the position of each peak is then determined with sub-pixel resolution (Figure 5.1a) as explained in Chapter 4.

3. Three projections are selected as reference projections, from which N^3 candidate marker positions are calculated (Figure 5.1a). The selection of the reference projections is explained below. The remaining projections are sorted according to the decreasing minimal distance between the peaks they contain. Projections with fewer than N peaks are placed at the bottom of the list and used last. In this way projections that may lose a peak have lower probability of being used and affecting the result. Note that projections with a smaller number of peaks due to merging of the peaks will not eliminate any of the correct points.

4. The fictitious $(N^3 - N)$ candidates are removed by using test projections. For each test projection, the projected value of each candidate point is calculated and the distances between this and the identified peak locations are computed (Figure 5.1(b), Figure 5.1(c)). The candidate point is removed if the minimum computed distance is larger than a tolerance ϵ. If the number of computed points is different from the known number of markers, then the entire solution is discarded.

5.2.1 Choice of the directions of 1D projection

Each computed peak location p_k has an error Δp_k associated with the measurement. The errors Δp_k result in an error ΔP in the computed point P, thus:

$$P = P_0 + \Delta P \tag{5.2}$$

where P_0 is the true position of the marker. It follows from Equation 5.2 that:

$$\Delta P = \frac{\Delta p_1(N2 \times N3) + \Delta p_2(N_3 \times N_1) + \Delta p_3(N_1 \times N_2)}{det(N_1, N_2, N_3)} \tag{5.3}$$

The error ΔP may be minimized by maximizing $det(N_1, N_2, N_3)$. This is achieved by maximizing the minimum angle between any two directions. In other words, the

projection directions should be regularly distributed in space. The direction candidates were taken from the well-known concept of voxel topological neighborhood [Toriwaki and Yoshida, 2009]. This is illustrated in Figure 5.2 for 6-neighbourhood of a voxel, which defines 3 regularly distributed projection lines. Similarly, 18-neighbourhood and 26-neighbourhood define, respectively, 9 and 13 regularly distributed projection lines.

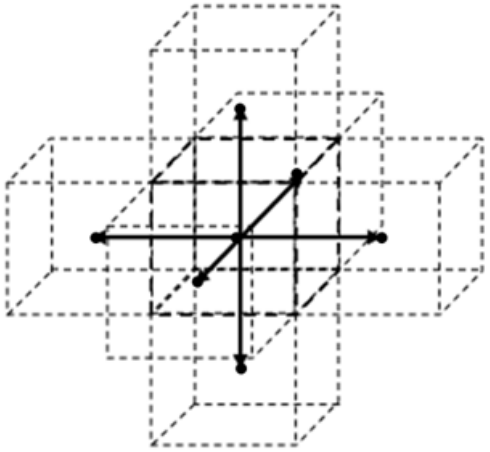


FIGURE 5.2: 6-neighbourhood of a voxel in 3D. A voxel is connected to the 6 surrounding voxels which have a face in common. The vectors connecting the central voxel to the neighbours define three directions.

The number of needed directions is an important issue. The aim was not to modify the tracking sequence during execution as this may compromise the high update rate of the localization method. Simulations were performed in order to test the performance of the algorithm in relation to the number of projections. As a result, 13 projections were acquired and their directions defined in accordance with the 26-neighbourhood. These are the directions that were anticipated in Chapter 4, Section 4.3.

5.2.2 Definition of the reference projections

Following the acquisition, peak detection and peak localization, three *reference projections* need to be selected from the acquired set. For the case of 13 acquired projections there are 13!/(13-3)!3!=286 subsets of three directions N_i, N_j, N_k. The subsets are ordered according to the decreasing value of the determinant $det(N_i, N_j, N_k)$. The first subset with N distinct peaks and a minimum distance between two peaks greater than a prescribed value d is selected as the *reference* subset. The latter condition ensures that the candidate points are well scattered in the volume and therefore that the corresponding computed projected values are well distributed along a projection direction, which

improves the success rate in the subsequent removal of fictitious points. The value of d was set to be higher than the tolerance value ϵ used in removal of fictitious points.

5.2.3 Definition of the tolerance ϵ

If there was no noise and peaks in the reference and test directions were perfectly detected, no tolerance would be needed and the candidate point would be removed if its projection onto a test direction does not coincide with any peak detected in this test direction. However, because there are errors in peak detection, the projections of the candidate points do not coincide with the corresponding detected peaks. In order to solve this issue, a tolerance ϵ is used as follows: the candidate point is removed if the computed distance is larger than a tolerance ϵ or in other words if the projected candidate does not have an identified peak in its vicinity.

Optimizing the value of the tolerance ϵ in removal of fictitious points is an important but complex problem to address. Too small a value for ϵ will remove too many candidate points whereas a too large ϵ will keep some fictitious points in. The experiments, as well as the simulations, indicated that the main factors to be considered when determining the tolerance value are the stochastic nature of the peak position and the issue related to the identification of the peaks that are very close to each other.

The aim was to have less than one in a million unsolved situations. It is well known that for a stochastic variable belonging to Gaussian distribution, the probability that a deviation lies in the range $\mu - 5\sigma$ and $\mu + 5\sigma$ is 0.9999994 [Utts and Heckard, 2006]. As two independent events, namely, projection onto reference directions and projection onto test directions, are used for the removal of fictitious points, the tolerance needs to be 10σ. Taking into account that each candidate point is computed from 3 measurements (1 in each of 3 reference directions) this tolerance value needs to be multiplied by $\sqrt{3}$. As a result, the tolerance value was set equal to $10 \cdot \sigma \cdot \sqrt{3} = 10 \cdot 0.08 \cdot 1.73 = 1.4$ mm.

However, the tolerance may need to be differently defined when the two peaks are close to each other. In Chapter 4, Section 4.3.3, it is shown that peak merging may occur when peaks are within two pixels from one another and that the position of the identified peak is not affected by the merging. In order to accommodate peak merging, the tolerance was automatically enlarged to two pixels size whenever fewer than N peaks are detected. In this way, merged peaks were represented by the identified one. This solution did not affect the accuracy or robustness of the localization method.

It is well known that positional errors may result from resonance offset errors, such as when the markers are in a region of inhomogeneous field near the edges of the imaging volume, or in regions with magnetic distortions caused by differences in magnetic susceptibility. This positional error may affect the accuracy and robustness of the method. The distance between the projected values of candidate points may be further from the

corresponding peaks detected in test projections than the tolerance. If this occurs some of the correct points may be wrongly removed. One way to remedy this problem is to increase the tolerance.

5.3 Performance assessment

5.3.1 Monte Carlo simulations

Monte Carlo simulations were performed in order to establish the required number of projections, assess the accuracy of the 3D localization and estimate the computing time. The simulations involved generation of $N = 3, 4, 5, 6$ random marker positions in 3D, with the only condition that they are at least 30 mm apart, in view of a realistic placement of the markers on a device. The N points were projected onto all directions of a set of 1D projections and a deviation, from a Gaussian distribution, was added to each projected value. These values provided the input for the tracking algorithm which computed the markers' coordinates.

5.3.1.1 Robustness and Accuracy

The robustness of the proposed method was expressed in terms of a percentage of successful localizations of N markers in a set of experiments. Table 5.1 summarizes the results of 10^6 simulations of N points, with $N = 3, 4, 5, 6$. The number of 1D projections was increased from 5 up to 13. These results show that robustness is improved with an increased number of projections and that more projections are needed with an increased number of markers. In all simulated cases the variation in peak localization was Gaussian, with $\sigma_{peak} = 0.08mm$, in accordance with signal peak analysis in Chapter 4.

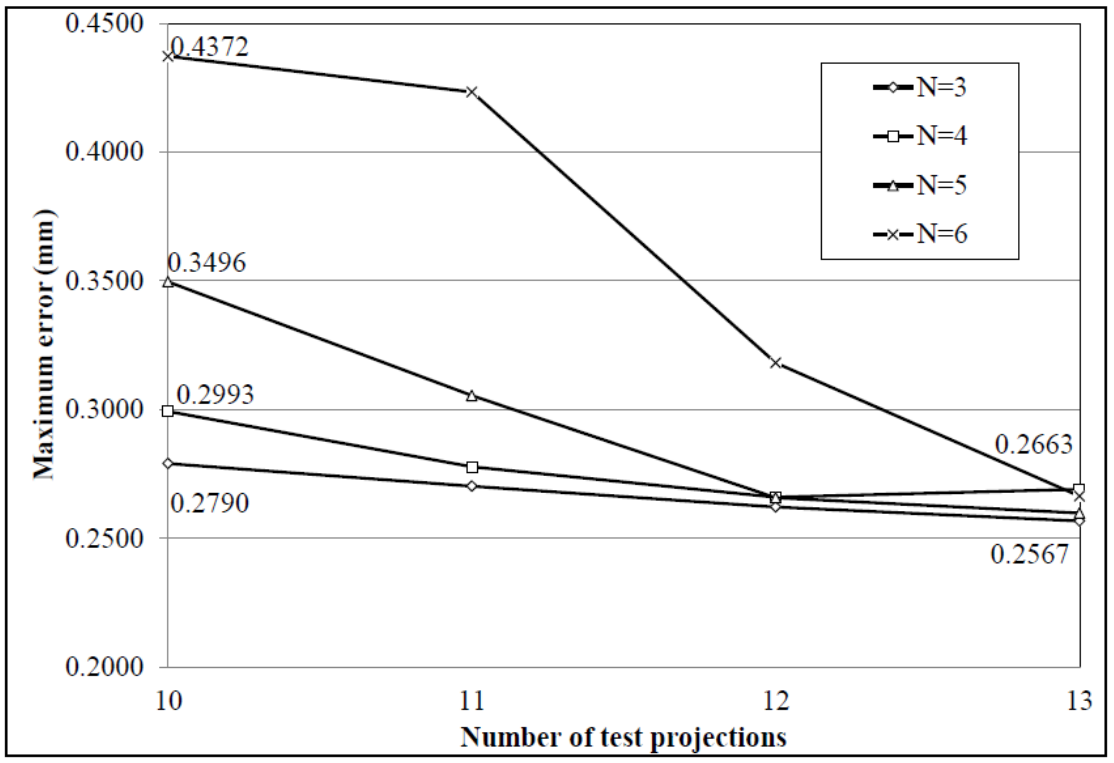
TABLE 5.1: Robustness of the algorithm. Successfully reconstructed points (%).

	5 proj	*7 proj*	*10 proj*	*13 proj*
3 points	95.40	99.99	100.00	100.00
4 points	86.00	99.94	99.998	100.00
5 points	70.00	99.83	99.994	99.999
6 points	51.00	99.40	99.98	99.999

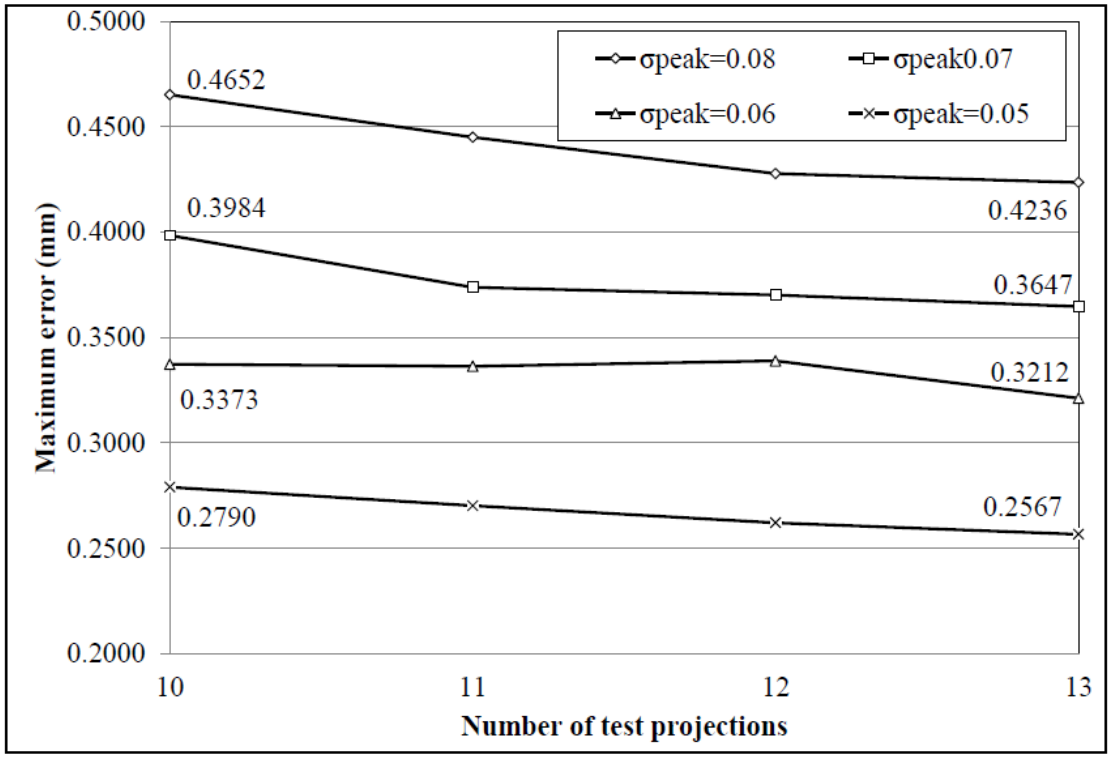
However, the results in Table 5.1 should be considered in relation to the accuracy results in Figure 5.3(a), showing the variation of the maximum error as a function of the number of projections. Two aspects can be observed. First, although the algorithm

robustness may be already high, the maximum error may be significantly reduced by increasing the number of projections and this is particularly evident for $N > 3$ markers. Second, in all cases the results appear to converge at $n = 13$, leading to the conclusion that using 13 projections is an optimal choice.

Figure 5.3(b) shows the dependence of maximum localization error as a function of σ_{peak} and the number of projections, clearly demonstrating the importance of accurate peak localization.



(a)



(b)

FIGURE 5.3: Accuracy of the localization method. (a) Maximum error for $N = 3, 4, 5, 6$. Maximum error(mm) in 10^6 simulations as a function of the number of projections, up to 6 markers,$\sigma_{peak} = 0.05mm$. (b) Maximum error for $N = 3$. Maximum error(mm) in 3D localisation of $N = 3$ markers and increasing σ_{peak}.

5.3.1.2 Computational time

Figure 5.4 shows the measured computational time of the algorithm implemented in MatLab, running on a Windows PC (i7 processor, 2.13 GHz, 64-bit) as a function of the number of markers N and the number of projections, showing that computation for 6 markers using full 13 projections is achieved in less than 2.5 ms. The increase in time with the number of projections is insignificant.

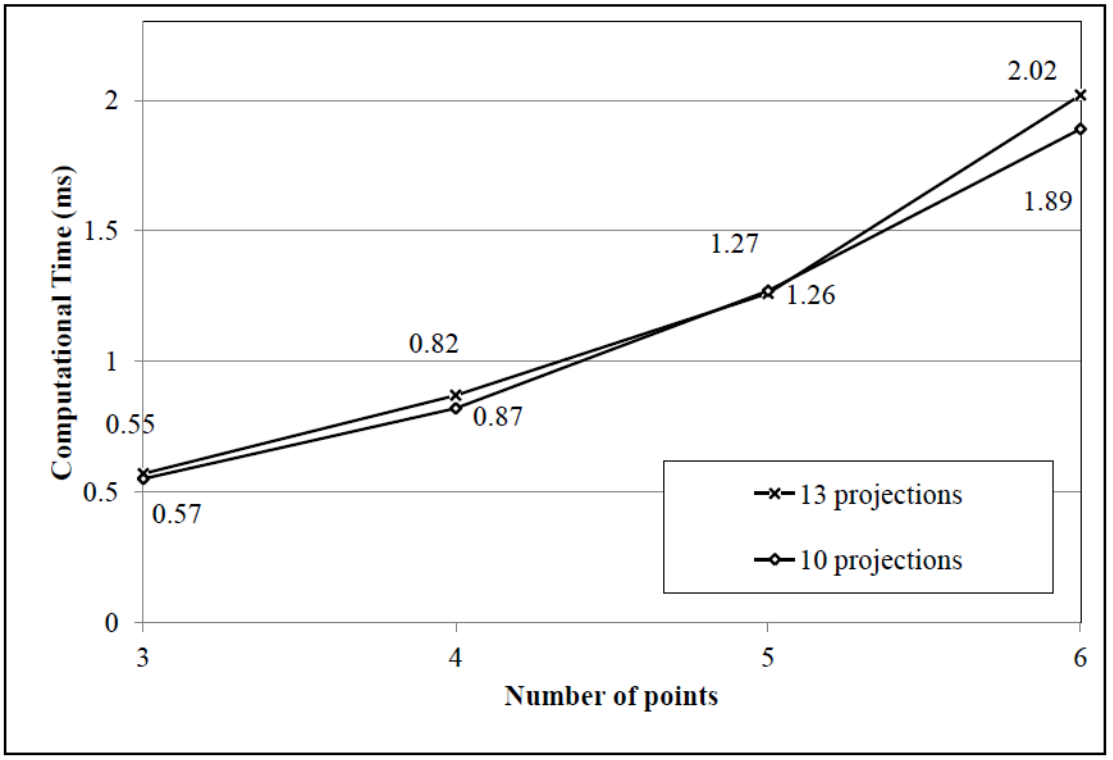
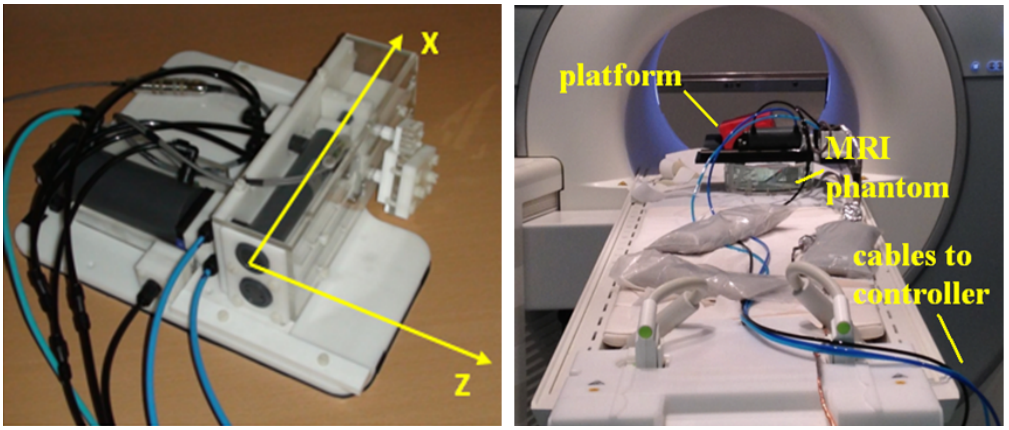


FIGURE 5.4: Computational time. The graph shows the computational time for N=3, 4, 5, 6 when 10 and 13 projections are used.

5.3.2 Experimental accuracy assessment

The accuracy of the tracking method was assessed in a 2.9 T MR scanner under static and dynamic conditions. To this end a 2 degree-of-freedom, pneumatic, remotely controlled, MR-compatible platform was employed. The platform was developed within the research group and it is shown in Figure 5.5(a). Position measurements were provided by built-in incremental, linear optical encoders with verified accuracy 0.025 mm.



(a) (b)

FIGURE 5.5: MRI-compatible two degree of freedom platform.(a) Platform and (b) Set up in the MR scanner. The two translational movements are actuated pneumatically and controlled by a microcontroller and piezo-valves situated outside the magnet room.

A marker was fixed on the moving arm of the platform, which in turn was placed on top of a 1L water flat phantom, as shown in Figure 5.5(b). The platform axes were aligned with the scanner axes and the marker was placed at the isocentre by means of the laser crosshair of the scanner. Translations were performed in 10 mm steps along the x and z axes in the range $\pm 40mm$. The position was measured by the platform's optical encoders and recorded at each step, while the marker was scanned 20 times and each position was calculated by the proposed algorithm.

First, standard and maximum deviations of the computed positions from their corresponding means were calculated. This gave an initial estimation of the position accuracy of the tracking method. Then, the error in localization of the marker was calculated as the difference between the distances computed using the marker tracking and those measured using the optical encoders.

The use of the actuated platform also allowed the assessment of the dynamic tracking accuracy. Dynamic tests involved moving a marker along predefined trajectories in the x and z directions at various speeds, while simultaneously recording both the encoder positions and the measured marker positions.

5.3.2.1 Static tests

Table 5.2 shows an analysis of the positional error computed by applying the algorithm to the 20 sets of 1D projections of a marker at different locations within the scanner. Standard deviation was computed for each coordinate as well as for the 3D distance from each point to the mean point. The standard deviation is lower than 0.06 mm and the maximum error is smaller than 0.21 mm for all three coordinates.

TABLE 5.2: Positional error.

	x	y	z	$3D$
Standard deviation (mm)	0.024	0.040	0.058	0.037
Maximum error (mm)	0.105	0.090	0.148	0.208

Figure 5.6 shows a representative subset of the distance errors. These were computed as the difference between translation distances calculated using marker tracking and those measured using optical encoders. Error contribution due to an imperfect alignment of the platform with the scanner axes was assumed to be negligible. The corresponding statistics for independent translations in the x and z directions are presented in Table 5.3. The average translational error was 0.056 mm while the maximum error was smaller than 0.3 mm. These experiments indicate that sub-millimeter accuracy in tracking can be achieved using the proposed method.

It can also be observed that the standard deviation of the distance error is larger than that of the positional error shown in Table 5.2. This is in agreement with the theory which states that, for independent random variables x and y the variance of their sum or of their difference is the sum of individual variances, i.e. $\sigma^2_{(x+y)} = \sigma^2_{(x-y)} = \sigma^2_x + \sigma^2_y$ [Utts and Heckard, 2006].

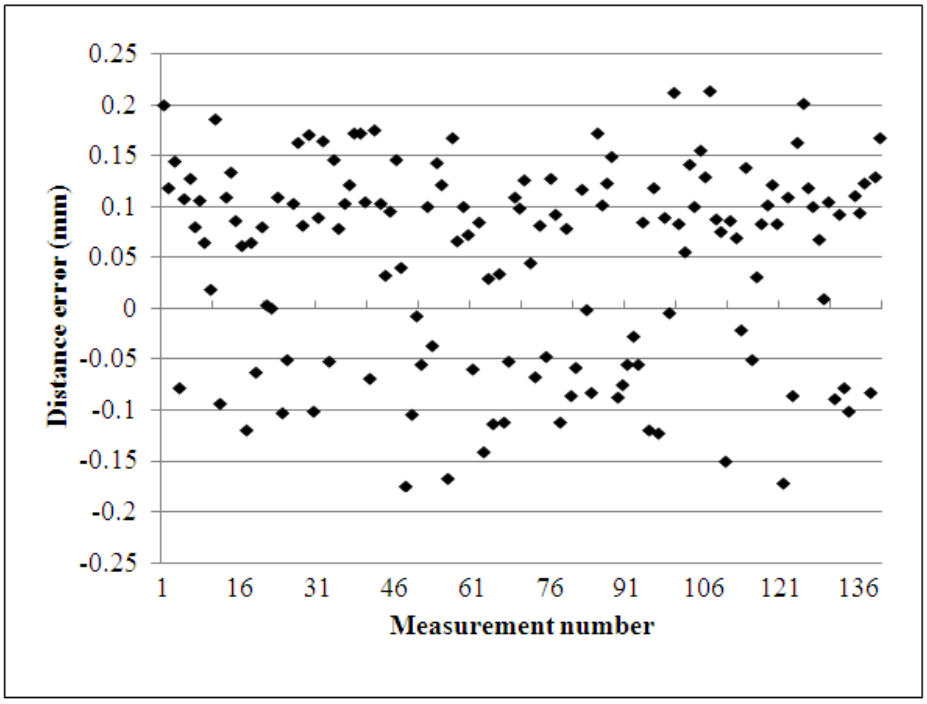


FIGURE 5.6: Distance error for a subset of 140 measurements along x. Each point is computed as the difference between the steps in x calculated with marker tracking and those measured with optical encoders.

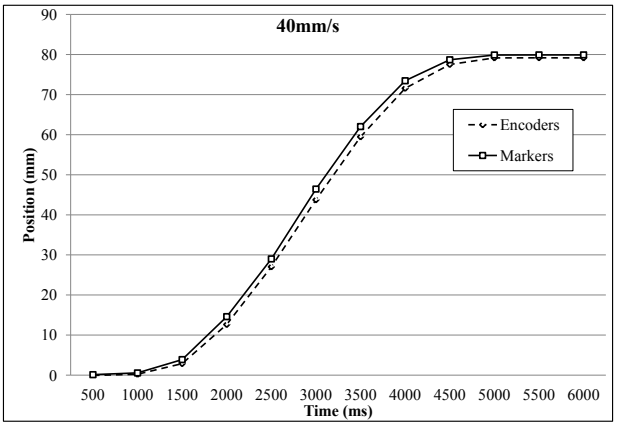
TABLE 5.3: Distance error statistic: mean error, standard deviation and maximum error. The analysis was performed along x and z directions.

	x translation (mm)	*z translation (mm)*
Mean error (mm)	0.049	-0.063
Standard Deviation (mm)	0.098	0.168
Maximum error (mm)	0.216	0.283

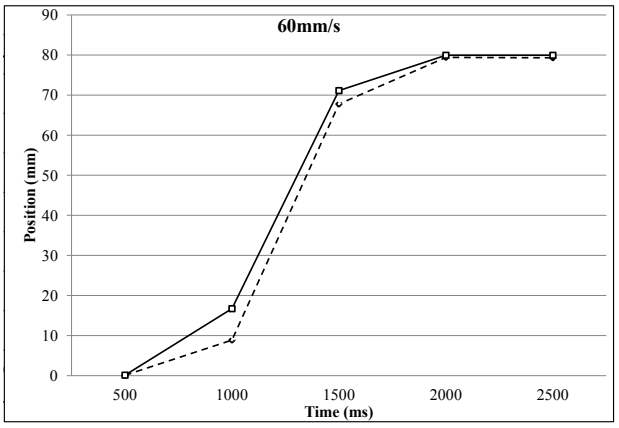
5.3.2.2 Dynamic tests

Figure 5.7 shows the results of dynamic tests, involving controlled movement of the platform carrying the marker at different speeds. While the platform was moving, sets of 13 1D projections were repeatedly acquired at regular intervals of 500 ms. The instantaneous position was measured by the encoders after the acquisition of the $6^{th} projection$, in order to reduce the time delay between the locations obtained in the two ways.

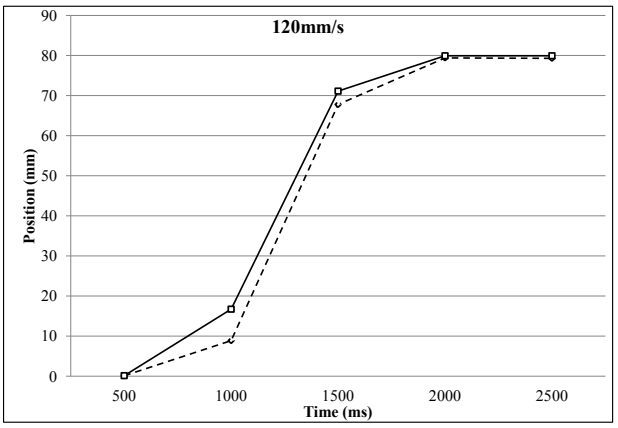
Table 5.4 shows the mean and maximum error at the different speeds of the platform. The reported speed is the maximum speed achieved using the s-shaped velocity profile and was controlled by the platform controller. At 40 mm/s the error is lower than 1 mm; at higher speeds, the error increases up to a few mm. This increase in error was attributed to the movement of the marker during acquisition of a set of 1D projections.



(a)



(b)



(c)

FIGURE 5.7: Dynamic tracking at different speeds. The plots show the position of a marker measured by the encoders and computed by the proposed method.

TABLE 5.4: Distance error for increasing speed.

	40mm/s	*60mm/s*	*120mm/s*
Mean error (mm)	0.39	1.17	3.07
Maximum error (mm)	0.72	3.65	7.81

5.4 Comparison with previously proposed methods

The performance of the proposed localization method was compared in terms of accuracy and time with the previously reported method by Flask et al. [2001]. In order to compare adequately the two methods, Flask et al. [2001] method was implemented in MatLab and run on the same computer as the proposed one.

It can be seen in Table 5.5 that the proposed method achieves a comparable standard deviation but a smaller maximum error. This can be attributed to the fact that the algorithm presented in Flask et al. [2001] uses clustering and averages all valid projections to calculate the result, while the proposed one uses only those projections that were found to be optimal. Importantly, avoiding cluster analysis dramatically reduces the computational time of the algorithm. This was particularly evident when 6 markers were tracked, in which case a reduction of 100 ms was obtained, as shown in Figure 5.8.

In addition, by acquiring a pre-defined set of optimal 1D projections, the acquisition time was drastically reduced and thereby the total updating time, as reported in Table 5.5. Furthermore, the proposed method eliminates the problem inherent in Flask et al. [2001] algorithm, which occurs when two markers have similar coordinates along the common axis of the two orthogonal scans.

TABLE 5.5: Comparison between Flask et al. [2001] and the proposed method, for $N = 3$ markers. Statistics for 10^6 simulations.

	StDev(mm)	*MaxError(mm)*	*Comp. Time(ms)*	*Update Time(ms)*
Flask et al. [2001]	0.048	0.342	16	200
Proposed method	0.054	0.279	0.9	73.71

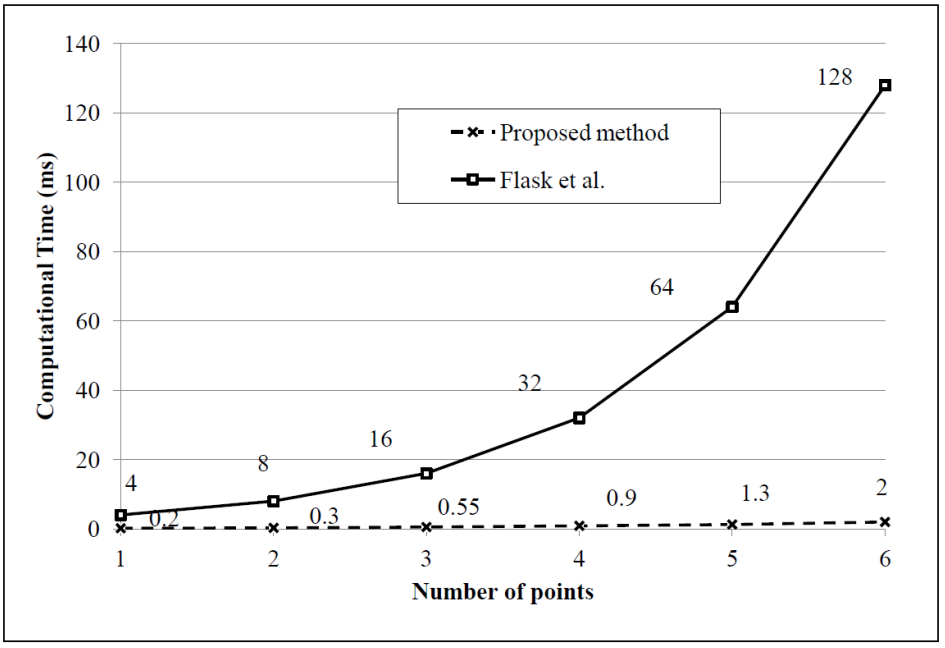


FIGURE 5.8: Computational time. Comparison between the proposed algorithm and the one presented in Flask et al. [2001].

5.5 Discussion and conclusions

This Chapter presented the algorithm developed for localization of N markers in 3D from a set of 1D projections. The complexity of the post processing algorithm was significantly reduced by avoiding cluster analysis [Flask et al., 2001], while higher accuracy was achieved by applying Gaussian interpolation in peak detection and using an optimal set of projections to compute the points. The algorithm does not reject projections with coincident peaks, which results in a reduced scan time, while the number of projections may be traded against robustness and accuracy for optimized results in a specific situation.

By using more than three markers, higher accuracy in localizing an instrument can be achieved with no compromise in update rate. Computational time of up to 6 markers required less than 2 ms. An update rate of 10 Hz was achieved with localization error lower than 0.3 mm. The reliability of the method in dynamic situations, when the markers are moving, was demonstrated and resulted in a maximum error equal to 0.7 mm for speeds anticipated during interventional procedures.

5.5.1 Failure scenarios

In the course of this work it was found that the proposed localization method may fail in two situations:

- a peak was detected which does not correspond to any of the markers;
- a peak from some marker was not detected (which is a different situation than peak merging).

The first situation was solved by introducing a threshold in the detection of the peaks and by checking the level of signal gainst the background for each of the detected peaks. The likelihood of occurrence of the second situation and its impact were minimized as follows:

- The projections used for removal of fictitious points are ordered in such a way that projections having less than N peaks are used last. In this way projections that may lose a peak have lower probability of being used and affecting the result. Note that projections with a smaller number of peaks due to merging of the peaks will not eliminate any of the correct points.
- If the number of computed points is different from the known number of markers, then the entire solution is discarded.

Chapter 6

Tracking in MRI-guided transrectal prostate biopsy

The proposed localization method was employed for tracking the endorectal probe which serves as guide for the biopsy needle in the MRI-guided prostate biopsy procedure. With this scope, three RF semiactive markers were embedded within the probe in a known geometrical configuration. At each location update, the measured markers were assigned to the nominal markers in a probe model. Then, Least-Squares method was employed in order to best-fit the probe model to the measured one. The obtained transformation matrix was subsequently used to compute the biopsy needle direction and needle tip in the MR scanner frame.

This Chapter begins describing the overall MRI-guided prostate biopsy system and its components. Tracking of the endorectal biopsy probe using the proposed method is then explained. Accuracy in computing the needle tip is then assessed through Monte Carlo simulations and experiments in the MR scanner. Finally, accuracy of the needle tip location using more than three markers is explored.

6.1 System layout

Figure 6.1 shows the prostate biopsy system integrated with the MRI environment. The system includes an MR-compatible prostate biopsy manipulator for positioning the biopsy needle guide, a navigation workstation which hosts the tracking and visualization software, and a shielded monitor for image-based guidance of the probe.

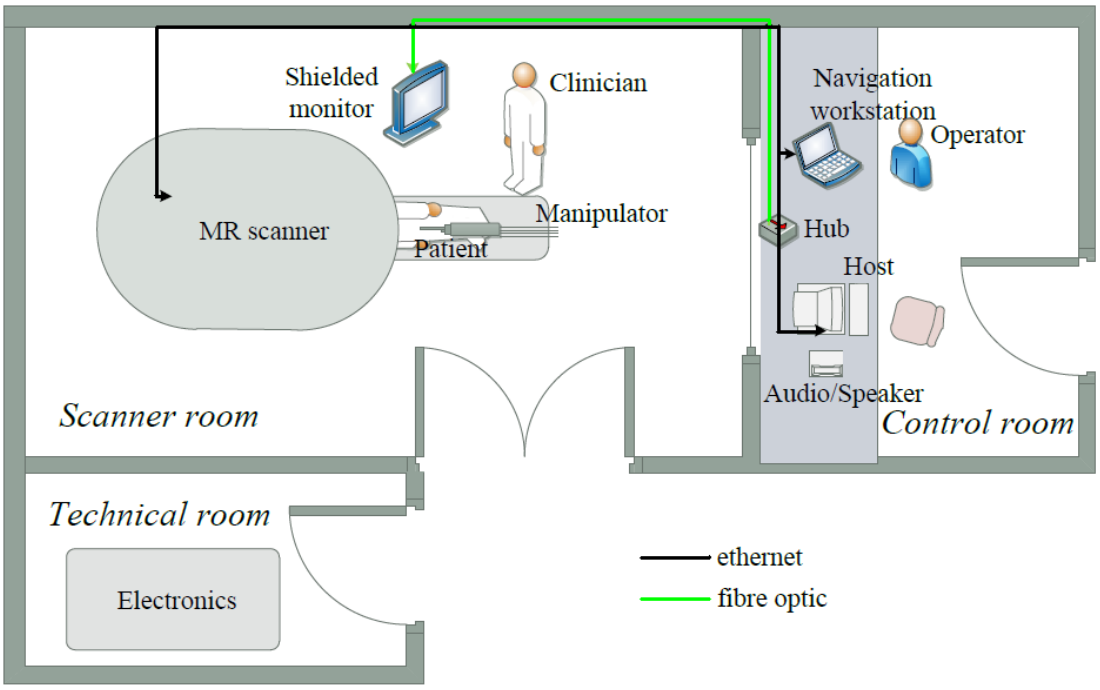
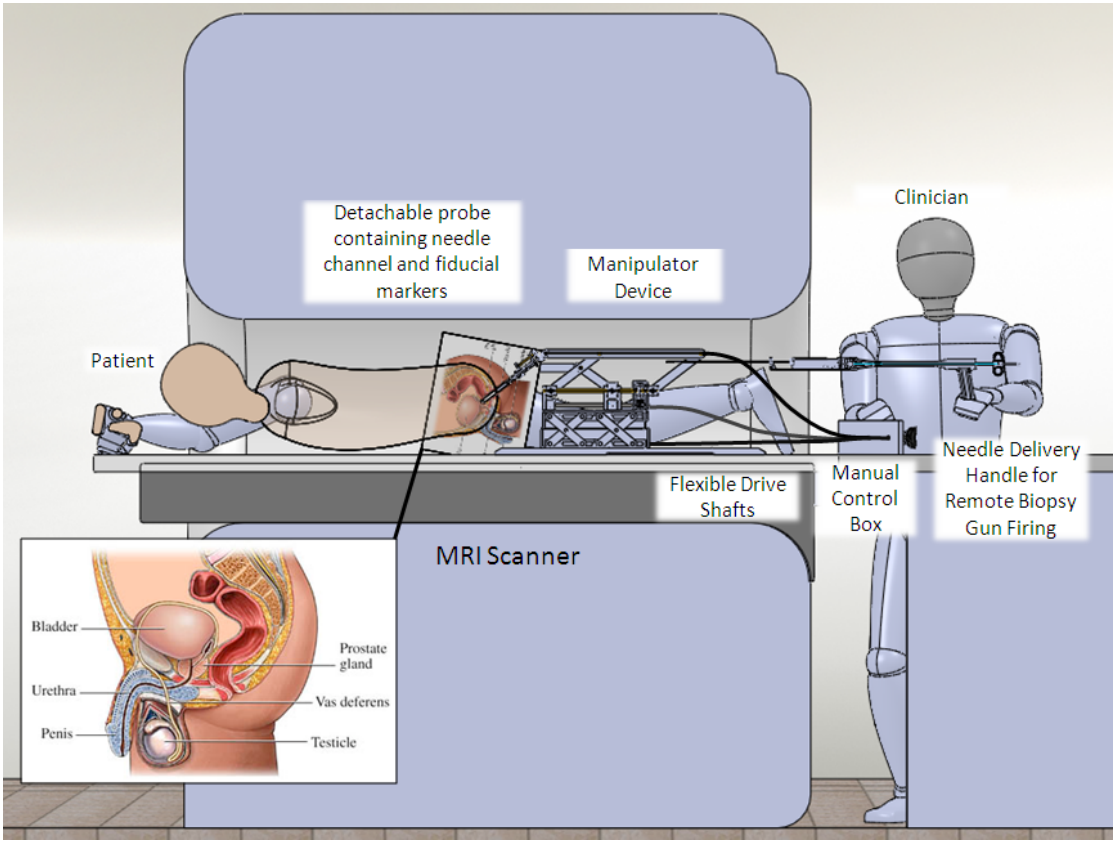


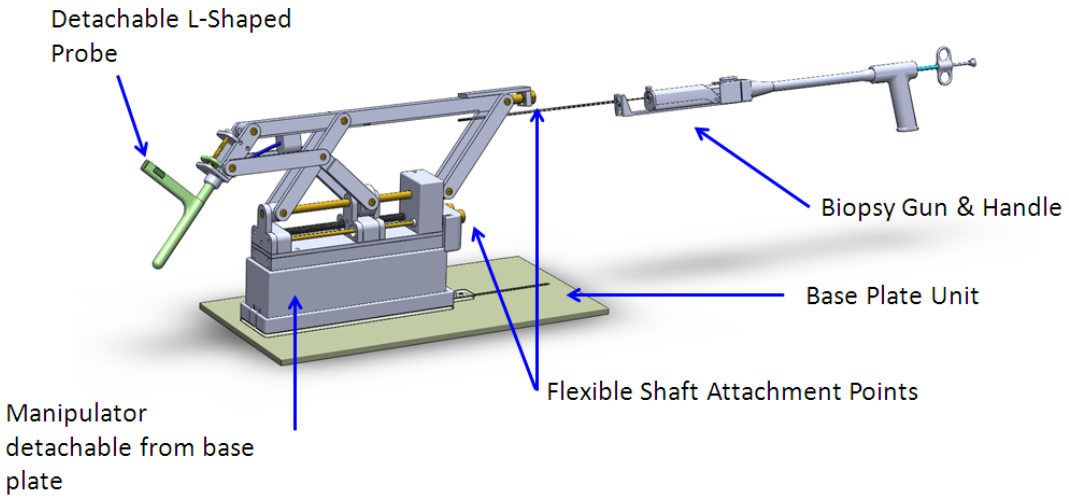
FIGURE 6.1: The main hardware components of the MRI-guided prostate biopsy system are represented.

6.1.1 Manipulator design

An MRI-compatible manipulator was developed within the project to position the endorectal biopsy probe [Lambert et al., 2012]. The manipulator, shown in Figure 6.2, was designed for a conventional high field closed-bore scanner and for a patient in the prone position. The constrained access to the patient within the magnet bore was addressed by using remote actuation, involving mechanical transmission via phosphor-bronze flexible shafts. High rigidity and stability of the manipulator were achieved by employing a detachable base plate to be positioned in between the legs of the patient. In order to maintain material compatibility with MRI, the manipulator was manufactured entirely from plastic, except from the bronze shafts; however, these were situated sufficiently far away from the imaging volume and did not produce any visible artifact.



(a)



(b)

FIGURE 6.2: MRI-compatible manipulator for transrectal prostate biopsy. The manipulator is used to position an endorectal probe which serves as guide for the biopsy needle. The procedure is performed inside a closed-bore MR scanner and with the patient in the prone position.

The kinematics of the manipulator was designed to fulfill two requirements. The first was to maintain the fiducial markers perpendicular to the main field at any pose of the

probe, maximizing the peak amplitudes during tracking. The second was to enable the required range of probe movements.

In order to establish the required range of movements during the procedure an experimental investigation involving a conventional ultrasound probe was performed on volunteer patients. A six degree of freedom 3D digitiser (MicroScribe) was employed as the measuring device. Suitable end-effector adapters were designed and made in order to attach the standard ultrasound transrectal probe to the digitiser. This provided a position measuring system for the transrectal probe that was suitable for use during the standard procedure. The equipment was installed in the interventional facility at Royal Marsden hospital (Sutton, London, UK). The experimental trials involved a total of 4 volunteer patients undergoing the prostate biopsy procedure. In each case a PC computer was used to provide continuous monitoring of the probe position and orientation with a conveniently high sampling rate, recording thousands of readings. The data generated in this way was subsequently analysed in 3D using MatLab. The analysis indicated that the probe rotates in the coronal plane and about the y axis by an angle in the range $\pm 25^{\circ}$, and in the sagittal plane and about the x axis by an angle in the range $30^{\circ} - 80^{\circ}$. This led to the design of a manipulator which supports two rotational (pitch, jaw) and one translational (insertion) degrees of freedom.

The manipulator mechanism is shown in Figure 6.3. The three degrees of freedom are supported by a remote-centre-of-motion parallelogram mechanism. The remote-centre was designed to be positioned at the anus in order to minimize tissue deformation and maximize patient comfort. Importantly, the mechanism is such that the fiducial markers are kept perpendicular to the main field at any pose of the probe.

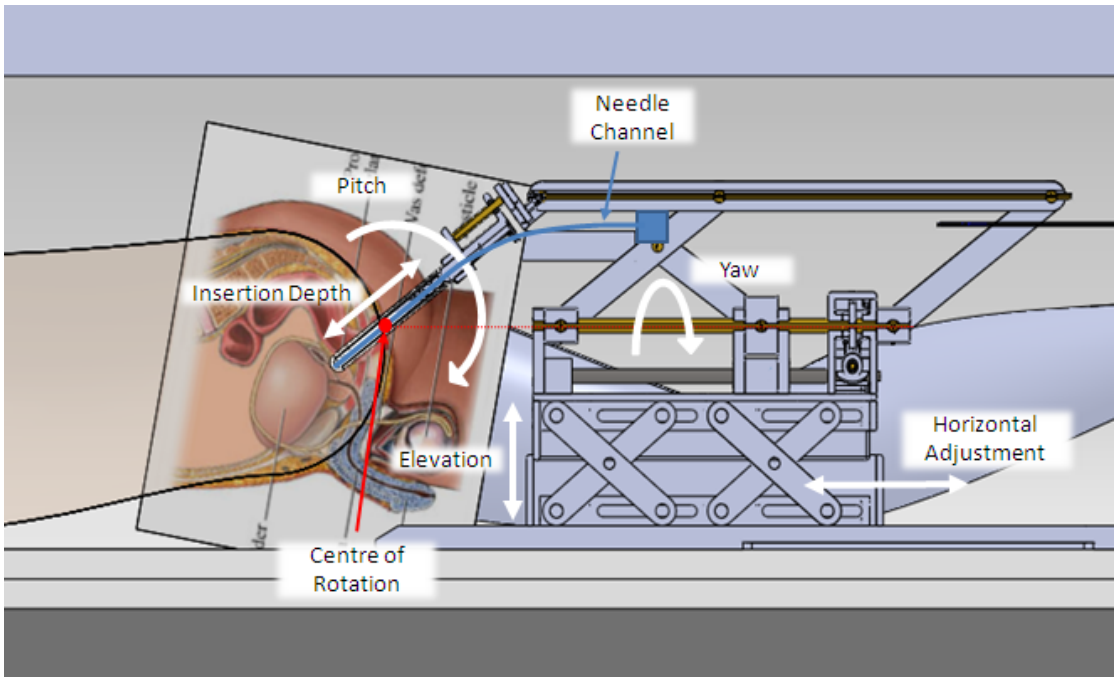


FIGURE 6.3: Manipulator mechanism. The parallelogram mechanism supports two rotational and one translational degrees of freedom and maintains the markers perpendicular to the main field at any pose of the probe.

6.1.2 Endorectal biopsy probe

Figure 6.4 shows the design of the endorectal biopsy probe. The probe is detachable from the manipulator by means of a locking mechanism. This allows for initial insertion and positioning of the probe into the rectum so that the remote-centre can be easily aligned with the anus of the patient.

The proposed localization method was employed to compute position and orientation of the probe within the MR scanner frame. Figure 6.4 shows the geometrical configuration of the three markers which were incorporated within the probe. In order to maximize the accuracy of the needle tip location, one of the markers was positioned as close to the probe tip as possible and all markers were placed reasonably far apart [Shamir et al., 2012]. Localization of the probe using the measured markers coordinates is explained in Section 6.2.

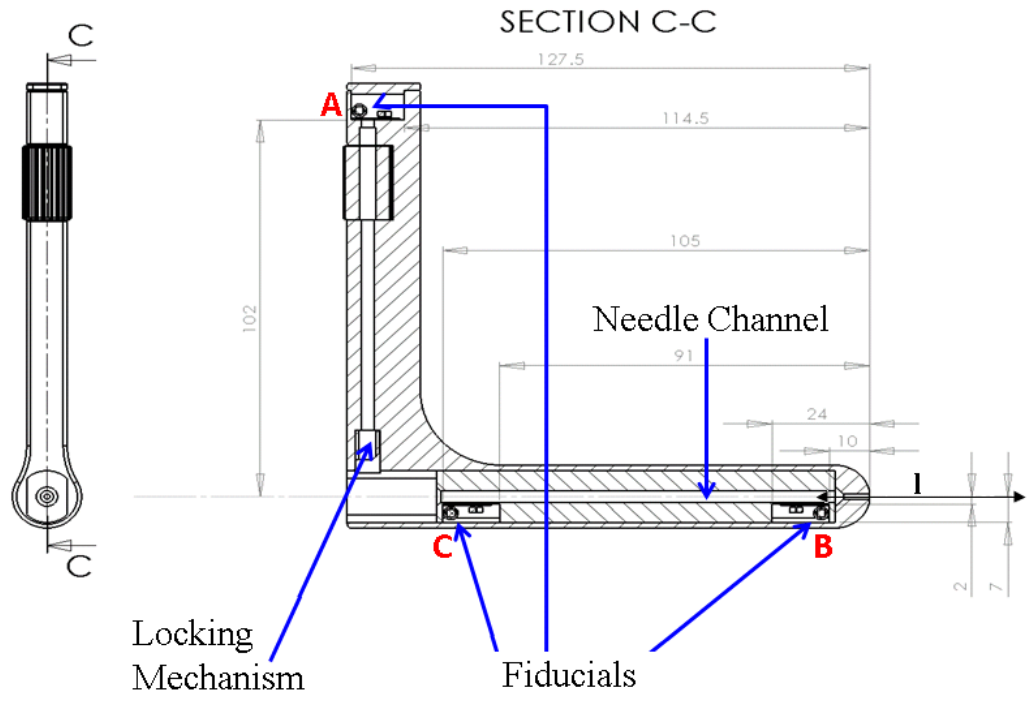


FIGURE 6.4: Endorectal biopsy probe. a) Configuration of three markers within the probe. The markers positions are labelled as A, B, and C. The needle channel is parallel to the segment CB and coaxial with the probe. l is the needle length after firing. The probe diameter is about 16 mm.

6.1.3 Biopsy needle

A limitation common to numerous systems previously proposed is that the patient has to be withdrawn from the scanner to perform the biopsy. This means a cumbersome procedure which takes time and limits the accuracy of the MR guidance. The main cause of this limitation is the use of rigid biopsy needles having a handle containing the firing mechanism. This does not allow biopsies to be performed inside the limited space of conventional close-bore MR scanners.

To solve this problem, an MR-compatible flexible needle was employed, which can be bent to avoid interference with the inner wall of the magnet. The needle was supplied by InVivo Germany GmbH, Schwerin, Germany. This was a longer version of a standard biopsy needle, such that it can be used with the manipulator and the patient remaining in the scanner. An elongated handle for insertion of the biopsy gun into the manipulator was designed. The needle delivery mechanism allows for the needle to be advanced into the tissue prior to firing. This initial puncture prevents unwanted tissue deformation and needle deflection to give better accuracy. Experiments showed that the spring-loaded

mechanism can achieve a sufficient firing speed for the bending radii anticipated in the procedure.

6.1.4 Navigation workstation

The tracking and visualization software were implemented on an external PC (navigation workstation). The complete software was written in MatLab and was tested on both Windows and Linux platforms. The navigation workstation was located in the control room and connected to the MR scanner via a local Ethernet network in order to receive MR images and 1D projections. Visual feedback was provided to the clinician in the scanner room by connecting the navigation workstation to a shielded monitor situated in the scanner room, via VGA interface. The clinician in the scanner room and the workstation operator (radiographer) in the control room communicated via microphones and speakers.

The functionalities of the navigation software may be summarized as follows:

- 3D visualization of the acquired MR images;
- Real-time acquisition of the 1D projections and computation of the RF markers' coordinates;
- Localization and visualization of the instrument within the imaging volume;
- Target selection;
- Tracking of the instrument to the selected target;
- Suggestion for optimal movements.

In order to send MR images from the MR scanner to the navigation workstation, the image-sending functionality of the MR scanner was switched on by using the Siemens *ideacmdtool* on the host computer. The *ideacmdtool* provides means for setting hostname, port and drive, while the directory of destination was mapped via the Map Network Driver tool. User Datagram Protocol (UDP) connection was used in the navigation workstation in order to receive 1D projections in real-time from the MR scanner.

6.1.5 Intervention Workflow

The workflow of the intervention, which is the result of extensive consultations with clinicians, may be outlined as follows:

1. The patient is positioned on the table in the prone position and the endorectal probe is introduced into the rectum. The remote-centre is aligned with the anus. In

order to minimize positional errors introduced by field inhomogeneity, the isocentre is set as close to the prostate as possible.

2. The manipulator is attached to the probe and then secured to the table of the scanner with an adjustable support, to accommodate the patient.

3. The scanner table is moved into the magnet. Images of the anatomy are acquired using T_2-weighted Turbo Spin Echo Sequence and sent to the navigation workstation.

4. The navigation software determines the position of the remote centre of motion of the mechanism in scanner coordinates, for subsequent use by the graphical user interface.

5. Using the graphical user interface, the clinician interactively selects the lesion to be targeted. The navigation program computes and displays the ideal location of the probe and needle to carry out the biopsy.

6. In this step the targeting starts. In a streaming mode, the scanner sends the IFT data (1D projections) to the navigation workstation while the clinician remotely controls the manipulator. Calculation of the probe location is performed in real-time and visualized as overlay on the MR images.

7. When sufficiently accurate targeting is achieved, confirmation images are acquired to verify if the target has moved. In the case the target has moved the procedure is repeated starting from Step 5. Otherwise, the biopsy needle is released and the procedure continues with Step 8.

8. After the sample is collected additional confirmation images are acquired and the table is moved out of the magnet, the endorectal probe is detached from the manipulator and removed from the patient, and the patient is unsecured from the table.

6.2 Tracking of the endorectal probe

6.2.1 Paired-point assignment

Paired-point assignment is a method in which measured markers in the MR scanner frame are assigned *or* matched to corresponding markers in the probe model. The assignment was done using the fact that by design the distances between markers are different from one another and they are known. The solution of Zhang et al. [2001] was extended so that it is not necessary that all markers are collinear.

Prior to assignment, the markers in the probe model (nominal probe) are labelled as follows. The distances between pairs of markers are computed and sorted in ascending order. The marker that is common to the two largest distances is annotated as marker A, while the other one on the largest distance is annotated as marker B. The third marker is annotated as C. The labelling of the markers in the probe model is shown in Figure 6.4.

The first step in the assignment is to check if the number of measured markers is different than the number of nominal markers. If this is the case the assignment is not possible and the point set is discarded and another one acquired instead. The next step is to calculate the distances between the measured markers. These distances are compared against the known distances between nominal markers and if there is significant discrepancy the point set is discarded. The final step is to assign the measured markers to the nominal markers in the probe model using the same labelling method as described above. The key requirement in assigning computed points to corresponding nominal markers is that the distances between the markers are different, fixed and known.

6.2.2 Alignment using Least-Squares method

Once correspondences between measured markers and nominal markers are known, the known geometry of the probe can be used to compute any vector or point defined within the probe model in the MR scanner frame. In order to minimize the error introduced by the measurement, Least-Squares method was employed [Bjorck, 1996] .

Least-Squares method computes the optimal rigid transformation matrix that aligns the nominal markers $\mathbf{M}$ in the probe model to the measured markers $\mathbf{P}$ in the MR scanner frame. This transformation matrix, which includes *rotation* and *translation*, minimizes the sum of the squared distances between nominal markers $\mathbf{M}$ and corresponding measured markers $\mathbf{P}$ [Arun et al., 1987][Bjorck, 1996]:

$$\sum_{i=1}^{N} \|P_i - (\mathbf{R} \times M_i + \mathbf{T})\|^2 \tag{6.1}$$

where N is the number of markers; $\mathbf{R}$ and $\mathbf{T}$ are 3×3 rotation and translation matrix, respectively.

Similarly to Arun et al. [1987], a solution to the Least-Squares problem which uses Singular Value Decomposition (SVD) [Bjorck, 1996] was adopted. The steps of the solution may be described as follows.

1. The centres of mass C_P and C_M of the measured points $\mathbf{P}$ and nominal markers $\mathbf{M}$ sets are calculated as average points:

$$C_P = \frac{1}{N}\sum_{i=1}^{N} P_i \tag{6.2}$$

$$C_M = \frac{1}{N}\sum_{i=1}^{N} M_i \tag{6.3}$$

, with N number of markers.

2. The two point sets are translated so that both centroids are at the origin, by computing $\mathbf{M}^{'} = \mathbf{M} - C_M$ and $\mathbf{P}^{'} = \mathbf{P} - C_P$. This operation removes the translation component and leaves the rotation only.

3. The matrix $\mathbf{H}$ is computed as:

$$\mathbf{H} = \sum_{i=1}^{N} \mathbf{M}_i^{'}\mathbf{P}_i^{'t} \tag{6.4}$$

, with t denoting the matrix transposition.

4. The SVD of matrix $\mathbf{H}$ is calculated as:

$$\mathbf{H} = \mathbf{USV^t} \tag{6.5}$$

, with $\mathbf{U}$ orthogonal matrix, $\mathbf{S}$ diagonal matrix, and $\mathbf{V}$ transpose of an orthogonal matrix.

5. The rotation matrix $\mathbf{R}$ is computed as:

$$\mathbf{R} = \mathbf{VU}^t \tag{6.6}$$

6. The translation matrix $\mathbf{T}$ is computed as:

$$\mathbf{T} = -\mathbf{R} \times C_M + C_P \tag{6.7}$$

The computed transformation can then be applied to any other vector or point defined within the probe model to compute its location in the MR scanner frame while minimizing the error introduced by the measurement. The needle tip in the scanner frame is found by applying this transformation to the nominal tip of the needle given by the design of the probe.

6.3 Targeting accuracy

Monte Carlo simulations were performed in order to assess the accuracy of the measured needle position after firing. Using the model of the probe shown in Figure 6.4, 10^5 random orientations of the probe were tested. Each orientation was achieved by two rotations of the markers in the probe. First rotation was in the sagittal plane around the x axis for a random angle α, with $30° < \alpha < 80°$, and second rotation was in the coronal plane around the y axis for a random angle β, with $-25 < \beta < +25°$. The corresponding rotation matrices were, respectively, as follows [Rogers and Adams, 1989]:

$$R_x = \begin{pmatrix} 1 & 0 & 0 \\ 0 & cos(\alpha) & -sin(\alpha) \\ 0 & sin(\alpha) & cos(\alpha) \end{pmatrix}$$

and

$$R_y = \begin{pmatrix} cos(\beta) & 0 & sin(\beta) \\ 0 & 1 & 0 \\ -sin(\beta) & 0 & cos(\beta) \end{pmatrix}$$

For each pose, the nominal position of the needle tip was computed from the positions of the rotated markers using the known geometry of the probe. The measured position of the needle tip was simulated as follows:

1. The projections of the rotated markers onto all 13 directions were computed (these projections correspond to the positions of the signal peaks in a real experiment).

2. A random number from the Gaussian distribution was added to each projection value in order to simulate the stochastic nature of the peak position.

3. The proposed localization method was applied to the projections and measured positions of the markers were estimated.

4. These estimated markers were assigned to the corresponding markers in the nominal model of the probe.

5. The transformation matrix that aligns markers of the nominal probe to the estimated markers was computed using Least-Squares method.

6. The same transformation matrix was applied to the nominal tip position in order to obtain the estimated needle tip position. The same result would be obtained if the transformation matrix was applied to the nominal markers and the needle tip position was computed from the transformed nominal markers using the known geometrical relation between markers and needle tip.

The targeting error was computed as the Euclidean distance from the computed needle tip to the nominal needle tip. As a result, for a standard deviation in the Gaussian distribution equal to 0.08 mm, the mean error in determining the needle tip position was 0.214 mm, the standard deviation was 0.111 mm, and the maximum error was 0.880 mm.

Experiments in the MR scanner were also performed to estimate the targeting accuracy. A fourth marker was placed at the tip of the probe; the probe was attached at the manipulator which was, in turn, placed in a 2.9 T Siemens Verio MR Scanner. Four 2L water phantoms were positioned around the probe. The nominal coordinates of markers and needle tip were calculated as the average of 20 repeated measurements with the probe in a static initial position.

The probe was rotated and translated so that 20 different poses were achieved. For each pose, 1D projections were acquired and the coordinates of the four markers were computed by applying the proposed localization method. For the three nominal markers within the probe, assignment and alignment with the measured markers were performed; the calculated transformation matrix was applied to the nominal fourth marker (nominal needle tip). Targeting error was calculated as the difference between the nominal needle tip and the measured fourth marker. The mean error in determining the needle tip position was 0.734 mm, the standard deviation was 0.460 mm, and the maximum targeting error was 1.11 mm.

6.3.1 Expected targeting accuracy using more than three markers

Further improvement to the accuracy in localizing the tip of the needle may be achieved by using more than three markers. The dependence of the targeting accuracy on the number of employed markers was quantified by implementing Monte Carlo simulations for more than three markers. A maximum number of 6 markers was considered, as it was recognized that this is a realistic number of markers which can be embedded within a probe.

The markers configuration of Figure 6.4 was the starting configuration. Markers were added one by one to this configuration. As shown in Figure 6.5, a fourth marker D, a fifth marker E, and lastly a sixth marker F were added in that order. For each added marker Monte Carlo simulations were performed as above and the targeting error was computed.

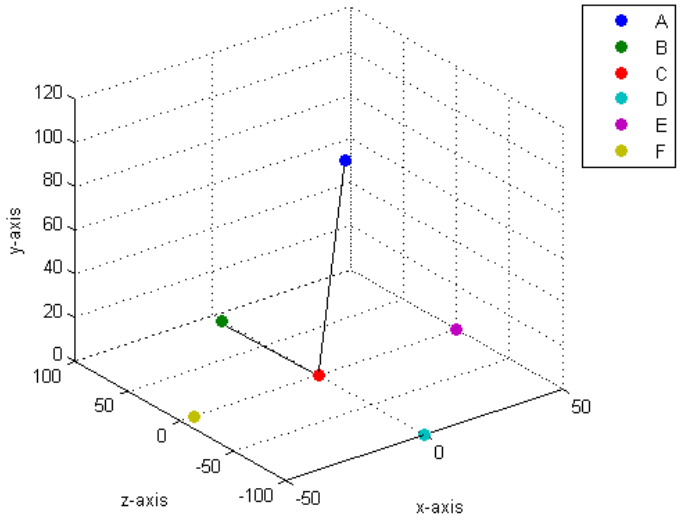


FIGURE 6.5: Configuration of N= 6 markers. Marker A, B, and C were the starting configuration; markers D, E, and F were added one by one and new targeting accuracies were computed.

10^5 Monte Carlo simulations were performed per for each configuration of 3, 4, 5, and 6 markers, respectively. The simulations were performed for two lengths l of the needle, one equal to 60 mm and the other was equal to 120 mm. 60 mm is the maximum firing distance for the employed biopsy needle, while 120 mm represents a situation in which the markers are further away from the needle tip e.g. for space limitation or safety reasons. Results are showns in Tables 6.1 and 6.2.

It can be noticed that, in general, the maximum error in locating the needle tip can be reduced by using more markers. For a needle length of 60 mm, with 6 markers the maximum error decreases from 0.88 mm to a value equal to 0.53 mm. For a needle length of 120 mm, the targeting error significantly increases when three or four markers are employed, while using 6 markers the targeting error shows only a relatively modest increase above the 60 mm case.

TABLE 6.1: Targeting accuracy using up to 6 markers. Length of the needle equal to 60 mm. Standard deviation equal to 0.08 mm.

Markers	St Dev(mm)	Mean Error(mm)	Max Error(mm)
3	0.111	0.214	0.88
4	0.097	0.191	0.75
5	0.08	0.163	0.57
6	0.07	0.147	0.53

TABLE 6.2: Targeting accuracy using up to 6 markers. Length of the needle equal to 120 mm. Standard deviation equal to 0.08 mm.

Markers	St Dev(mm)	Mean Error(mm)	Max Error(mm)
3	0.4	0.59	2.9
4	0.17	0.31	1.24
5	0.12	0.23	0.78
6	0.09	0.18	0.59

6.4 Discussion and Conclusion

The proposed localization method was employed to localize the endorectal probe and the biopsy needle in MRI-guided transrectal prostate biopsy. The proposed interventional MRI system was presented and the design of the endorectal probe and the delivery mechanism were explained. Nominal position and orientation of probe and biopsy needle were defined in relation to three semiactive markers embedded within the probe.

Localization of the probe and needle within the scanner frame included paired-point assignment of the measured markers to the nominal markers and Least-Squares fitting of the nominal markers to the measured markers. The obtained transformation matrix was used to compute direction and position of the biopsy needle in the scanner frame.

Monte Carlo simulations were performed to quantify the targeting accuracy. Targeting accuracy was computed as Euclidean distance between the measured tip of the needle in the scanner frame and the nominal tip of the needle. A maximum targeting error of 1 mm was estimated and a similar result was obtained in the MR scanner. Improvement in the targeting accuracy was predicted by implementing Monte Carlo simulation for more than three markers; using 6 markers the targeting error reduced by up to a factor of two.

6.4.1 Failure scenario in probe localization

When estimating position and orientation of the probe from the computed points, it is essential to correctly assign each computed point to its corresponding marker. In view of the steps explained in Section 6.2, a situation of tracking failure would result from a mis-assignment of the computed coordinates to the markers.

In tracking of the probe two tests for identifying mis-assignment were introduced. For each updated position, i) the distances between the markers were computed and compared with the know distances and ii) the distance between consecutive positions of the markers were computed and compared with a realistic step. For both tests and in a case of failure, the computed positions were discarded and the position of the probe

was not updated.

It is important to underline that loss of signal may occur when the marker is at some angle to the main field, which may result in failure to detect a marker. Design of the probe and kinematics of the robot were such that markers were kept perpendicular to the main field in all positions of the device during the procedure, maximizing the peak amplitudes during tracking.

Chapter 7

Guidance in MRI-guided transrectal prostate biopsy

One of the main benefits of a fast localization method is to enable the implementation of navigational aids, such as automatic update of the plane through the instrument. As a result, a more robust, consistent and accurate image-based guidance of the instrument is achieved.

This Chapter describes the developed software for visual guidance of the endorectal probe and biopsy needle. The software, which was implemented on the external navigation workstation, was design to meet the needs of the procedure workflow explained in Chapter 6. It provides 3D anatomical images visualization, display of the current locations of the probe and needle, and visualization of the plane through the needle. The suggested trajectory to the selected target and the current distances from the needle to the target are also provided to enable an easier and faster targeting. Furthermore, filtering of the measured data was implemented, resulting in a more consistent monitoring of the instrument.

Pre-clinical targeting trails were conducted in a 1.5 T Siemens Avanto MR Scanner by clinician Prof. Nandita Desouza at Royal Marsden Hospital (Sutton, London, UK). These were performed on a male prostate phantom which was built by other members of the research group to represent adequately the male pelvic anatomy.

7.1 Visualization of the imaging volume

The acquired anatomical MR images are in DICOM format, which uses a right handed LPH (Left-Posterior-Head) coordinates system centred at the isocentre of the MR scanner and oriented according to the patient position on the scanner table, as illustrated in

Figure 7.1(a).

Position and orientation of an image within the MR scanner are included in the header of the DICOM file under the tags *ImagePositionPatient* and *ImageOrientationPatient*, respectively. The tag *ImagePositionPatient* specifies x, y, and z coordinates of the first transmitted pixel of the image, which corresponds to the upper left hand corner of the image (*TLC*) or pixel (1,1) as displayed in MatLab; the tag *ImageOrientationPatient* includes two vectors which specify direction cosines of rows and columns of the image, as shown in Figure 7.1. Further image information, such as size of a pixel and dimensions of an image, are also included in the file header and the MatLab function *dicominfo* was used to access them.

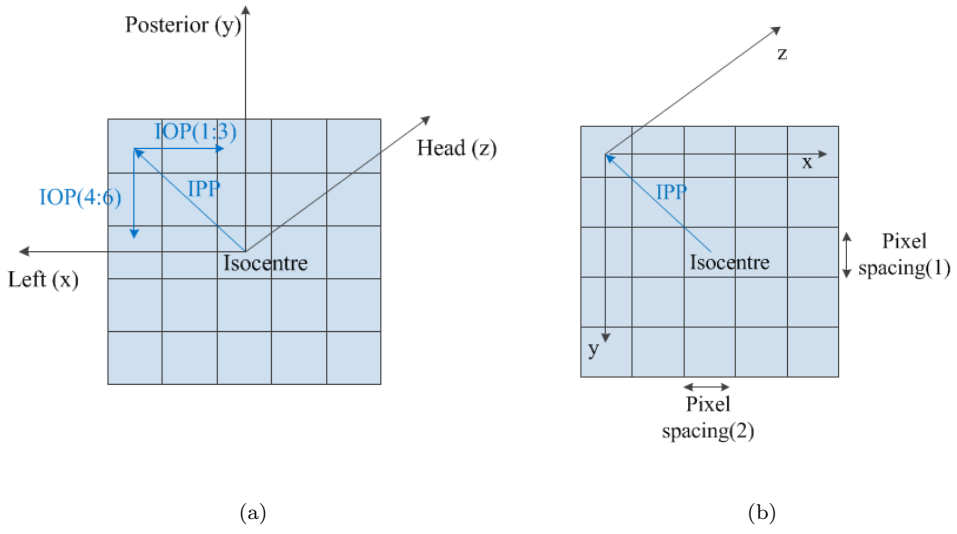


FIGURE 7.1: LPH coordinate system for patient in prone position. IPP=image position patient, IOP=image orientation patient. a) Definition of the DICOM image within the MR scanner volume. b) Image coordinate system in MatLab environment.

The visualization functionality was implemented such that the received DICOM images are first ordered according to ascending z-coordinate, from the feet towards the head of the patient, and second, operations of flipping up-down and left-right are performed on each slice to show the patient in the prone position as seen by a person standing at his feet. The operator may scroll through the displayed slices, change the 3D point of view, zoom in-out and visualize sagittal and coronal planes which are given by interpolation through the acquired MR images. All this is performed by keyboard commands.

Figure 7.2 shows visualization of a set of transverse MR images acquired for a healthy volunteer in the prone position. In this view, the displayed transverse and sagittal slices are through the middle of the prostate, while the coronal slice is slightly below the prostate.

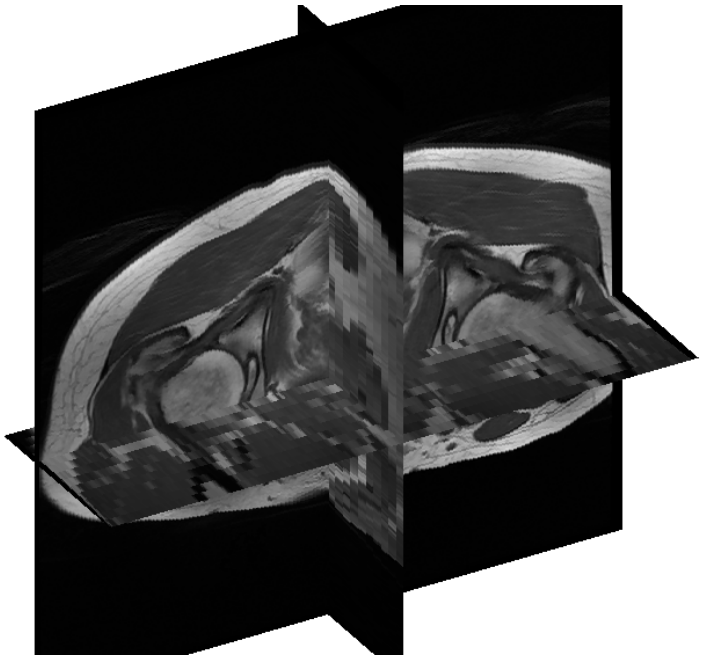


FIGURE 7.2: Display of the MR anatomical images on the navigation workstation. MR transverse images are acquired and visualized in 3D. Sagittal and coronal planes are interpolated through the acquired transverse images.

7.2 Display of Endorectal probe and biopsy needle

7.2.1 Markers coordinates in the imaging volume

When a new set of 1D projections is received, the coordinates of the markers are computed by means of the localization algorithm presented in Chapter 5. In order to provide a correct display of the instrument in relation to the anatomical target, the computed markers must be firstly related to the imaging volume.

As illustrated in Figure 7.3, the computed coordinates of a marker, (M_x, M_y, M_z), and the slice position, (IPP_x, IPP_y, IPP_z), are both with respect to the isocentre of the MR scanner, which is also the middle of the slice. The following transformations were implemented to bring the marker to the imaging volume:

$$\begin{aligned} M_x^{'} &= 1 + \frac{M_x - IPP_x}{pixelSpacing} \\ M_y^{'} &= 1 + \frac{M_y - IPP_y}{pixelSpacing} \\ M_z^{'} &= 1 + \frac{(M_z - IPP_z)}{sliceDistance} \end{aligned} \tag{7.1}$$

where $pixelSpacing$ is the size of a pixel in mm and $sliceDistance$ is the distance between the centres of consecutive slices in mm. The addition of 1 is due to the fact that the first pixel has coordinates (1,1,1).

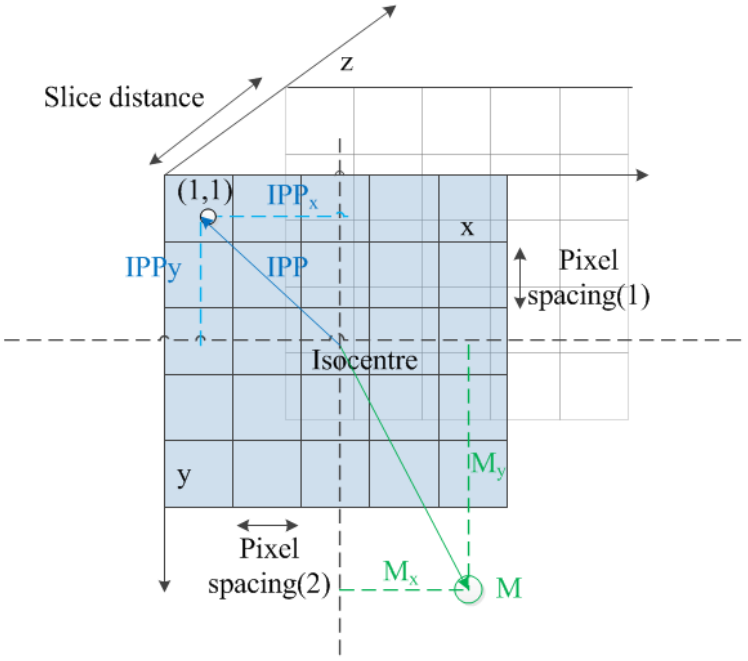


FIGURE 7.3: RF marker within the image coordinate system. The computed coordinates of the RF marker are to the isocentre of the MR scanner and must be translated into image coordinates.

Since the operations of flipping the y axis upside-down and the x axis left-right are performed on the images, as explained above, the same operations must be performed on the markers. The flipped coordinates $(M_x^{''}, M_y^{''}, M_z^{''})$ of a marker were computed as:

$$\begin{aligned} M_x^{''} &= 1 + sizeX - M_x^{'} \\ M_y^{''} &= 1 + sizeY - M_y^{'} \\ M_z^{''} &= M_z^{'} \end{aligned} \tag{7.2}$$

where $sizeX$ and $sizeY$ are respectively width and height of an image in mm.

By substituting $(M_x^{'}, M_y^{'}, M_z^{'})$ in Equations 7.2 with Equations 7.1, $(M_x^{''}, M_y^{''}, M_z^{''})$ coordinates are expressed in terms of (M_x, M_y, M_z) coordinates:

$$\begin{aligned} M_x^{''} &= 1 + sizeX - (1 + \frac{M_x - IPP_x}{pixelSpacing}) \\ M_y^{''} &= 1 + sizeY - (1 + \frac{M_y - IPP_y}{pixelSpacing}) \\ M_z^{''} &= 1 + \frac{(M_z - IPP_z)}{sliceDistance} \end{aligned} \tag{7.3}$$

which was implemented as:

$$\begin{aligned} M_x^{''} &= \frac{-M_x + IPP_x + sizeX \cdot pixelSpacing}{pixelSpacing} \\ M_y^{''} &= \frac{-M_y + IPP_y + sizeY \cdot pixelSpacing}{pixelSpacing} \\ M_z^{''} &= 1 + \frac{(M_z - IPP_z)}{sliceDistance} \end{aligned} \tag{7.4}$$

Location of the probe and needle within the imaging volume was computed using the markers coordinates given in Equations 7.4.

7.2.2 Graphical Display

Tracking of the endorectal probe and biopsy needle was explained in Chapter 6. It involves paired-point assignment of the measured markers to the nominal markers and Least-Squares fitting for measurement error minimization. During the procedure, the operations of assignment and alignment are performed for each set of measured markers and prior to update of display of the probe and needle.

Figures 7.4 and 7.5 show the graphical models which represent the probe and needle. The probe is displayed as a thick blue line corresponding to the needle guide and the length of the probe. The needle is displayed as a thin yellow line corresponding to the needle after firing. The length of the needle after firing was set equal to 60 mm.

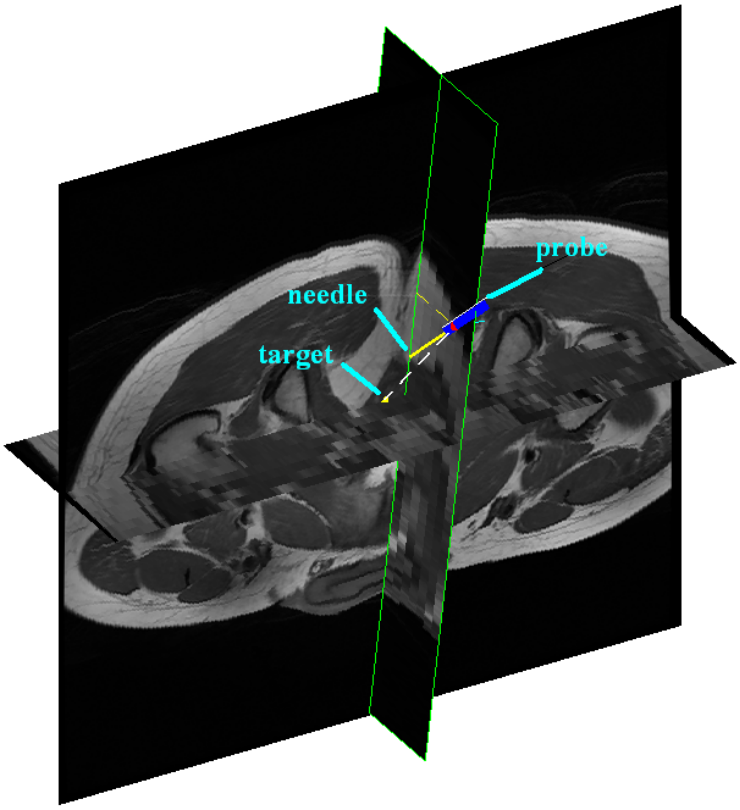


FIGURE 7.4: Graphical user interface. The thick blue lines represents the probe and the thin yellow line represents the needle. The dashed white line is the suggested trajectory, which is through the target (yellow dot) and the remote-centre of motion (red dot).

7.3 Enhanced guidance

7.3.1 Target selection and suggested trajectory

Target selection is performed by the operator at the workstation on the displayed anatomical MR images. The operator adjusts the axial, coronal and sagittal planes so that their intersection coincides with the identified target and, as the operator presses the target selection key, the program computes the coordinates of the target as intersection of the three planes. The suggested trajectory to the target is provided as a line through the target and the remote-centre of the manipulator, as shown in Figures 7.4 and 7.5.

Computation of the remote-centre in the scanner frame is performed automatically, as soon as the movement starts. It is performed only once as the remote-centre does not change during operations of translation and rotation of the probe, unless the manipulator base has been moved. The remote-centre is computed on the basis of the directional vectors of the probe in the initial and current positions. It is calculated as the average of the two closest points on the two lines defined by the two directional vectors [Glassner,

1998]:

$$rc = t^{'} + s * pd \tag{7.5}$$

with

$$s = \frac{Det[(t^{'} - t), pd, pd^{'} \times pd]}{|pd^{'} \times pd|} \tag{7.6}$$

where $t^{'}$ and $pd^{'}$ are the current tip position and unit probe direction and t and pd are the tip position and unit probe direction at the initial probe position.

The clinician rotates the probe so that its corresponding displayed model is aligned with the suggested direction and translates the probe so that the biopsy needle, displayed as after firing, goes through the aimed target. Such display technique was based on clinicians requirements.

7.3.2 Updated plane and Distances from the target

For more intuitive perception, the oblique plane of the parallelogram mechanism of the manipulator, which is defined by the needle and the manipulator main axis of rotation, is interpolated through the transversal slices and updated during the entire targeting procedure, as shown in Figure 7.5.

At each new set of 1D projections, the program computes the angle between the previous location and the current location of the probe, using the dot product of the two directional vectors projected in the XY plane, then it rotates the plane for this angle about the z axis using the remote-centre of the manipulator as centre of rotation.

In order to achieve more accurate, faster and easier targeting, the program also provides the distances from the target to the oblique plane, to the probe directional vector and to the tip of the needle, as after firing. Visualization screenshots taken while performing pre-clinical trials are shown in Section 7.5.

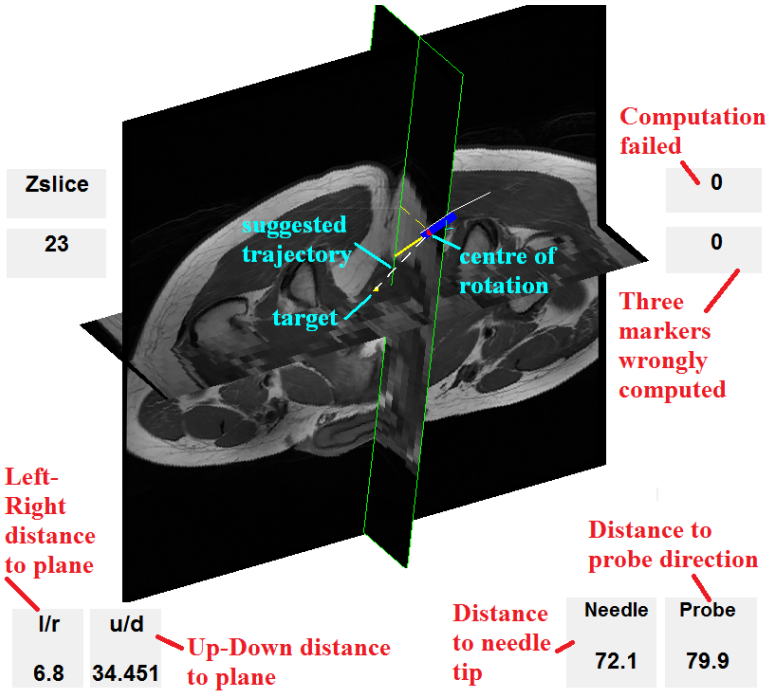


FIGURE 7.5: Graphical user interface. The suggested trajectory is the line connecting the computed remote-centre and the selected target. The distances are in mm.

7.4 Filtering of the measured data

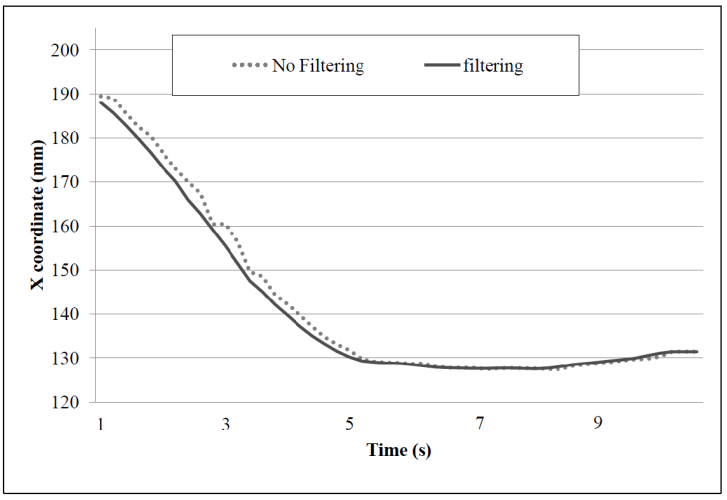
While performing the procedure, it was noticed that jittering of the displayed needle and probe may occur. This was attributed to the localization error and to imperfections in the device mechanism. By plotting the measured positions of the needle tip in time, fluctuations were observed. Such fluctuations should be smoothed out to provide a more reliable guidance of the instrument. With this aim, filtering techniques may be applied [Teukolsky et al., 1986].

In order to verify the improvement in the display when a filtering technique is applied, a simple moving average filter was implemented, as suggested by [Teukolsky et al., 1986]. This filter replaces each measured point, $x[i]$, with the average of this measured point and its M preceding measured points:

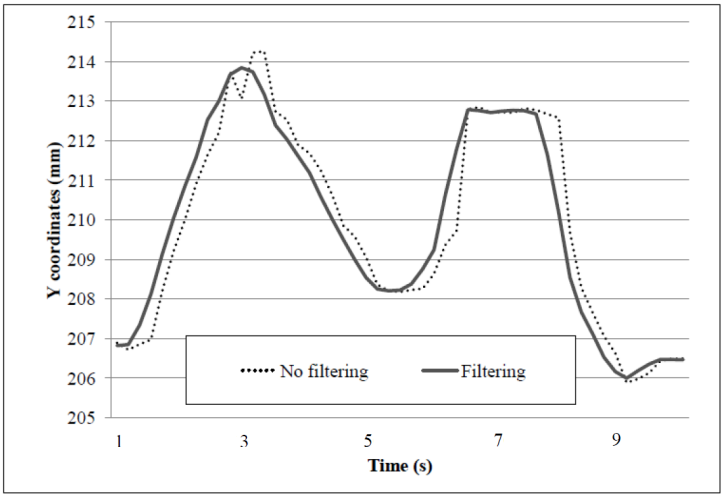
$$x_f = \frac{1}{M} \sum_{j=0}^{M-1} x[i+j] \tag{7.7}$$

where x_f is the filtered position, and M is the number of points used in the moving average. Owing to the fast localization, preceding points of the averaged point measure very nearly the same underlying value, at least in a final stage of the tracking where movements are small. Therefore, averaging reduces the level of noise without biasing the value obtained.

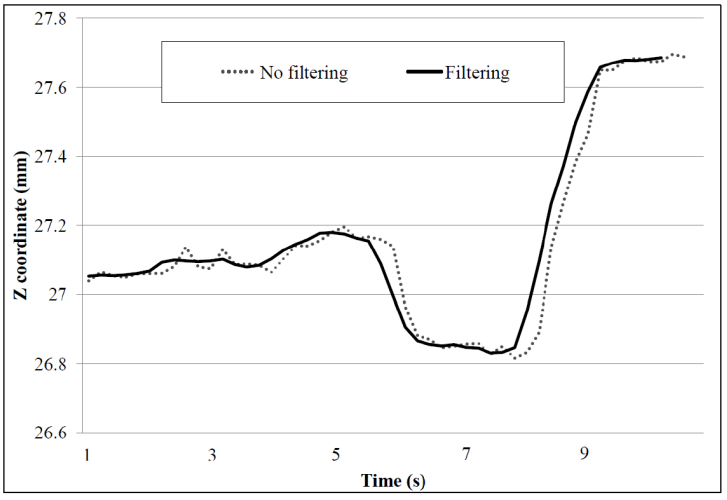
Figure 7.6 shows results of the averaging procedure applied to real measured data obtained in a navigation experiment, with $M = 5$. The components of the measured points along the three main axes are shown with and without filtering. It can be noticed that by applying the average filtering the fluctuations are smoothed out. However, this method introduces undesirable delay, that is perceived in the regions of faster change and negligible in the regions of slower change. As high accuracy of the tracking is needed only in the last stage of the targeting procedure, when the movements of the probe are small and slow, the delay introduced, which is of the order of a few tenths of a second, does not affect the targeting. As a natural improvement to the method of moving average Kalman filtering may be considered [Teukolsky et al., 1986].



(a)



(b)



(c)

FIGURE 7.6: Coordinates of the tip of the needle. The tip of the needle was computed for the real acquired data during the procedure and the graphs show the results with and without moving average filtering.

7.5 Pre-clinical trials

The design of the interventional system was presented in Chapter 6, Section 6.1. Figures 7.7 and 7.8 show the navigation workstation in the control room and the shielded monitor in the scanner room, respectively. Figure 7.9 shows the MRI-compatible manipulator and the male pelvic phantom set-up on the MR scanner table.

The silicon phantom was made by other members of the research group, modelled on a subject volunteer in the prone position to represent adequately the male pelvic anatomy, both internally and externally. The phantom houses anus, rectum and an empty cavity for placement of a prostate phantom, shown in Figure 7.10. Prostate phantoms were constructed as gelatine assemblies of diameter equal to about 40 mm. Five prostate phantoms were constructed, each of them including realistic targets of diameter between 5 mm and 10 mm, representative of lesions. Small targets were made by injecting a drop of vinegar into the the prostate, while large targets were made by inserting a piece of lard. Examples of targets are shown in Figure 7.11.

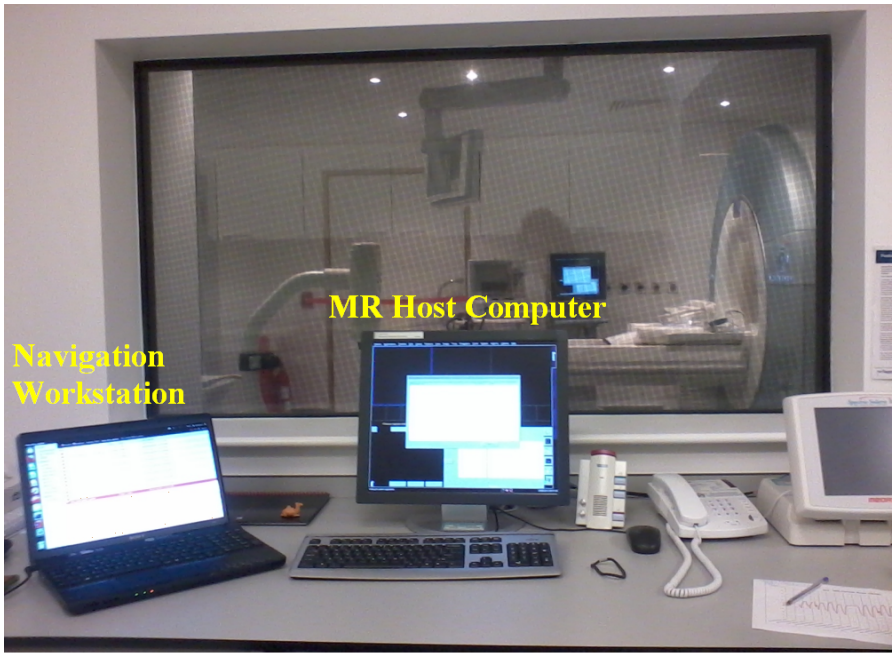


FIGURE 7.7: MRI-guidance set up. Navigation workstation in the control room.

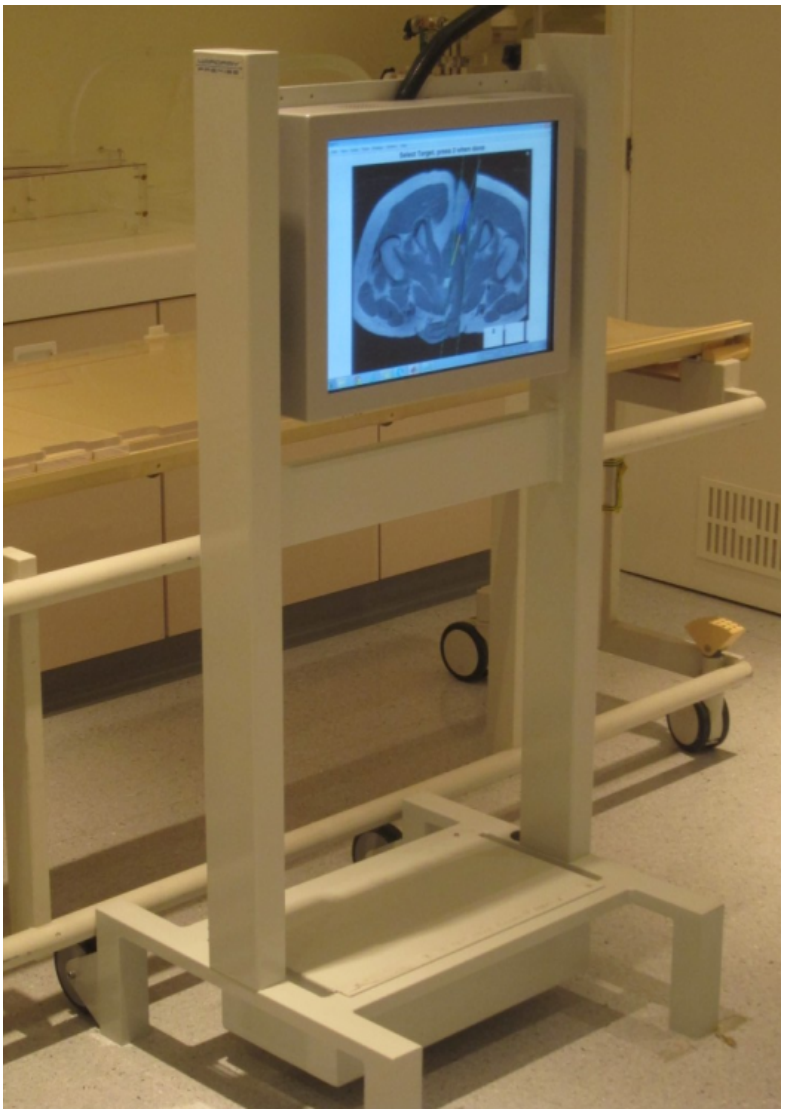


FIGURE 7.8: MRI-guidance set up. Shielded monitor in the MR scanner room.

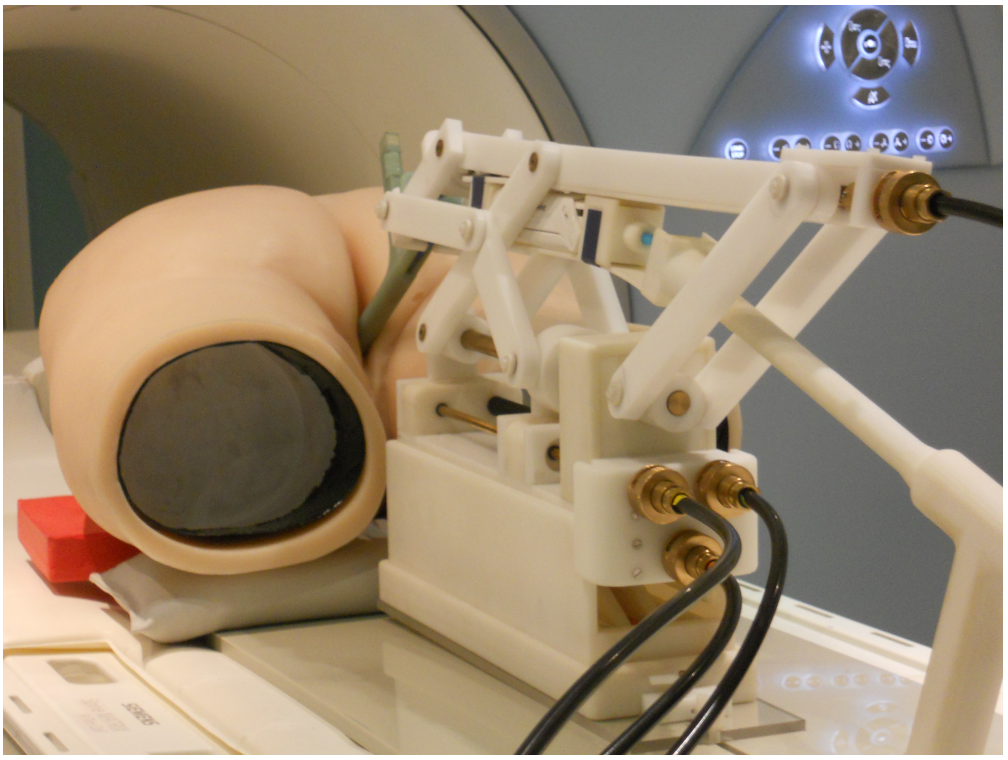


FIGURE 7.9: Manipulator and pelvic phantom on the scanner table.

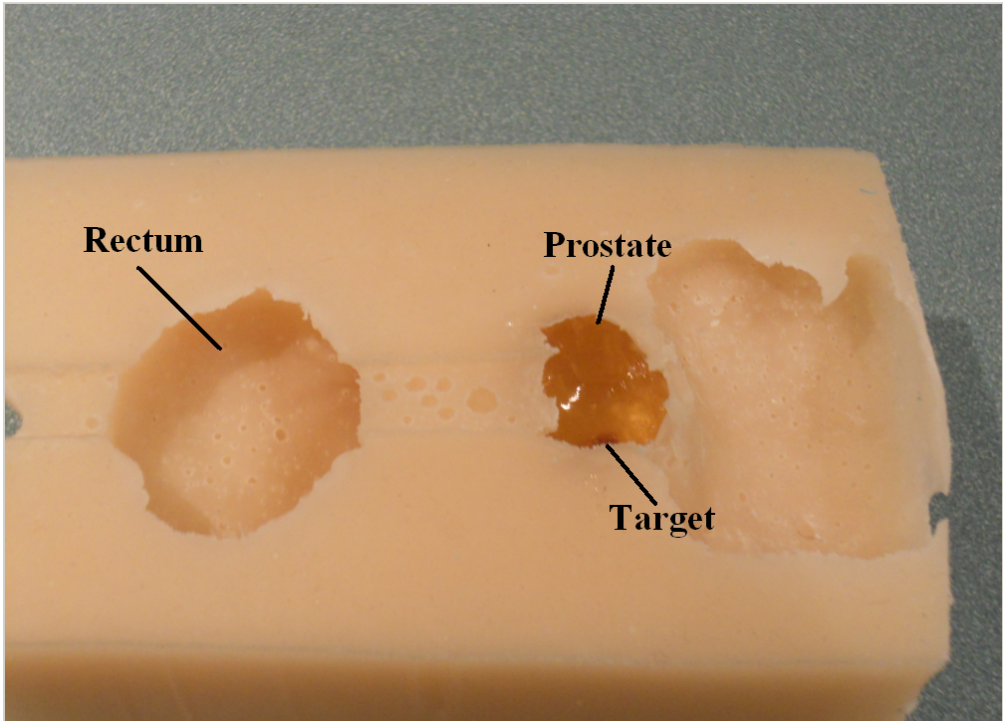
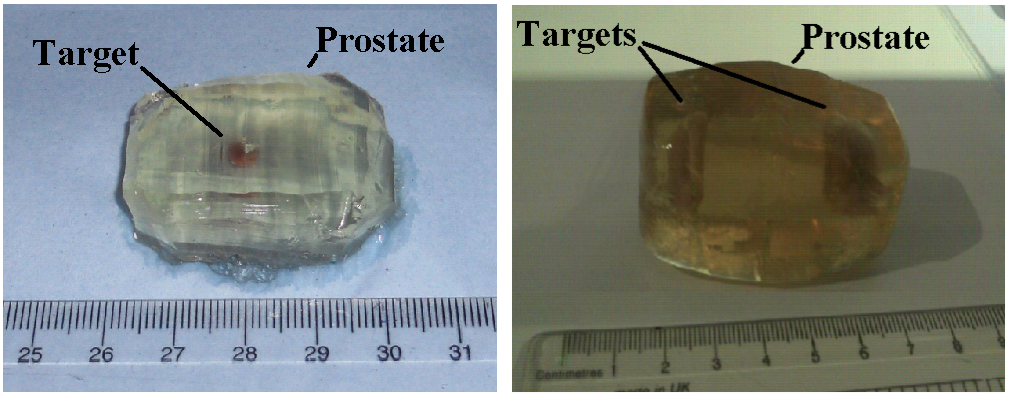


FIGURE 7.10: Inner section of the male pelvic phantom.



(a) (b)

FIGURE 7.11: Targets in the prostate. The targets were created (a) by injecting a drop of vinegar or (b) by inserting a piece of lard inside water-gel assembly (prostate).

7.5.1 Targeting outcome

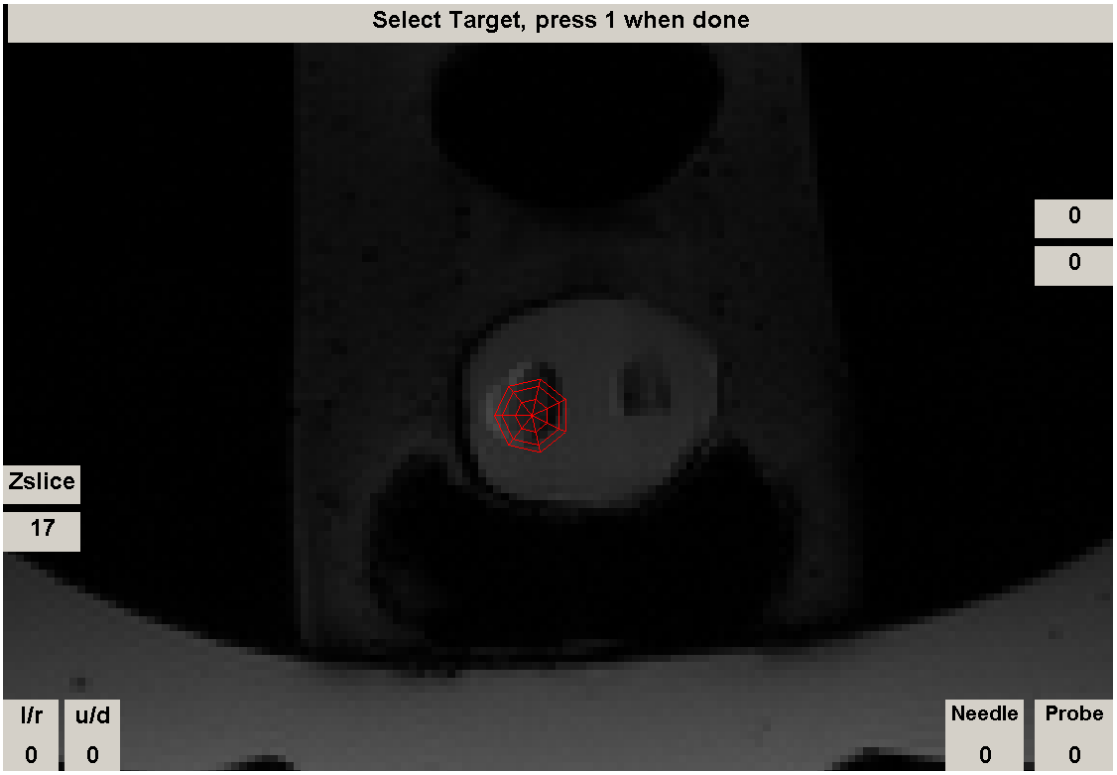
MR images of the phantom were acquired using T_2-weighted Turbo Spin Echo sequence with parameters as reported in Table 7.1. These are the parameters routinely used in prostate imaging. In order to provide a good overall view of the anatomy 20 slices were acquired.

Figure 7.12 shows screenshots of the graphical user interface during the procedure. In this trial, the prostate phantom shown in Figure 7.11(b) was employed. In Figure 7.12(a) the two targets are clearly visible. The displayed red sphere indicates that the clinician selected the target on the left. Figure 7.12(b) and Figure 7.12(c) show stages of the targeting procedure. The trajectory to the target, the plane through the needle defined by the parallelogram mechanism of the manipulator, and the distances from needle tip and probe line up to the target are displayed. Figure 7.12(d) shows probe and needle just before firing. The anatomical images were at this stage acquired and updated. Also, it can be observed that the algorithm successfully computed the markers' positions for all the received sets of 1D projections.

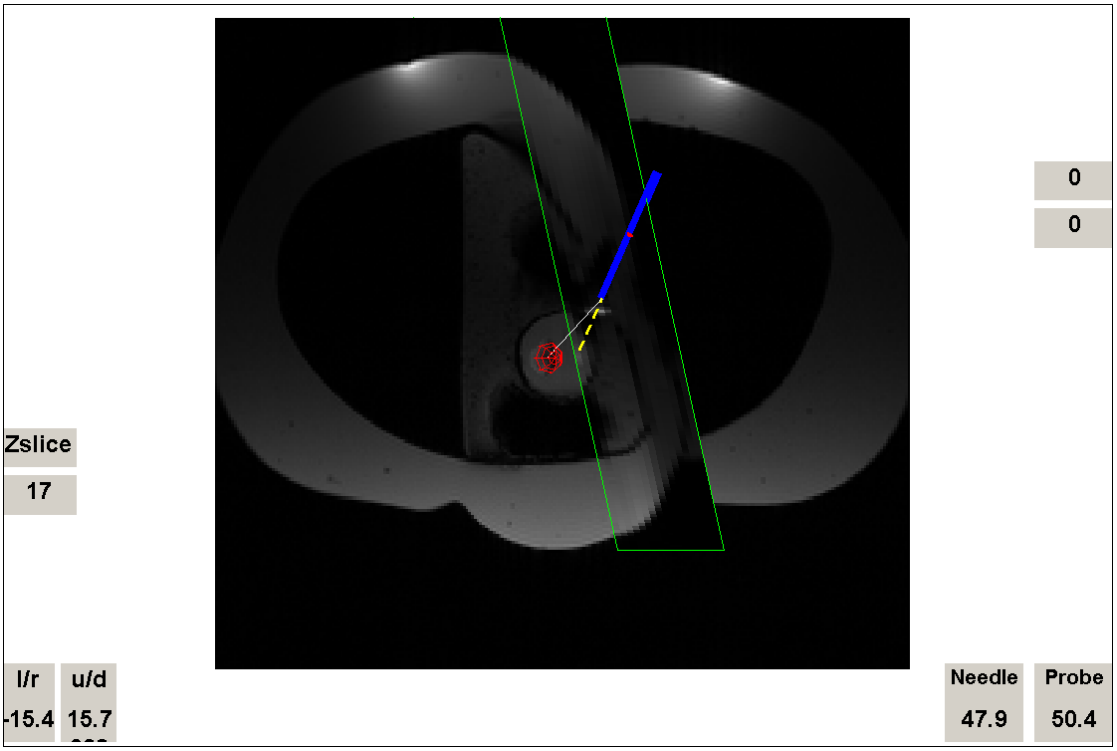
Figure 7.13(a) shows the prostate phantom after firing. Figure 7.13(b) shows the result of another trial using a smaller target similar to the one shown in Figure 7.11(a). In both cases the trace is through the target. Figure 7.14 show a sagittal slice which was acquired to show the needle after firing in situ. It can be noticed that the tip of the needle is through the target. A total of five trials were performed and similar results were obtained in each trial. The average time taken for completing a targeting procedure was about 5 minutes.

TABLE 7.1: Parameters of the sequence Turbo Spin Echo.

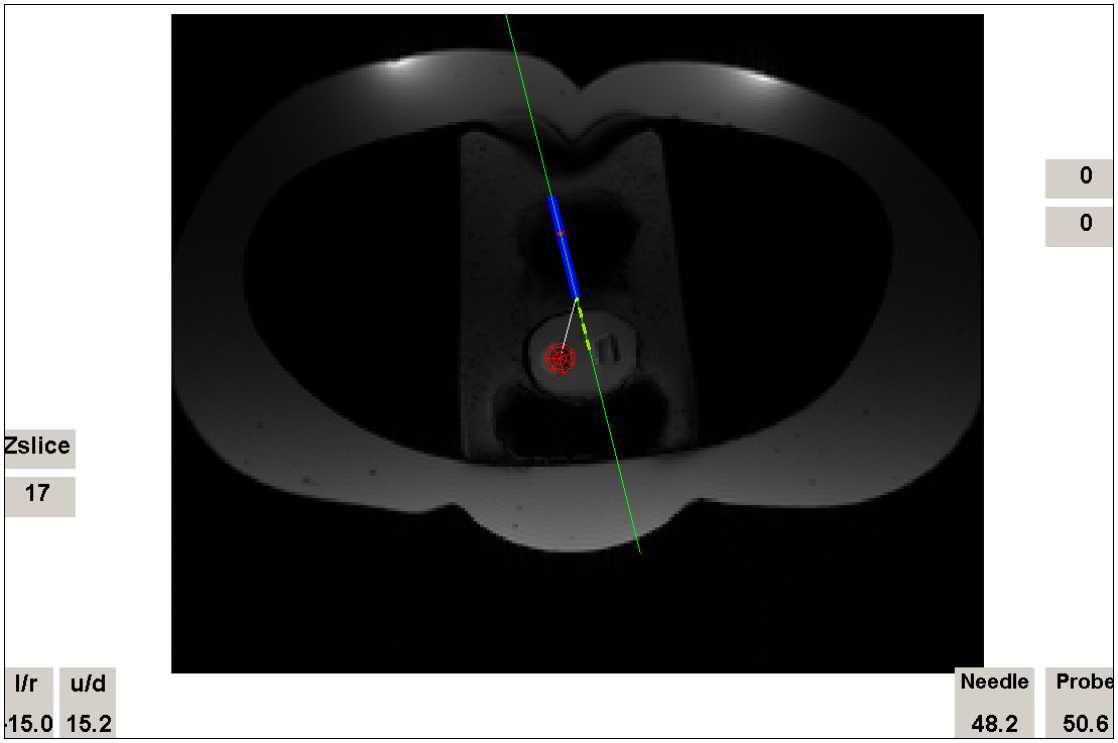
TR (ms)	3670
TE (ms)	121
Flip angle (°)	137
Slice thickness (mm)	3-5
Pixel spacing (mm)	0.688
Distance factor (%)	10
Turbo factor	23


Select Target, press 1 when done
0
0
Zslice
17
l/r
0
u/d
0
Needle
0
Probe
0

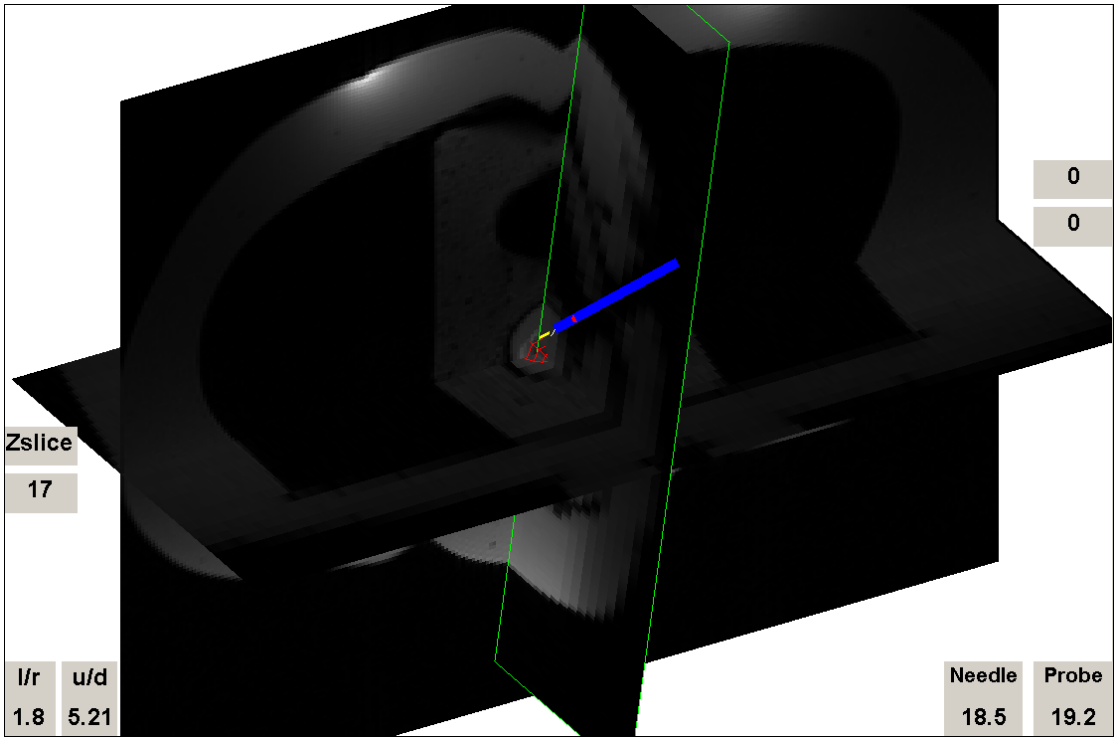
(a)


0
0
Zslice
17
l/r
-15.4
u/d
15.7
Needle
47.9
Probe
50.4

(b)

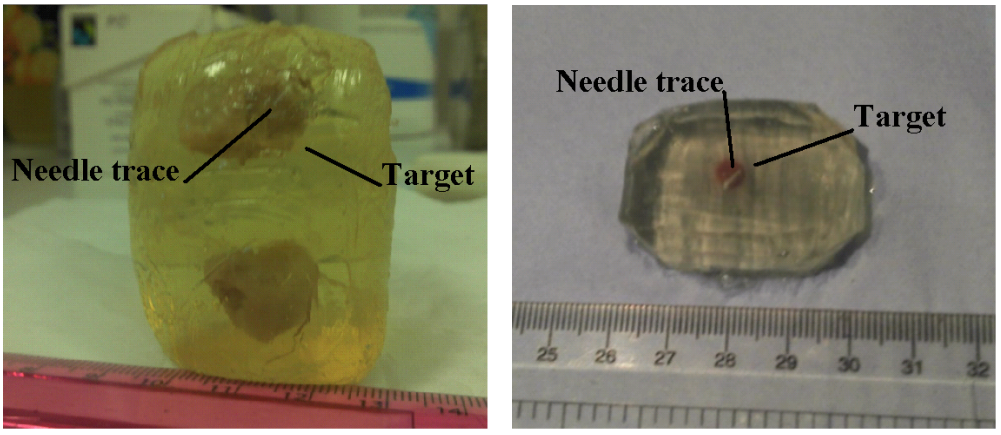


(c)



(d)

FIGURE 7.12: Screenshots of the graphical interface while performing pre-clinical trials.(a) Target selected; (b) and (c) while guiding the probe towards the target; (d) before firing the needle.



(a) (b)

FIGURE 7.13: MRI-guided targeting trials. The trace through the targets left by the biopsy needle is indicated.

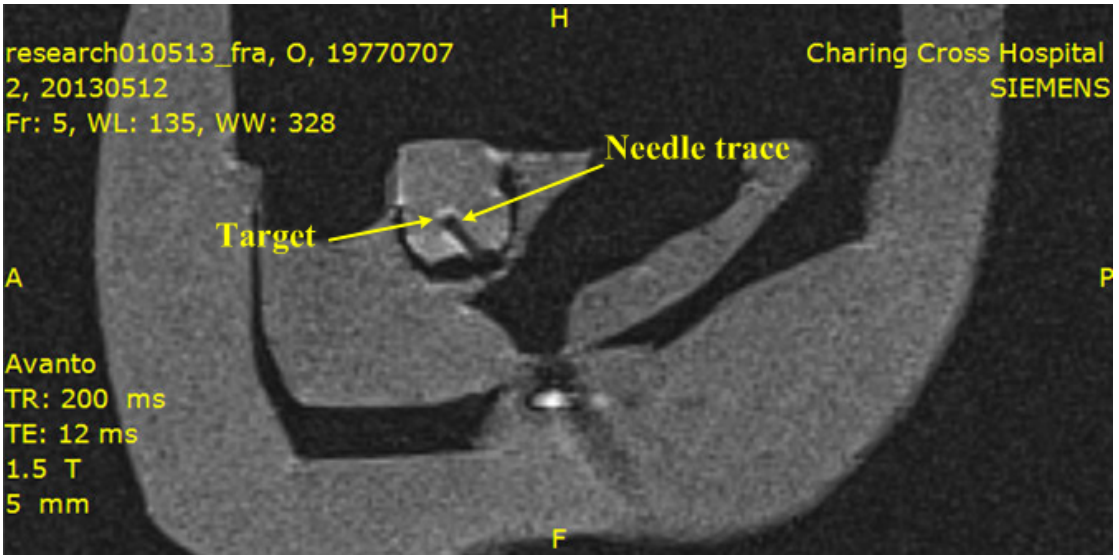


FIGURE 7.14: Confirmation MR image after firing. In the sagittal slice it can be seen that the tip of the needle is through the target.

7.6 Discussion and conclusions

This Chapter presented the visualization software that was developed in order to provide intuitive and reliable visual guidance of the instruments within the patient's body. The acquired transversal MR images were uploaded and visualized together with sagittal and coronal planes interpolated through the slices. Models of the probe and biopsy needle, as it would be after firing, were displayed within the imaging volume. The suggested trajectory to the selected target was provided as the line through the remote-centre and the target. The oblique plane containing the needle was interpolated

through the slices and updated at each new location of the probe. The distances from the target to this plane, as well as to the probe directional vector and to the needle tip were displayed for an easier and more accurate targeting. Filtering of the measured data was also implemented and, as a result, jittering of the displayed needle and probe was considerably reduced.

The system was tested in a pre-clinical environment. A male pelvic phantom was constructed within the project to represent the internal and external anatomy. Initial targeting trials were successfully performed on targets of diameter between 5 mm and 10 mm; the average time needed to complete a targeting procedure was 5 minutes.

Chapter 8

RF receiver array for MRI-guided Transrectal Prostate Biopsy

MRI-guided transrectal prostate biopsy ideally requires interleaving of biopsy needle tracking with imaging of the target lesions, in view of tissue movements during the intervention [Tadayyon et al., 2011]. Updates of needle and target locations provide a more accurate suggested trajectory to the clinician which results in a more accurate targeting of suspected lesions.

Imaging of target lesions while performing the intervention demands an MR signal detector which does not inhibit the clinical workflow. Diagnostic MR imaging of the prostate is routinely performed by means of pelvic array and endorectal balloon coils used in combination; however, endorectal balloon coils are not suitable for transrectal biopsy procedures, while pelvic array alone does not provide adequate signal. As an alternative to endorectal balloon coils, endorectal probes with an incorporated small solid surface coil and needle guide have been proposed [Krieger et al., 2011][Elhawary et al., 2010]. However, the field of view of these coils is small due to acceptable coil sizes and they do inevitably restrict the probe movements. In many cases clinicians perform transrectal prostate biopsy by means of pelvic coil alone [Beyersdorff et al., 2005] [Engelhard et al., 2006]. This is a good solution in terms of biopsy probe movements and patient safety and distress but unsatisfactory in terms of target imaging. Images of a target lesion may be further compromised by the need to relocate pelvic coil elements to better accommodate robot and probe.

There is therefore need for an optimal detector suitable for MRI-guided prostate biopsy procedures. In this Chapter a novel external receiver array is proposed, for which the design was produced based on volunteer subjects and optimized for use with a MRI-compatible manipulator and endorectal probe. Design of the array, performance

assessment and construction are explained. Initial results in a 1.5 T Siemens Avanto MR Scanner are reported and compared to a standard pelvic array coil.

8.1 Design of the receiver

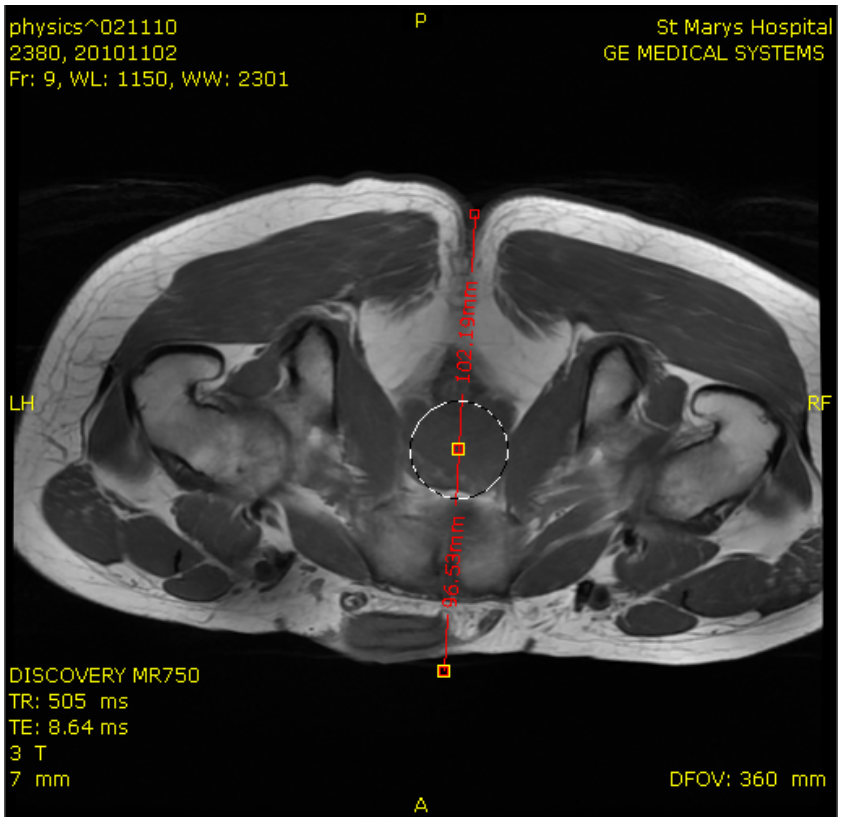
8.1.1 Definition of the region of interest

Design of the receiver array firstly depends on the region of interest, which comprises the prostatic area. As the aim was to design an external array, the region of interest was identified and related to the outer anatomy. To this end, high resolution cross-section sagittal and transverse MR images of the male pelvic anatomy were acquired for a subject in the prone position. The prostate was identified in both cross-sectional views and its distances from the outer contour of the body were estimated using the Dicom viewer software Sante Dicom [from: http://users.forth net.gr/ath/mkanell].

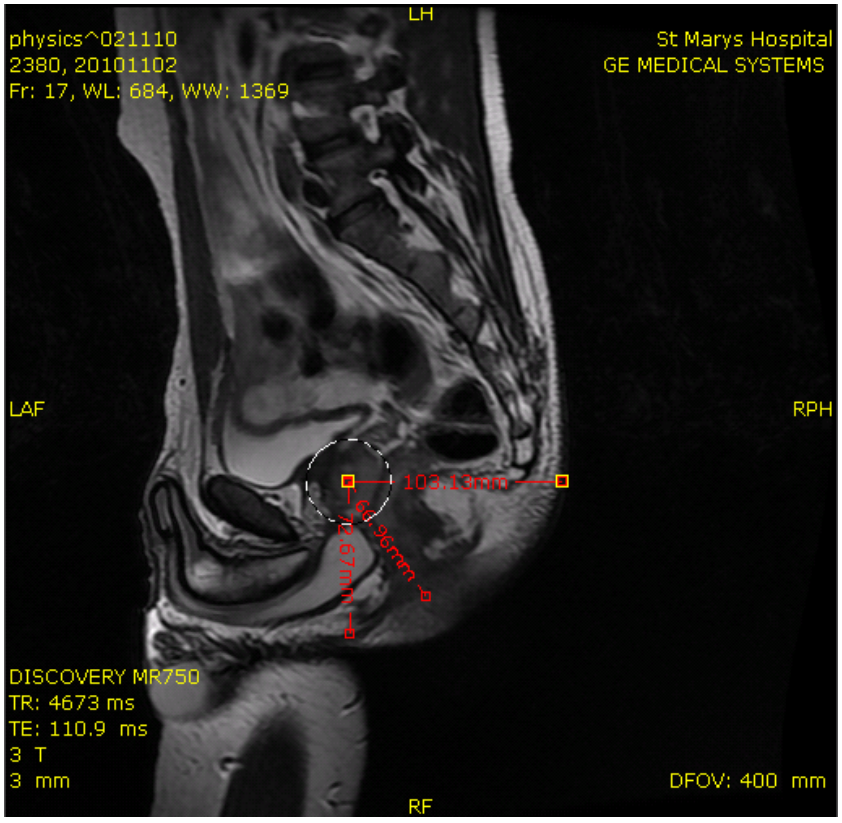
Two cross-sections, axial and sagittal, centred at the prostate are shown in Figure 8.1. A circle identifies the prostate. The distances were measured from the centre of the prostate to reference points in the external anatomy, namely the pelvic area, the anus and the front-back parts. The distances are reported in Table 8.1. In order to maximize the detected signal, the receiver coil was designed so that it surrounds the region of interest and the distances from its surfaces to the region of interest are minimized.

TABLE 8.1: Anatomical distances. The distances are defined as: PP=prostate-perineal body; PA=prostate-anus; PF=prostate-anterior; Pp=prostate-posterior

PP (mm)	PA(mm)	PF(mm)	Pp(mm)
73 ± 3	67 ± 3	103 ± 3	96 ± 3



(a)



(b)

FIGURE 8.1: Pelvic anatomy. (a) Axial and (b) Sagittal cross-sections of the prostatic area were acquired on a GE 3T MR scanner with GRE sequence and parameters as specified in the images.

8.1.2 Geometry of the detector

In order to follow closely the exterior body contour, an asymmetric array of two anterior and three posterior trapezoidal loops was devised, with each loop tapered toward the perineal body. Single loop design produces a maximum magnetic field at about the centre of the loop plane and directed perpendicularly to the loop plane; therefore, sensitivity to the transversal component of the MR magnetization vector was maximized by orienting the normals to the planes of each loop as much as possible toward the y axis of the MR scanner. In order to compensate for the small angle with the y axis at the midpoint (perineal body), the central pair of trapezoids was configured as a figure-of-eight or butterfly coil, a geometry which has been previously successfully employed in MRI to solve the problem of signal loss due to orientation of a RF surface coil within the MR scanner [Di Luzio et al., 1998]. Unlike a single loop surface coil, a butterfly coil in fact produces a magnetic field that in the central region of the coil is substantially parallel to the coil plane. The angle between cross overlapping conductors of the butterfly coil was designed to be 150°, which was proved to be optimal by Kumar and Bottomley [2008] in terms of sensitivity of the coil in its central region.

The final geometry of the detector is shown in Figure 8.2 and Figure 8.3. The geometry comprises four elements, three single loop surface coils and a butterfly coil. Neighbouring elements were partially overlapped in order to minimize the mutual coupling between nearest neighbours. The overlapping fractions between pairs of elements were estimated on the basis of simulations performed with mutual inductance calculation software FastHenry, as explained in the next Section. Dimensions and orientation with respect to the y axis were defined on a volunteer and were considered indicative for an average male subject. The butterfly coil (Element 1) comprises two symmetrical trapezoidal loops whose height is 70 mm and bases are 70 mm and 120 mm. One loop is at an angle of 30° with respect to the y axis and overlaps a trapezoidal loop (Element 2) which is at an angle of 70° with respect to the y axis and whose height is 90 mm and bases are 120 mm and 190 mm. The other loop is at 20° to the y axis and overlaps a trapezoidal loop (Element 3) which is at 65° to the y axis and with height 140 mm and bases 120 mm and 250 mm. This loop, in turn, overlaps a rectangular loop with dimensions 250 mm and 50 mm and perpendicular to the y axis. Importantly, the design accommodates the transrectal biopsy probe, through one of the loops (Element 3), and the manipulator, as shown in Figure 8.4. This loop was designed so that the anus is approximately coincident with its centre. If we imagine a circle around the anus to indicate the available space, this circle would have radius equal to about 50 mm. This space was considered sufficient to avoid any obstruction to the movements of the probe inside the rectum.

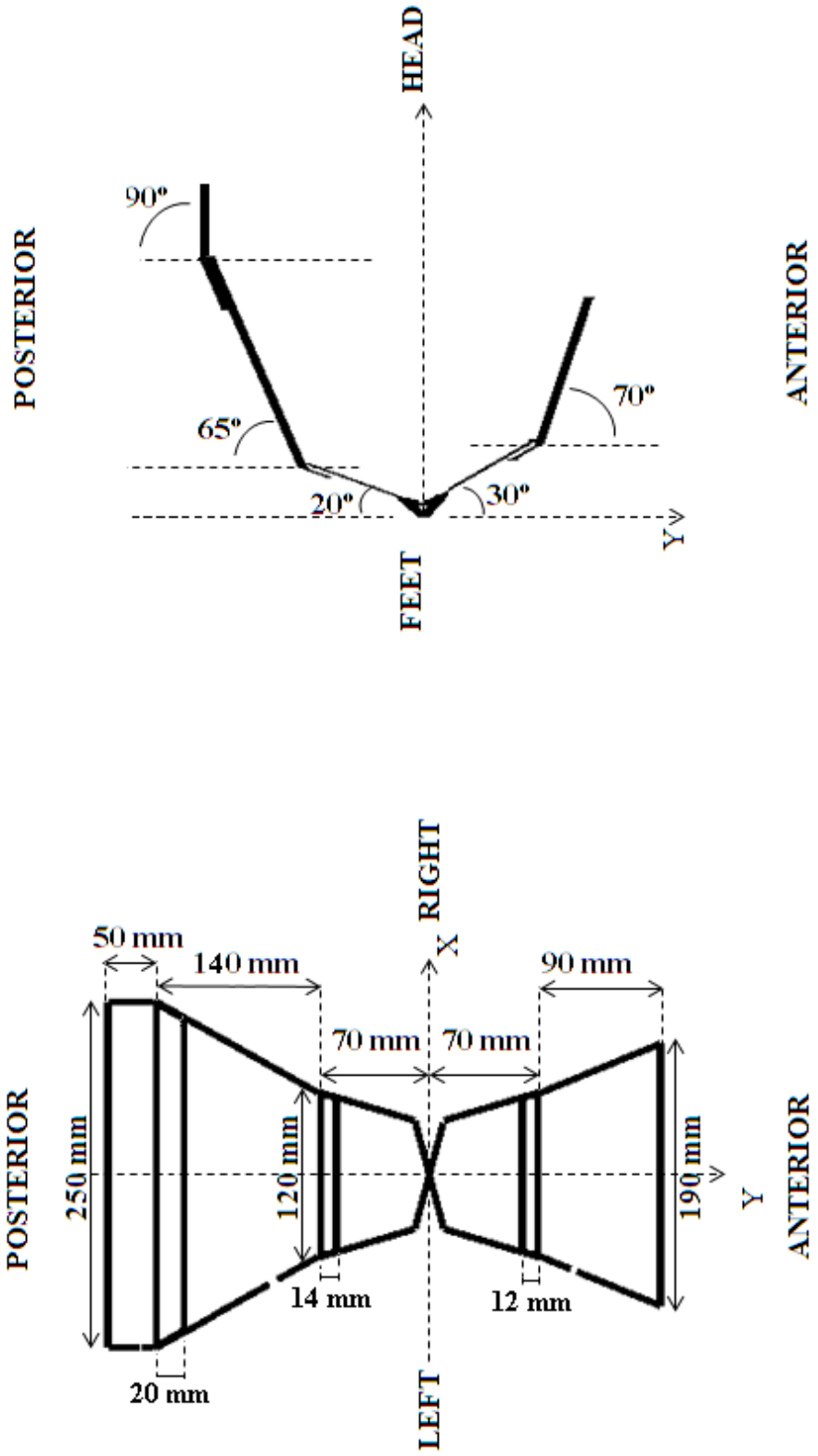


FIGURE 8.2: Design of the array. (a) Top planar and (b) aside tapered configuration of the array. The dimensions of the array and the angles to the y axis of each element are outlined. The overlapping distances were the result of simulations and experiments (Section 8.2).

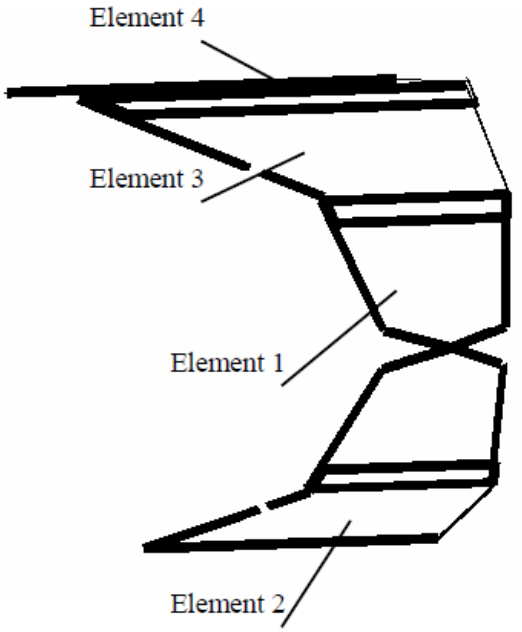


FIGURE 8.3: 3D view of the array. Each element of the array is labelled for later analysis of the performance.

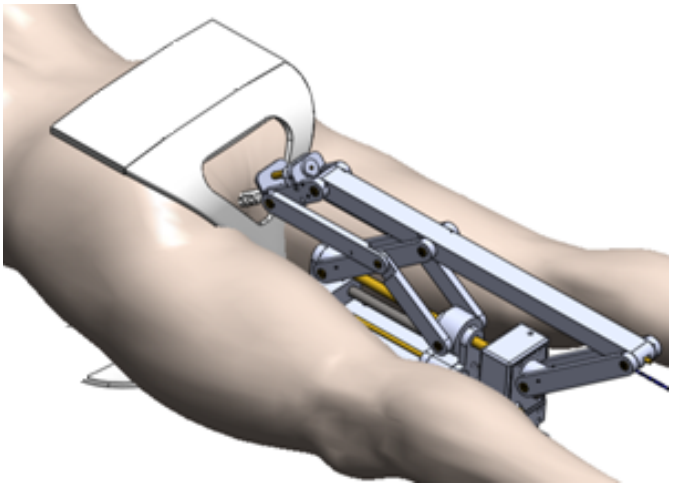


FIGURE 8.4: Integration of the array with a device for MRI-guided transrectal prostate biopsy. The array is meant to be compatible with a manipulator for performing transrectal prostate biopsy. The manipulator shown here was made by other members of the research group [Lambert et al., 2012]. Different manipulators may be employed.

8.2 Overlapping of neighbouring coil elements

Partial overlapping of receiver array loops was employed in order to cancel the total magnetic flux linkage between neighboring elements and therefore minimize their mutual inductances. Mutual inductances were calculated by using the mutual inductance calculation open source software FastHenry. FastHenry is a program capable

of computing the self and mutual inductances, as well as the resistances, of a generic tridimensional conductive structure, in the magnetoquasistatic approximation [from: http://www.fastfieldsolvers.com/] [Russer, 2006].

The input file required by FastHenry, describing the geometry and defining the frequencies of interest at about 63.8 MHz, was generated in MatLab. This file specified every conductor of the array as a sequence of rectilinear segments connected between 3D points or *nodes*. Every segment had conductivity $\sigma = 5.8 \cdot 10^4 mm\Omega$ and the shape of a rectangular parallelepiped, whose width and height were respectively 5 mm and 0.5 mm, reflecting the cross-section of the copper strip chosen for the array elements, as shown in Figure 8.5.

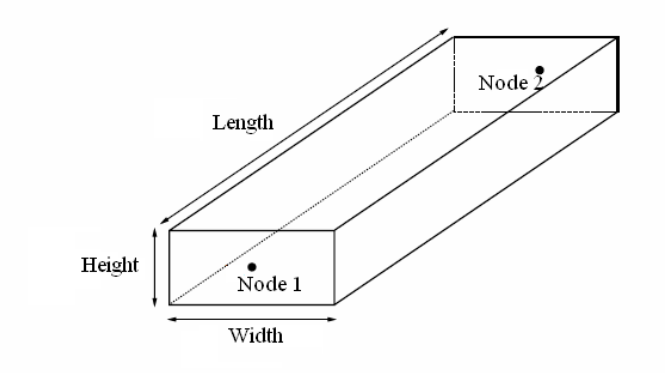


FIGURE 8.5: Segment conductor as defined in the input file to FastHenry. The nodes represents the points of junction with the neighbouring conductors.

The output file generated by FastHenry provided the impedance matrix of the four-element array in the form:

$$Z_{ik} = \begin{bmatrix} R_1 + jL_1\omega & jM_{12}\omega & jM_{13}\omega & jM_{14}\omega \\ jM_{21}\omega & R_2 + jL_2\omega & jM_{23}\omega & jM_{24}\omega \\ jM_{31}\omega & jM_{32}\omega & R_3 + jL_3\omega & jM_{34}\omega \\ jM_{41}\omega & jM_{42}\omega & jM_{43}\omega & R_4 + jL_4\omega \end{bmatrix}$$

with $i, k = 1, 2, 3, 4$. R_i represents the resistance and L_i the self-inductance of the i-element; M_{ik} represents the mutual inductance of the elements i and k, with $i \neq k$, and ω the radial resonance frequency.

The mutual inductances M_{ik} for each pair of elements i and k of the array were calculated by dividing the imaginary part of the impedance by the radial resonance frequency ω. The mutual inductances were computed for a range of overlapping fractions between neighbours in order to find the overlapping fraction which ensures best decoupling.

Figure 8.6 shows the estimated mutual impedances for each element of the array, for

overlapping divisors from 2 up to 9. Element 1 has two close neighbours, namely Element 2 and Element 3. It can be seen from Figure 8.6 (a) that the optimal overlapping fractions are $\frac{1}{5}$ and $\frac{1}{6}$ with Element 2 and Element 3, respectively. For these fractions the mutual impedances reaches in fact a minimum value equal to about $0.110^{-10}\Omega$. It can be noticed that the lower coupling with the far-away neighbour Element 4 slightly decreases by increasing the distance between the two elements. Similarly, Figure 8.6 (b) tells that the optimal overlapping fraction of Element 2 with Element 1 is $\frac{1}{5}$, while the lower coupling with far-away neighbours Element 3 and Element 4 is inversely proportional to the distance between the elements. For Element 3, Figure 8.6 (c), the optimal overlapping distance with Element 1 is $\frac{1}{6}$ and with Element 4 is $\frac{1}{7}$, as also shown in Figure 8.6 (d). These results indicate that mutual coupling between adjacent elements can be minimized by partial overlapping and give an estimation of the optimal overlapping divisor for each pair of loops. In general, partial overlapping has little effect on the low coupling between far-away neighbours. This is the case of the pairs Element 1 and Element 4, Element 2 and Element 3, Element 2 and Element 4. Coupling between far-away neighbours was experimentally evaluated and pre-amplifier decoupling was employed in this case.

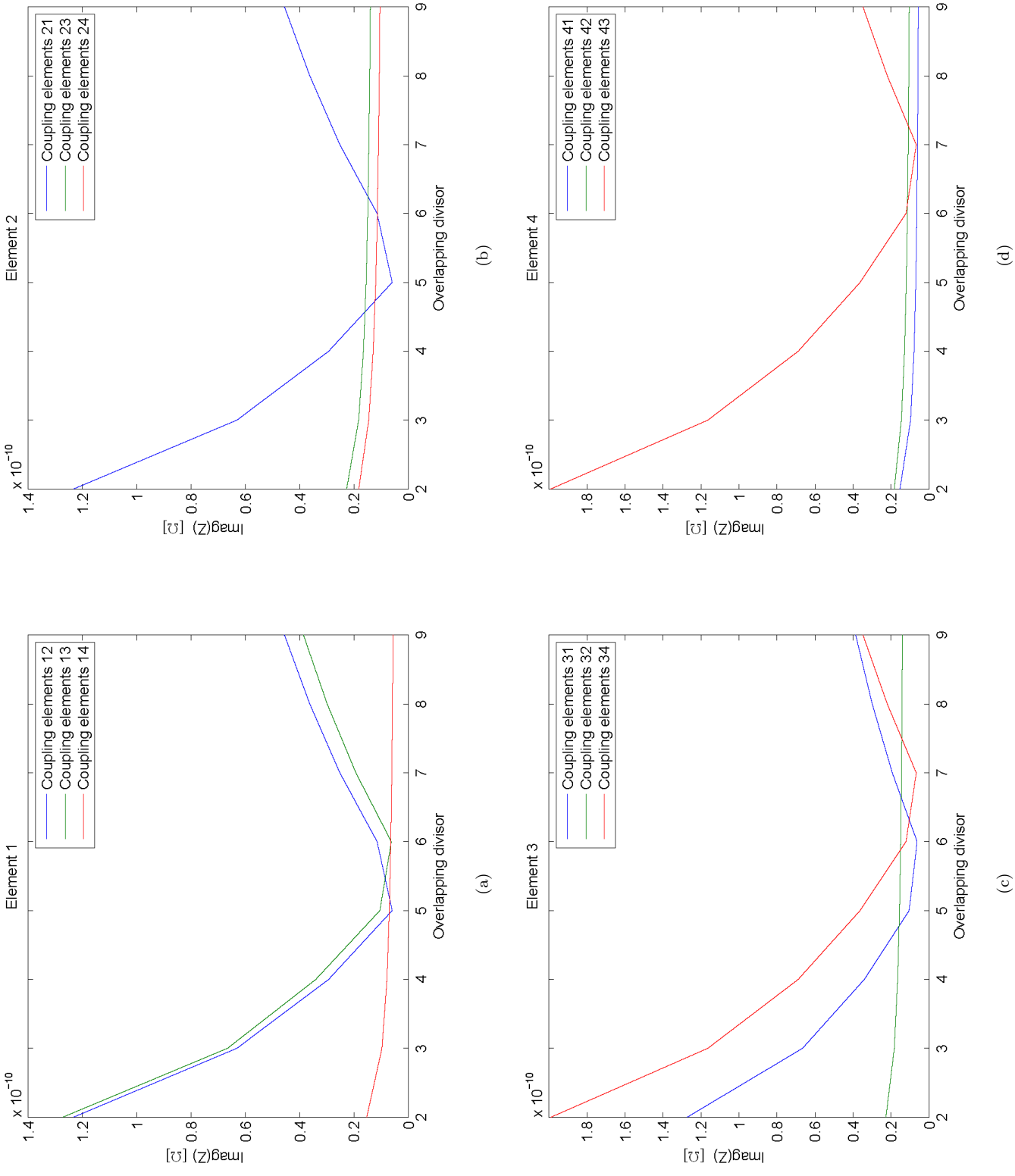


FIGURE 8.6: Overlapping evaluation. The plots show the impedance for each element for increasing overlapping factor. (a) Element 1, (b) Element 2, (c) Element 3, and (d) Element 4.

8.3 Evaluation of the receiver

8.3.1 Magnetic field

The receiver array was evaluated in terms of sensitivity and homogeneity over the region of interest. According to the Theorem of Reciprocity [Hoult, 1978], the sensitivity of the detector to the transversal component of the RF magnetization is proportional to the transversal component of magnetic field generated by unit current flowing in the coil.

By applying Biot-Savart Law, the magnetic field at a point P may be expressed in terms of current I flowing in the coil [Blum and Roller, 1981]:

$$\mathbf{B} = \frac{\mu_0 \mathbf{I}}{4\pi} \oint \frac{d\mathbf{l} \times (\mathbf{r} - \mathbf{r}')}{|\mathbf{r} - \mathbf{r}'|^3} \tag{8.1}$$

where μ_0 is the permeability of free space, $\mathbf{I}d\mathbf{l}$ is the infinitesimal current element and $\mathbf{r} - \mathbf{r}'$ is the vector distance from $\mathbf{I}d\mathbf{l}$ to the field point P.

The configuration of the detector is such that each element may be simplified into straight conductors parallel to the x axis or arbitrarily oriented. On the basis of the Principle of Superposition, the magnetic field $\mathbf{B}$ generated by an element may then be determined by summing the magnetic fields generated by each of the separate straight conductors.

Equation 8.1 was hence developed for a general case of a straight conductor arbitrarily oriented in space. The details of the field computation in terms of the coil coordinates is reported in Appendix B. The obtained expressions for magnitude and direction of the magnetic field at a point in space were implemented in C++ and linked to a main MatLab program in which geometry and orientation of each element were defined. The total magnetic field generated by the array was obtained by applying the Principle of Superposition and contour maps of the sensitivity were computed over the region of interest.

8.3.2 Sensitivity and Homogeneity

Sensitivity and homogeneity were evaluated in the region of interest. The sensitivity was computed as transversal component of the magnetic field $\mathbf{B}$ produced by unit current flowing in the coil. The homogeneity through a slice was computed as $\frac{|B - B_{mid-point}|}{|B_{mid-point}|}$, with $|B_{mid-point}|$ magnetic field at the middle point of the slice.

The complete setup used in the simulations is shown in Figure 8.7, where the distances of the elements of the array from the centre of the prostate were determined in

Section 8.1.1 while the extension of the prostate was defined on the basis of reported cases of prostate cancer [Kimple et al., 2010]. Table 8.2 shows the average dimensions of the prostate for patients with cancer and benign diagnosis along the three main anatomical axes. It can be observed that along anteroposterior and transverse directions the dimensions of the prostate are similar for the two categories of patients, whereas along craniocaudal direction the prostate may increase of about 20 mm in the case of cancer. As a result, a sphere of diameter 50 mm was considered representative of the volume of interest.

TABLE 8.2: Prostate dimensions. The distances are defined as: CC dim: craniocaudal dimension, AP dim: anteroposterior dimension, TR dim: transverse dimension.

	CC (mm)	AP(mm)	TR(mm)
Patients with cancer diagnosis	46.7 ± 17.5	37.6 ± 6.3	48.3 ± 5.8
Patients with benign diagnosis	50.4 ± 7.6	40.4 ± 6.5	50.2 ± 5.5

For comparison, sensitivity and homogeneity were also computed for a standard pelvic coil. This comprised 4 rectangular elements at the front and 4 at the back of the patient with dimensions taken by Siemens technical manual (4-channel flex coil; dimensions: $516mm \times 224mm$; overlapping: 1/3). The frontal part was aligned with the perineal body, while the posterior part was placed slightly higher in order to accommodate the probe and the manipulator, resulting in an offset between the front and back arrays of about 150 mm along z.

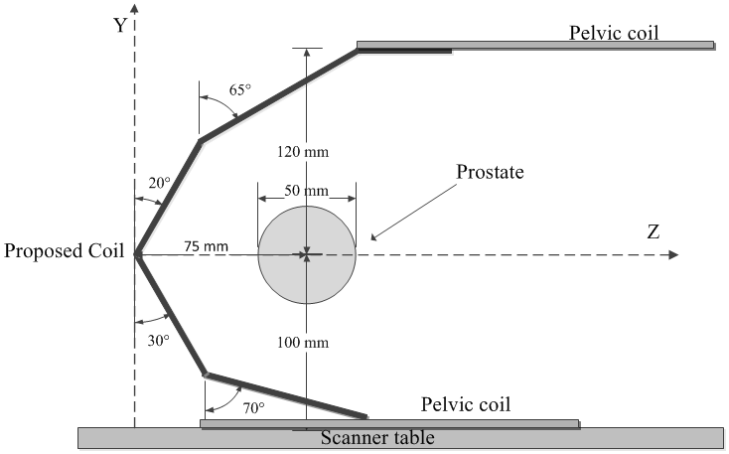
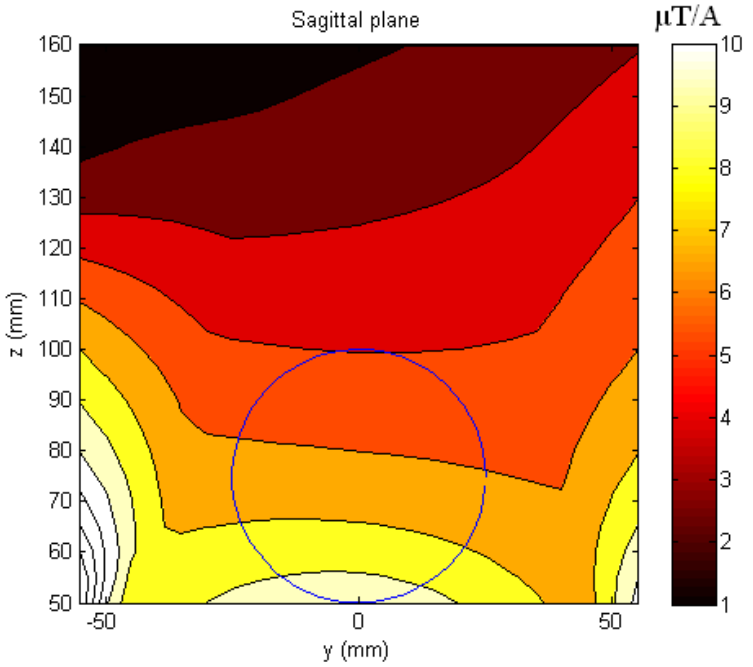


FIGURE 8.7: Envisaged setup of proposed coil and pelvic coil in the MR scanner. This setup was used in the simulations.

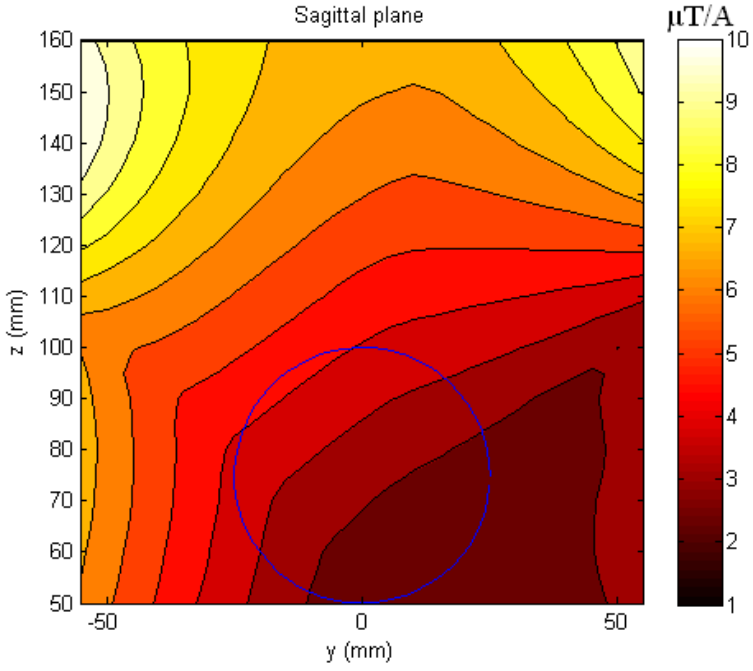
Figures 8.8 and 8.9 show the computed field contour maps in sagittal and axial planes, respectively. Both planes are through the centre of the prostate; the circle, which has diameter 50 mm, indicates the prostate. Each colour on the map represent points on the plane sharing the same field value. The values of the field were mapped in the range

1-10 $\mu TeslaA^{-1}$ using a red color scale. White color corresponds to highest values, while black color corresponds to lowest value.

The field maps indicate that the sensitivity of the proposed coil is appreciably higher than that of a pelvic coil over the entire region of interest. The magnetic field of the proposed coils reaches values about a factor of three higher than the pelvic array. There is an appreciable improvement in the sensitivity over the peripheral zone of the prostate (lower prostate area in Figures 8.8 and 8.9), which is the area where 70% cases of prostatic cancers originate [Center, 2013]. The field of the proposed coil also appears more homogeneous, as can be seen from the distribution of the field contours and further illustrated in Figure 8.10. In this case, the variation of the magnetic field along a line parallel to the y axis and through the middle of the prostate was computed with respect to the field value at the middle of the prostate ($y = 0$ mm, $x = 0$ mm, $z = 75$ mm). The variation was calculated in the sagittal plane (Figure 8.10 (a)) and in the axial plane (Figure 8.10 (b)). It can be noticed that in both planes the variation of the field for the proposed coil is lower than that for the pelvic coil and its value in the region of interest is always below 0.1.

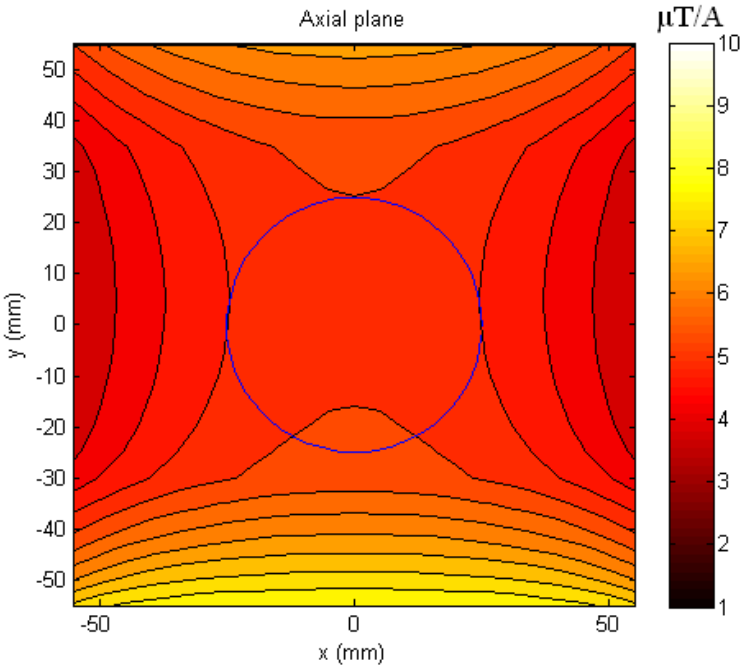


(a)

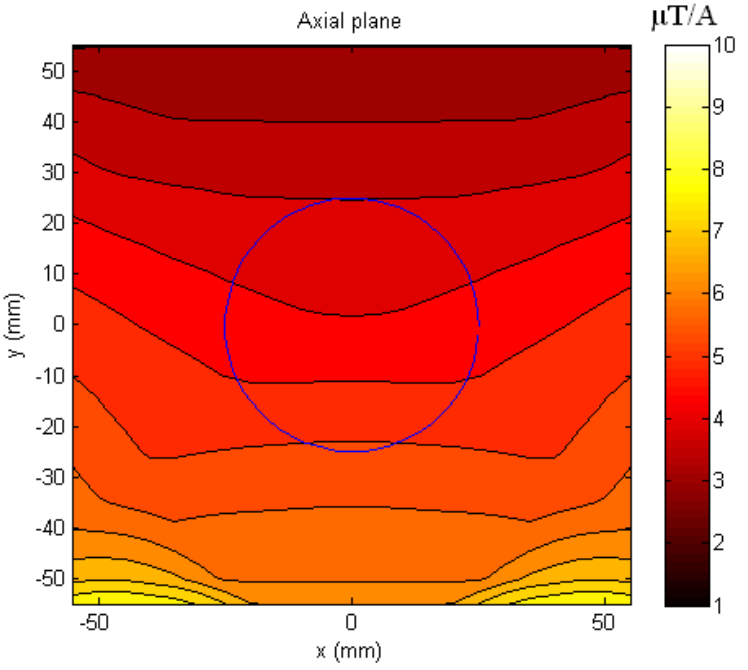


(b)

FIGURE 8.8: Sensitivity maps. (a) Proposed coil and (b) pelvic coil sensitivity in a sagittal plane through the middle of the prostate. The circle represents the prostate.

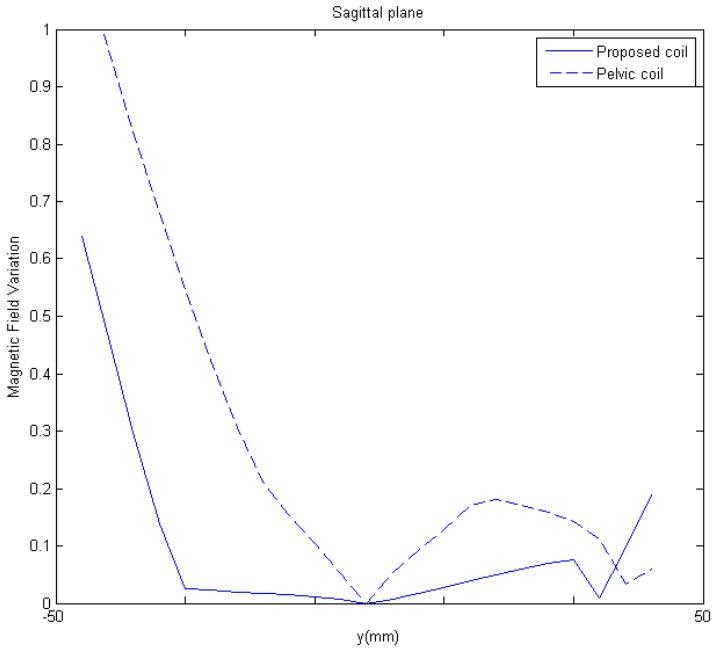


(a)

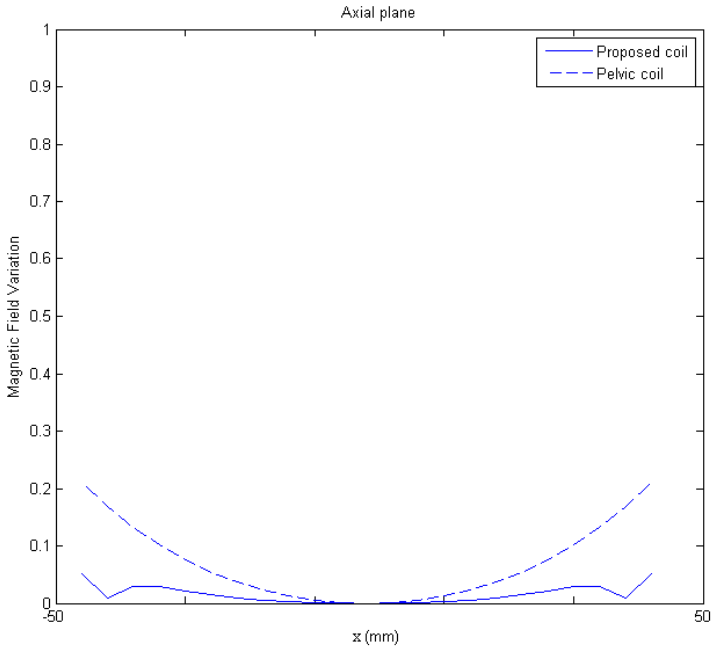


(b)

FIGURE 8.9: Sensitivity maps. (a) Proposed coil and (b) pelvic coil sensitivity in an axial plane through the middle of the prostate. The circle represents the prostate.



(a)



(b)

FIGURE 8.10: Variation of the magnetic field. The variation was computed along a segment through the middle of the prostate and in the (a) Sagittal and (b) Axial planes.

8.4 Manufacturing procedure

The results of the simulations were considered promising in terms of sensitivity and homogeneity of the proposed detector. This section describes how the detector was manufactured and experimentally evaluated. Evaluation involved tests on the bench and in a Siemens 1.5 T Avanto MR Scanner (Charing Cross Hospital, London, UK).

8.4.1 Step 1: Tuning and Matching

In order to ensure higher MR signal amplitude, each element of the array was tuned to the resonance frequency of ^1H at 1.5 T, which is $\nu_0 = 63.87$ MHz. The detected signal was transmitted from the elements to the MR scanner receiver channels by means of 50 Ω transmission lines. According to the *Maximum Power Transfer theorem*, in order to maximize the power transfer from an element to a transmission line, the impedance of the element, *source*, must be matched to that of the 50 Ω transmission line, *load*. These concepts are exhaustively explained in Terman [1943].

Tuning and matching of an element with inductance L involved the use of two capacitors, C_T and C_M, as shown in Figure 8.11. R_L is the impedance of the transmission line and R_S is the impedance of the element. The values of C_M and C_T were estimated as follows.

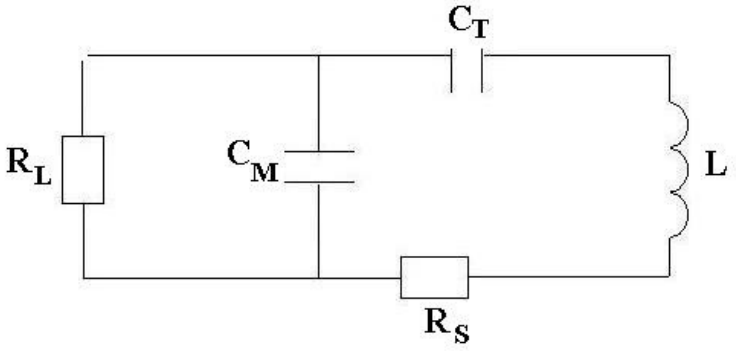


FIGURE 8.11: RF circuit element coil. An element coil, which has inductance L, was tuned to the frequency $\nu_0 = 63.87MHz$ and matched to the impedance R_L of the transmission line by means of two capacitors, C_T and C_M. R_S is the impedance of the element coil. The element coil acts as source of signal and the transmission line as load.

The equivalent impedance of the circuit $R_L C_M$ may be computed as

$$\begin{aligned} Z = \frac{1}{j\omega C_M}\frac{1}{(\frac{1}{j\omega C_M R_L}+1)} &= \frac{1}{j\omega C_M R_L}\frac{R_L}{(\frac{1}{j\omega C_M R_L}+1)} \\ &= \frac{1}{j\omega C_M R_L}\frac{R_L}{(\frac{1}{j\omega C_M R_L}+1)}\frac{1-\frac{1}{j\omega C_M R_L}}{1-\frac{1}{j\omega C_M R_L}} \\ &= \frac{1}{j\omega C_M R_L} R_L \frac{1-\frac{1}{j\omega C_M R_L}}{1+\frac{1}{\omega^2 C_M^2 R_L^2}} \\ &\approx \frac{1}{j\omega C_M R_L} R_L (1-\frac{1}{j\omega C_M R_L}) \\ &= \frac{1}{j\omega C_M} + \frac{1}{\omega^2 C_M^2 R_L} \end{aligned} \tag{8.2}$$

The approximation in Equation 8.2 is possible since $\omega C_M R_L \gg 1$. The circuit $R_L C_M$ is equivalent to a load $R'_L = \frac{1}{\omega^2 C_M^2 R_L}$ in series with a capacitor C_M, as illustrated in Figure 8.12.

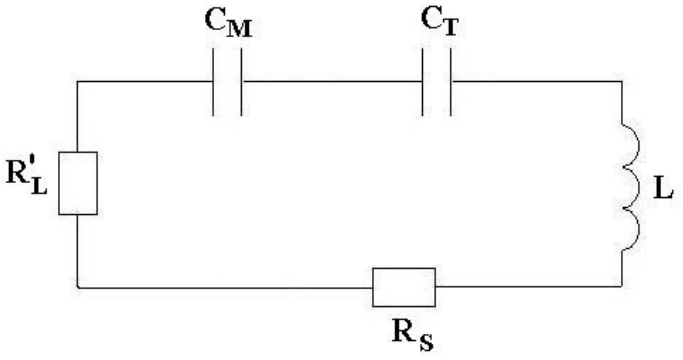


FIGURE 8.12: Circuit equivalent to an RF element coil.

Matching of an element coil requires that the impedance of the source R_S is equal to impedance of the load R'_L, thus $R_S = \frac{1}{\omega^2 C_M^2 R_L}$ and

$$C_M = \frac{1}{\omega\sqrt{R_S R_L}} \tag{8.3}$$

Tuning implies that the equivalent capacitance of the circuit $C_{eq} = \frac{C_T + C_M}{C_T C_M}$ is equal to $\frac{1}{\omega_0^2 L}$, where ω_0 is the resonance radial frequency of the element coil. It follows that

$$C_T = \frac{C_M}{\omega_0^2 L C_M - 1} \tag{8.4}$$

The values of C_M and C_T were computed using Equations 8.3 and 8.4. The inductance L and the resistance R_S of an element coil were experimentally determined. Estimated values of C_M and C_T are reported in Table 8.3. Measurements were performed by means of a Vector Network Analyzer (Anritsu MS 2026A VNA Master). Each element was in turn inductively coupled to the S_{11} transmitting probe and connected via coaxial cable to the S_{12} receiver channel, while the other elements were connected to 50 Ohm terminations. The values of the capacitances were slightly adjusted from the computed values for better tuning and matching. Adjustment was repeated for each step of the procedure.

TABLE 8.3: Estimated values of the added components.

element	$C_M(pF)$	$C_T(pF)$	$R_S(\Omega)$	L(nH)
1	250	13.7	1.95	0.476
2	260	20	1.85	0.334
3	270	16.7	1.75	0.394
4	286	24.4	1.52	0.276

8.4.2 Step 2: Detuning in transmission

Coupling of the receiver with the transmitter during the RF excitation pulse may cause large induced currents in the receivers. This could cause significant disturbance in the local field, potential damages to the electronic components and exceeding the permitted Specific Absorption Rate (SAR) limits [Roemer, 1990] [Fujita et al., 2013]. This was prevented by detuning the receiver during the transmission phase away from its resonance frequency by employing a PIN diode in series with an inductor L_d to form a L_dC_M network, as shown in Figure 8.13. The PIN diode limits the maximum voltage that can develop across the capacitor C_M to 0.5 V, while it permits reception of the MR signal, since the voltage during reception does not exceed this threshold. The induced voltage from the transmit pulse biases the PIN diode on and the carrier lifetime in the PIN diode ensures that the PIN diode conducts during the whole transmit pulse. When the PIN diode is forward biased the parallel circuit L_dC_M is presented at the receiver, as illustrated in Figure 8.13 (b). By tuning the circuit L_dC_M at the frequency of interest, optimal detuning of the receiver coil in transmission was achieved. The value of L_d component was estimated as follows. The impedance Z_r of the receiver coil was computed as

$$Z_r = Z_M \frac{(Z_t + Z_c)}{(Z_t + R_c + Z_c + Z_M)} \tag{8.5}$$

with

$$Z_c = j\omega L; Z_m = \frac{1}{j\omega C_M}; Z_t = \frac{1}{j\omega C_T} \tag{8.6}$$

L_d was found such that $L_d C_M$ resonates at the same radial frequency ω of the receiver:

$$L_d = \frac{1}{\omega^2 C_M} \tag{8.7}$$

The value of L_d was found to be approximately 15 nH for all the elements.
The total impedance of circuit 8.13 (b) was hence computed as

$$Z_{total} = Z_d \frac{Z_r}{(Z_d + Z_r)} \tag{8.8}$$

with

$$Z_d = j\omega L_d \tag{8.9}$$

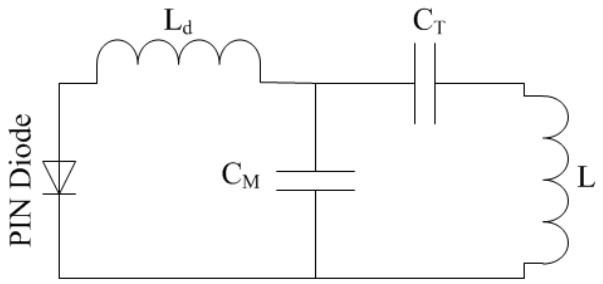
The new resonance frequencies were calculated by applying the Kirchhoff's Second Law to circuit 8.13(b):

$$\begin{cases} i_2 \frac{1}{j\omega C_T} + i_2 j\omega L + (i_2 - i_1)\frac{1}{j\omega C_M} = 0 \\ (i_1 - i_2)\frac{1}{j\omega C_M} + i_1 j\omega L_d = 0 \end{cases} \tag{8.10}$$

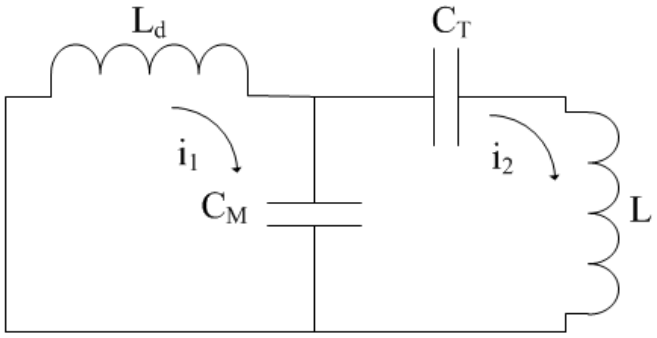
Solving the system in w, the following equation was computed:

$$\omega^4 L L_d C_M C_T + \omega^2(-C_M L_d - C_T L - L_d C_T) + 1 = 0 \tag{8.11}$$

The values of ω correspond to the positive solutions of equation 8.11 and give the locations of the maxima of the impedance in Figure 8.14. The response of the circuit for an off-resonance parallel network $L_d C_M$ was also simulated. The inductance L_d was perturbed of a value equal to about ± 10 nH. It can be noticed from the graph that in over-resonance condition, which corresponds to a higher value of L_d than the estimated one, decoupling is less effective, whereas in lower-resonance condition, which corresponds to a lower value of L_d, decoupling is still effective.



(a)



(b)

FIGURE 8.13: Detuning network. (a) L_dC_M resonant circuit in parallel to the receiver.(b) Equivalent circuit when the PIN diode is forward biased in transmission.

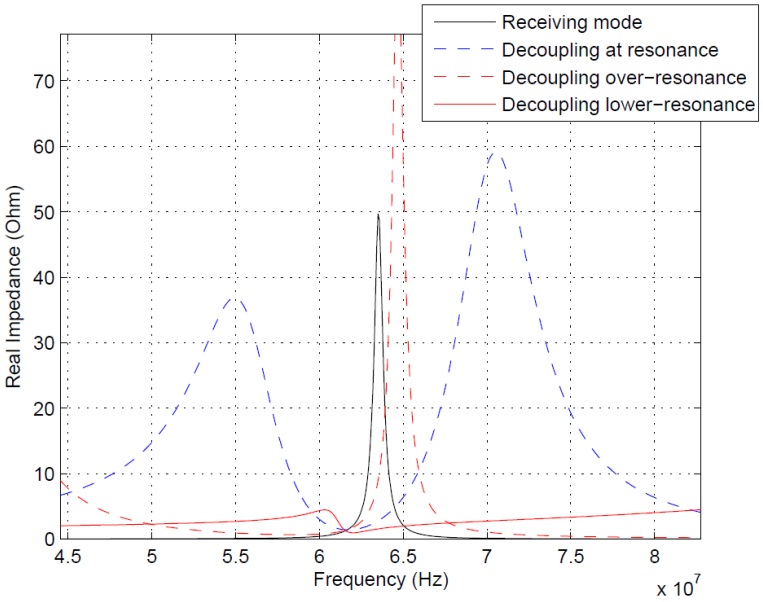


FIGURE 8.14: Real impedance in reception and in transmission stages. Decoupling in transmission was simulated for three values of L_d. Decoupling at Resonance: $L_d = 15nH$, Decoupling over-resonance: $L_d = 25nH$, and Decoupling lower-resonance: $L_d = 5nH$.

Figure 8.15 shows the setup for testing the decoupling of the array in transmission stage on the bench. The reception and transmission phases were recreated by means of a Function Generator and a Vector Network Analyzer. The Function Generator generated a square wave form with periodic transitions between two levels of voltage, 1 V and 0.1 V respectively. The former represented transmission, the latter reception. The square waveform was combined with the S_{11} signal generated by the VNA by means of a 50 Ω 3-way power divider. The third channel of the power divider was connected to the element of the array which was under test. The response was measured using a coupling S_{21} probe.

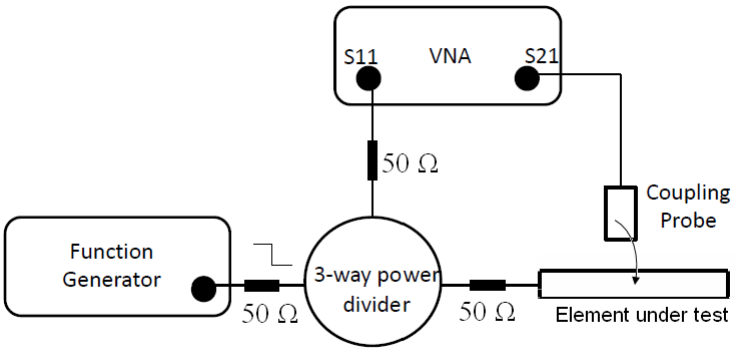


FIGURE 8.15: Block diagram for testing of decoupling in transmission on the bench.

8.4.3 Step 3: Preamplifier decoupling

Second resonance modes which were not cancellable by adjusting the overlapping fraction may be attributed to coupling with far-away neighbours. In order to identify the potential coupling neighbour, pairs of elements were in turn isolated by short circuiting the others. An example of coupling between far-away neighbours is given in Figure 8.16. The graph shows S_{11} and S_{12} responses of Element 2. By applying the explained method, the source of the second resonance mode was identified in Element 3.

Once the coupling neighbour was identified, a low resistance was placed in parallel to this element to simulate the presence of a low impedance preamplifier, as shown in Figure 8.17, and hence to verify the efficiency of the decoupling. In the Siemens MR scanner preamplifiers are integrated within the 4-channel flex interface box, which does simplify the manufacturing procedure.

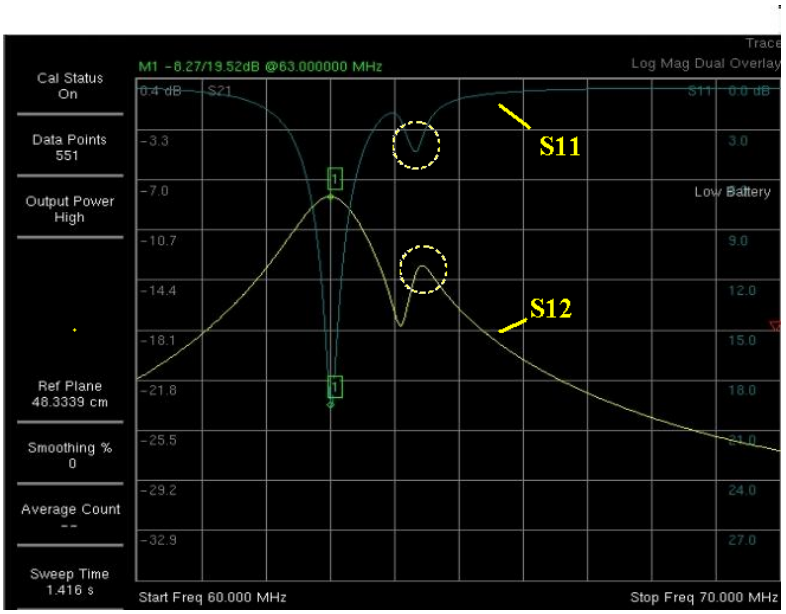


FIGURE 8.16: Example of coupling between far-away neighbours. The second resonance peaks are due to coupling of Element 2 with the far-away neighbour Element 3.

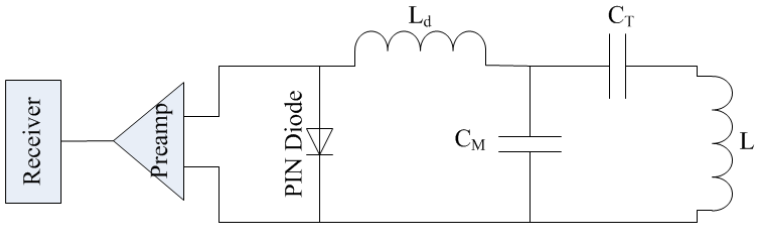


FIGURE 8.17: Low impedance preamplifier added in parallel to the element coil.

8.5 Results

Copper tape of thickness 0.5 mm and width 5 mm was used to trace each element of the array. Transparent thin plastic semi-rigid sheets were used as circuit boards; each element was traced independently on one sheet with the help of a millimetric sheet, as shown in Figure 8.18 (a) in the case of the butterfly coil. The use of semi-rigid sheets gave mechanical flexibility to the elements and thus facilitated the assembly and testing of the array. A plastic support was manufactured in our workshop having shape and dimensions of the detector; after assembling the elements on the support, tuning, matching and decoupling components were added and their values were adjusted (Figure 8.18 (b)). In Figure 8.19 (a) a close view of a miniature circuit presented at an element for matching, tuning and decoupling is shown; in Figure 8.19 (b) the interface connector at the MR scanner is shown.

8.5.1 Results on the bench

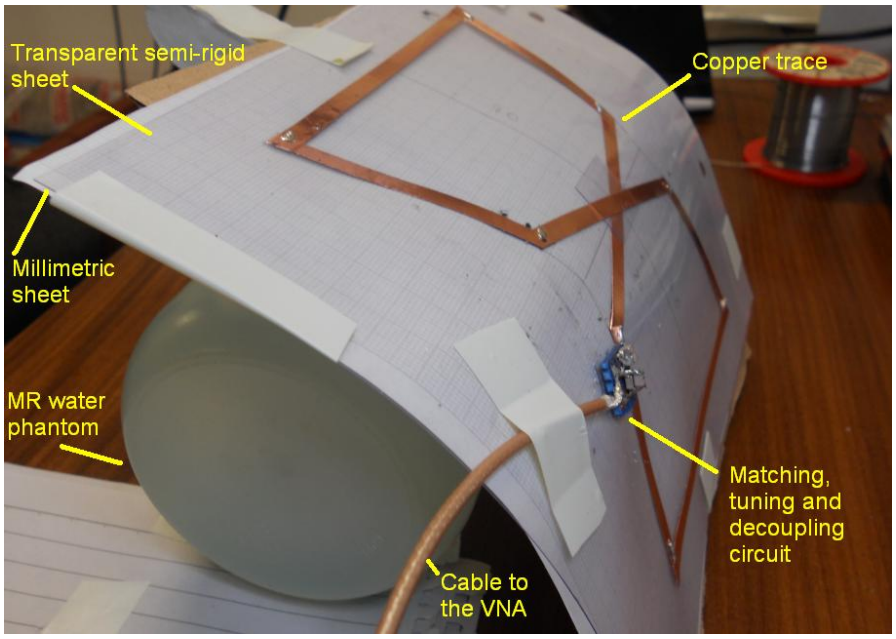
In Table 8.4 the final values of added capacitances and the electrical properties of each element are reported. Figure 8.20 shows S_{11} and S_{21} measurements for each element of the array. It can be observed that secondary resonance modes due to coupling between the elements were cancelled or minimized. The dashed red circle indicates remaining low amplitude second resonance peaks.

The resonance frequencies of the elements were slightly over-tuned because it was observed that a loading phantom simulating the anatomy would shift the resonance frequencies towards lower values by about 0.5 MHz. The values of the resonance frequencies are reported below each graph ($RefFreq$). For all the elements a value of S_{11} lower than -15 dB was achieved ($RefAmp$), which indicated good matching between an element and the coaxial cable.

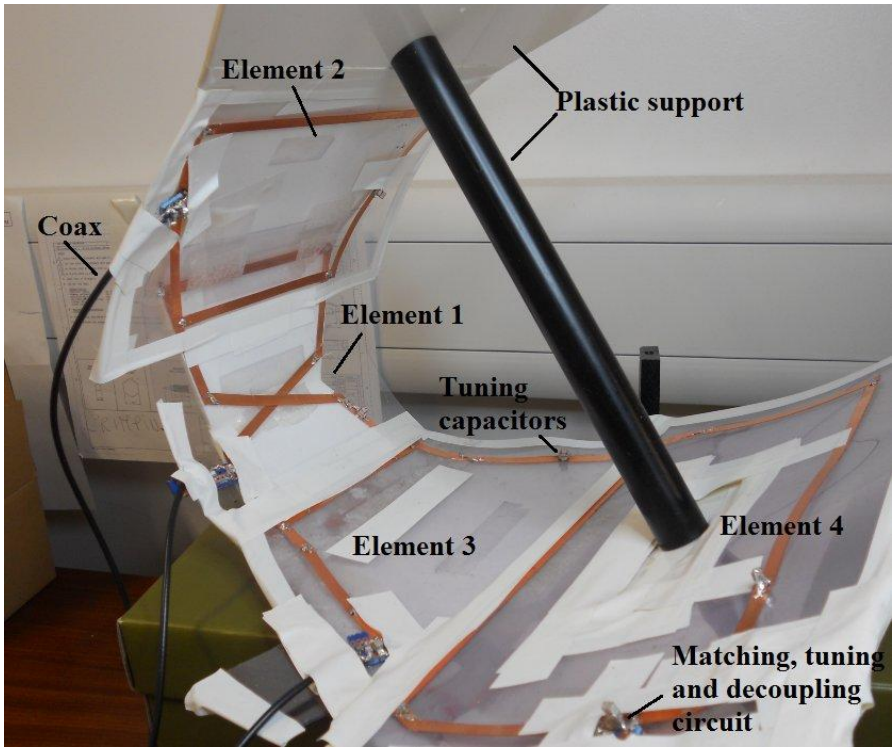
Figure 8.21 shows S_{21} measurements in reception and transmission stages. These results were obtained using L_d components of values 10 nH and the testing set up explained in Section 8.4.2. The reception stage corresponds to PIN diode off, while the transmission stage corresponds to PIN diode on. In reception, the PIN diodes are reverse biased and the elements resonates at the Larmor frequency. In transmission, the PIN diode is forward biased and the parallel L_dC_M is presented at the circuit. The elements are hence decoupled and the amplitude of the resonance peak decreases by at least 35 dB.

TABLE 8.4: Values of the electrical components and electrical properties of each element.

element	C_m	C_t	ν_0	$Q-factor$
1	230	10.9	64.1	75
2	240	9.4	64.7	82
3	240	14.7	64.4	80
4	220	12.4	64.5	85

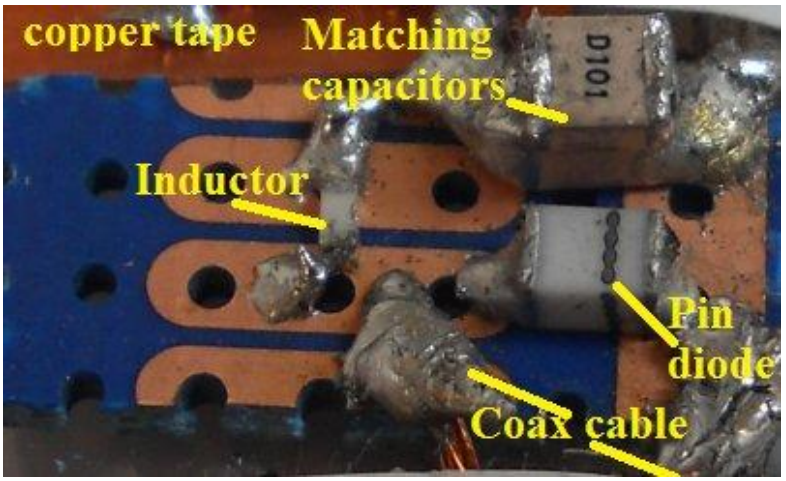


(a)

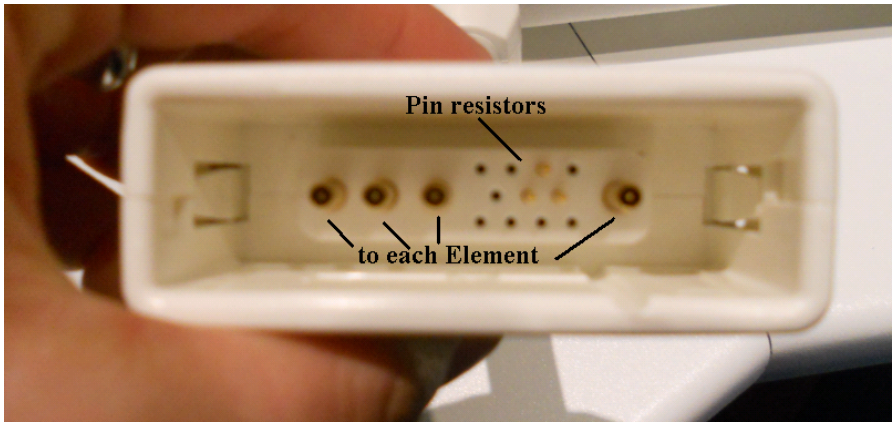


(b)

FIGURE 8.18: Coil manufacturing. (a) Manufacturing the butterfly element and (b) all element assembled.



(a)



(b)

FIGURE 8.19: Details of the receiver. (a) Matching, tuning and decoupling circuit at each element and (b) Connector interfacing the receiver to the MR Siemens Scanner.

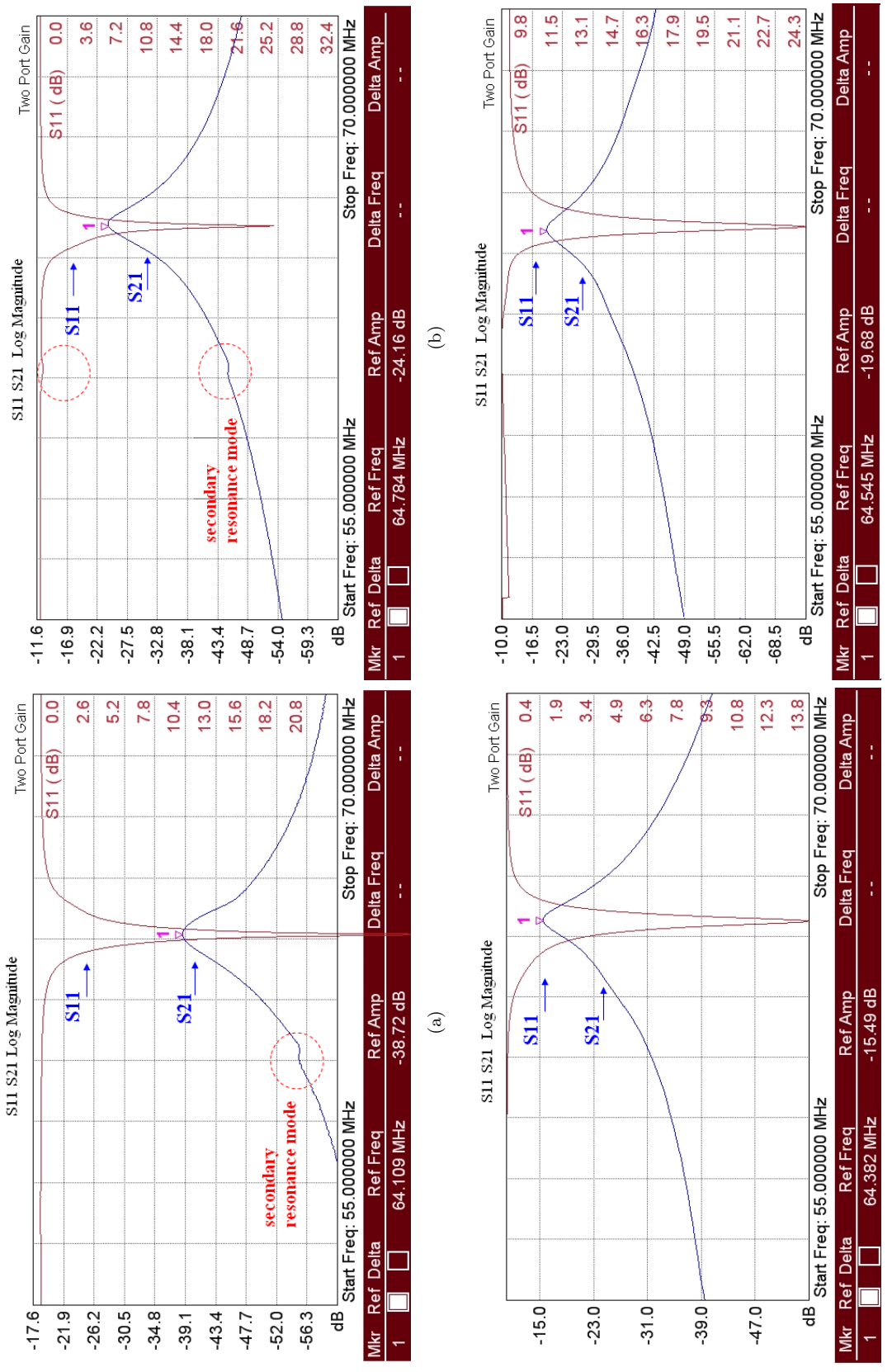


FIGURE 8.20: Response of each element. Measurements S_{11} and S_{21} for (a) Element 1, (b) Element 2, (c) Element 3, and (d) Element 4.

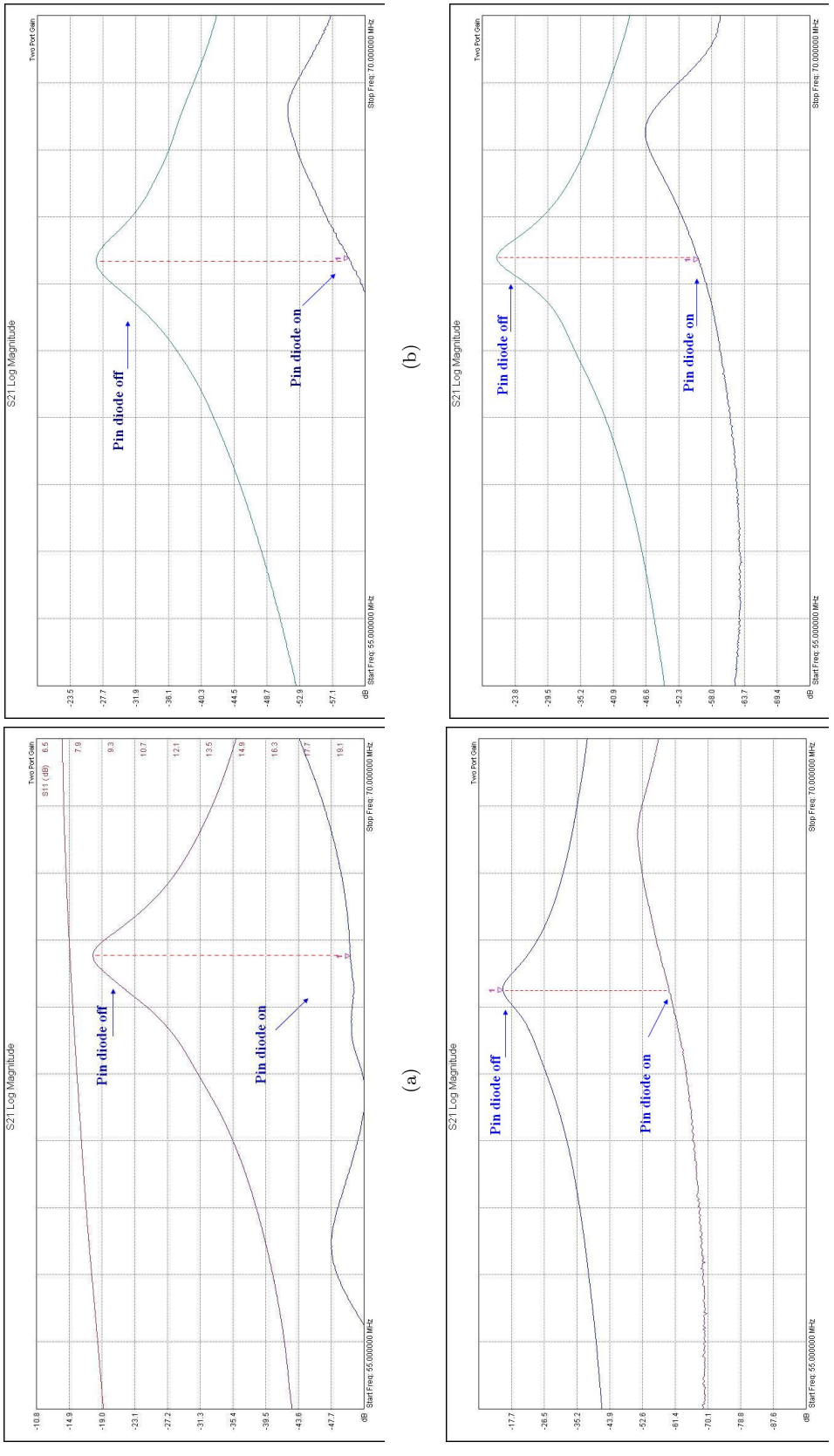


FIGURE 8.21: Response in transmission and reception stages. Measurements S_{21} for (a) Element 1, (b) Element 2, (c) Element 3, and (d) Element 4.

8.5.2 Results in the MR scanner

MR images were acquired in a 1.5 T Siemens Avanto MR Scanner. The body coil was used as transmitter. The proposed receiver was connected to a four-channel flex-interface of the scanner and positioned on the scanner table as shown in Figure 8.23. A large orange was used to represent the prostate. The orange was placed within at realistic distances from the elements by means of plastic supports and water phantom. A Turbo Spin Echo sequence was used and the parameters were set as in the scan protocol in Table 8.5. For comparison, MR images were also acquired using a standard coil positioned in as similar as possible to a realistic situation. Transversal cross-sections are shown in Figure 8.24; sagittal cross-sections are shown in Figure 8.25. The cross-sections were through the middle of the simulated prostate.

The signal-to-noise ratio (SNR) was calculated as ratio of the average signal over a selected uniform area of the prostate phantom and standard deviation of a selected area of the background [Constantinides et al., 2008]. The selected areas are outlined in Figure 8.25. The computed SNR is reported in Figure 8.28. It can be noticed that by using the proposed coil an improvement in signal-to-noise ratio of about 4 times was achieved.

Also, it can be noticed that the edges in the images acquired with the proposed receiver are generally more defined than in the images acquired using the standard coil. In order to further investigate the resolution of the signal, the tube phantom shown in Figure 8.22 was employed. The tube phantom comprises a cylindrical plastic container of internal diameter 67 mm and length 110 mm. This contains 10 plastic tubes of outer diameter 15 mm with wall thickness 1.4 mm. Three of these tubes lie within a larger plastic tube of outer diameter 36 mm and wall thickness 1.8 mm. The setup was as before, with the tube phantom placed horizontally instead of the orange and the water phantom removed. Results in transversal and sagittal planes are reported in Figures 8.26 and 8.27, respectively.

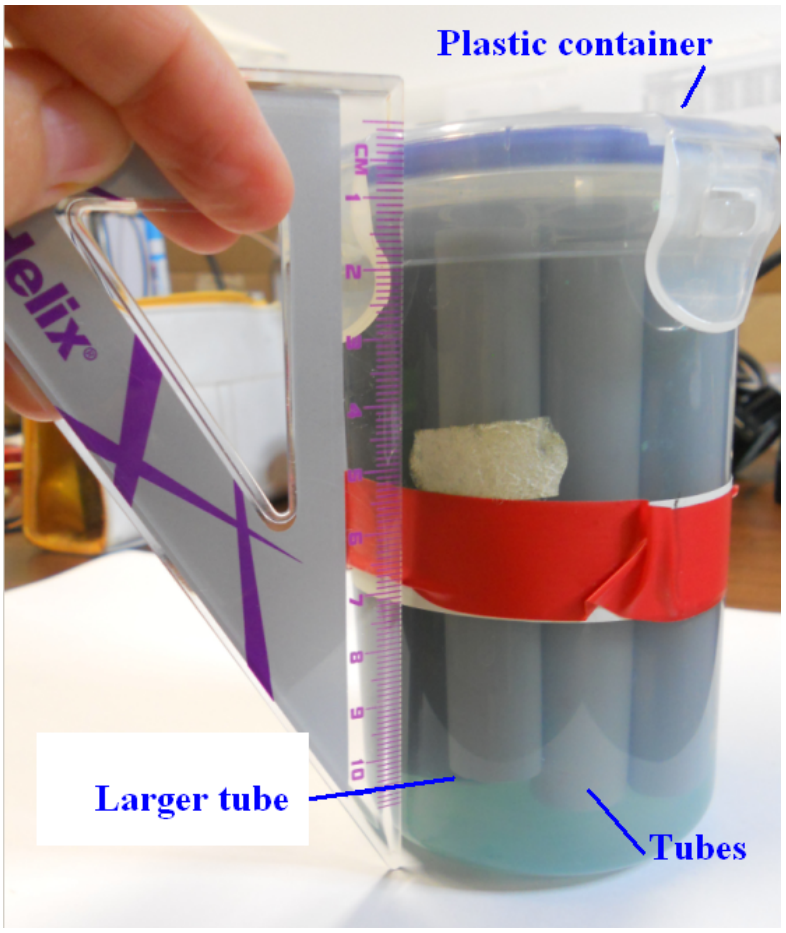


FIGURE 8.22: Tube phantom. The phantom comprises 10 plastic tubes of outer diameter 15 mm and wall thickness 14 mm. Three of them are within a larger tube of diameter 67 mm (black tube).

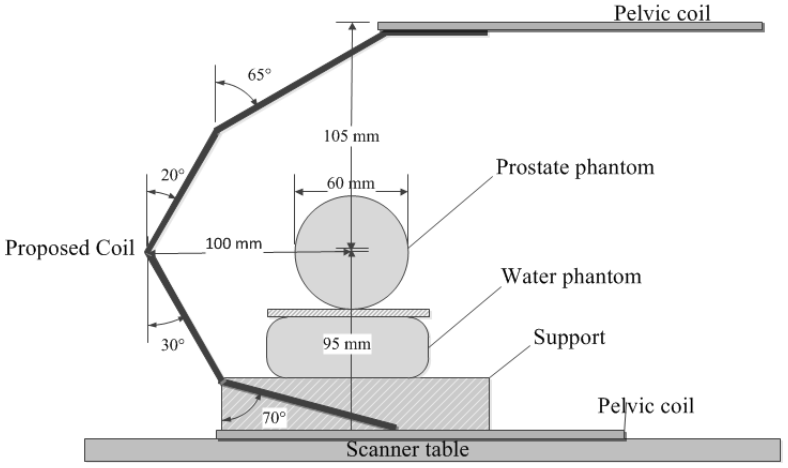


FIGURE 8.23: Setup of the proposed receiver in the MR scanner. An orange phantom represented the prostate; this was placed at realistic distances from the elements by using a plastic supports and a flat water phantom.

TABLE 8.5: Parameters of the sequence Turbo Spin Echo.

TR (ms)	3670
TE (ms)	121
Flip angle (°)	137
Slice thickness (mm)	3-5
Pixel spacing (mm)	0.688
Distance factor (%)	10
Turbo factor	23

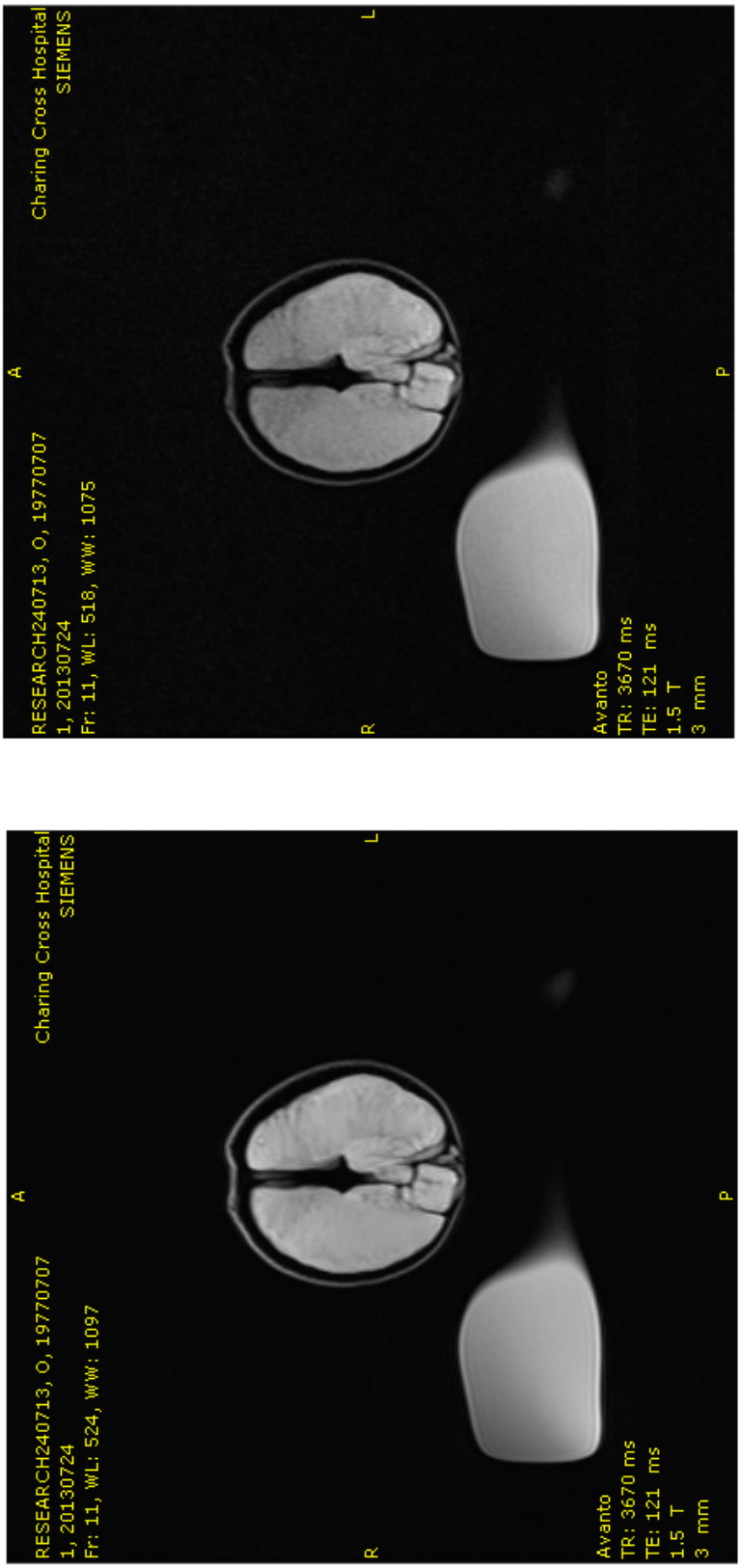


FIGURE 8.24: Transversal cross-section at the middle of the prostate phantom. (a) Proposed coil and (b) Standard pelvic coil.

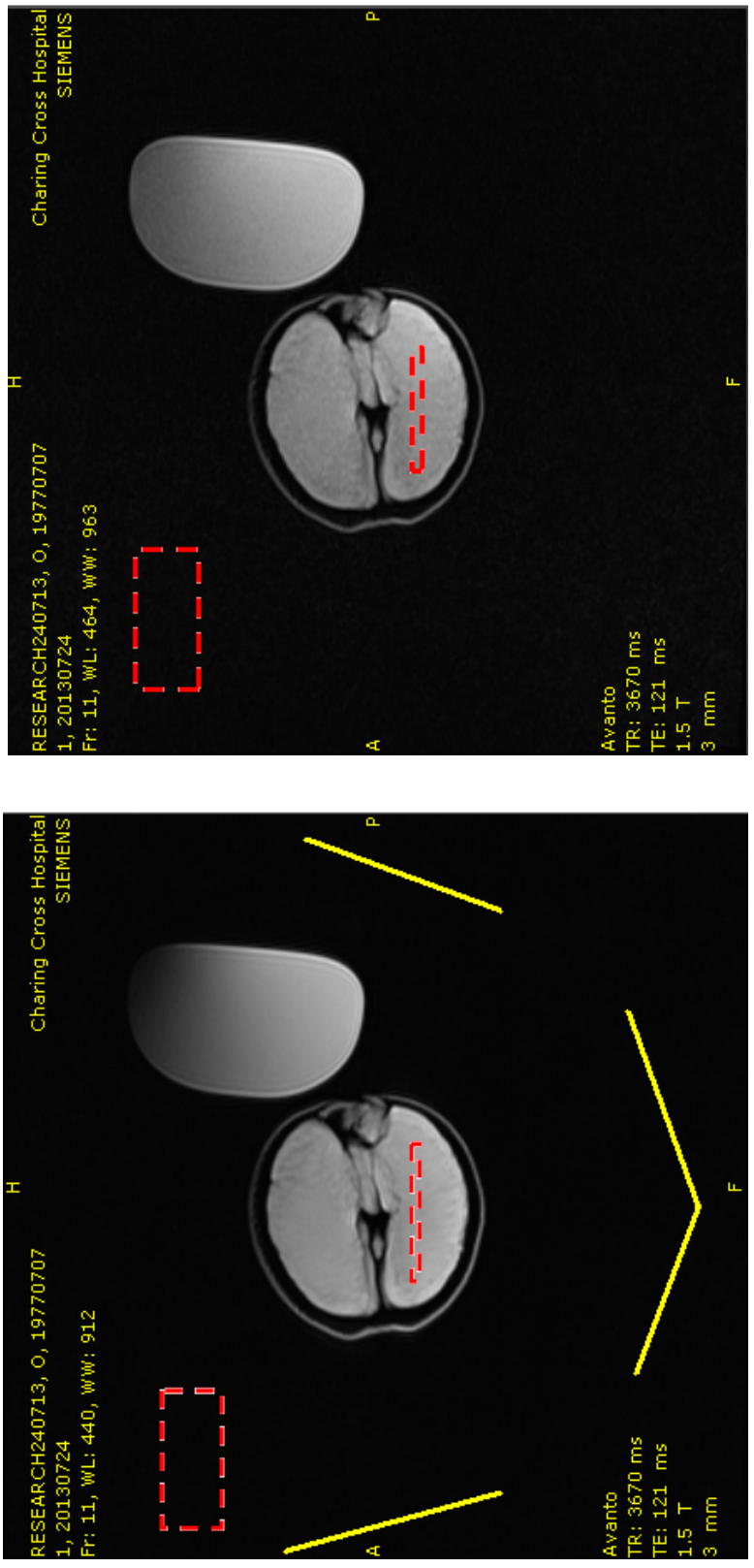


FIGURE 8.25: Sagittal cross-section at the middle of the prostate phantom. (a) Proposed coil and (b) Standard pelvic coil. The areas selected for computation of SNR are outlined. For clarity, the elements of the proposed coil are indicated (yellow segments).

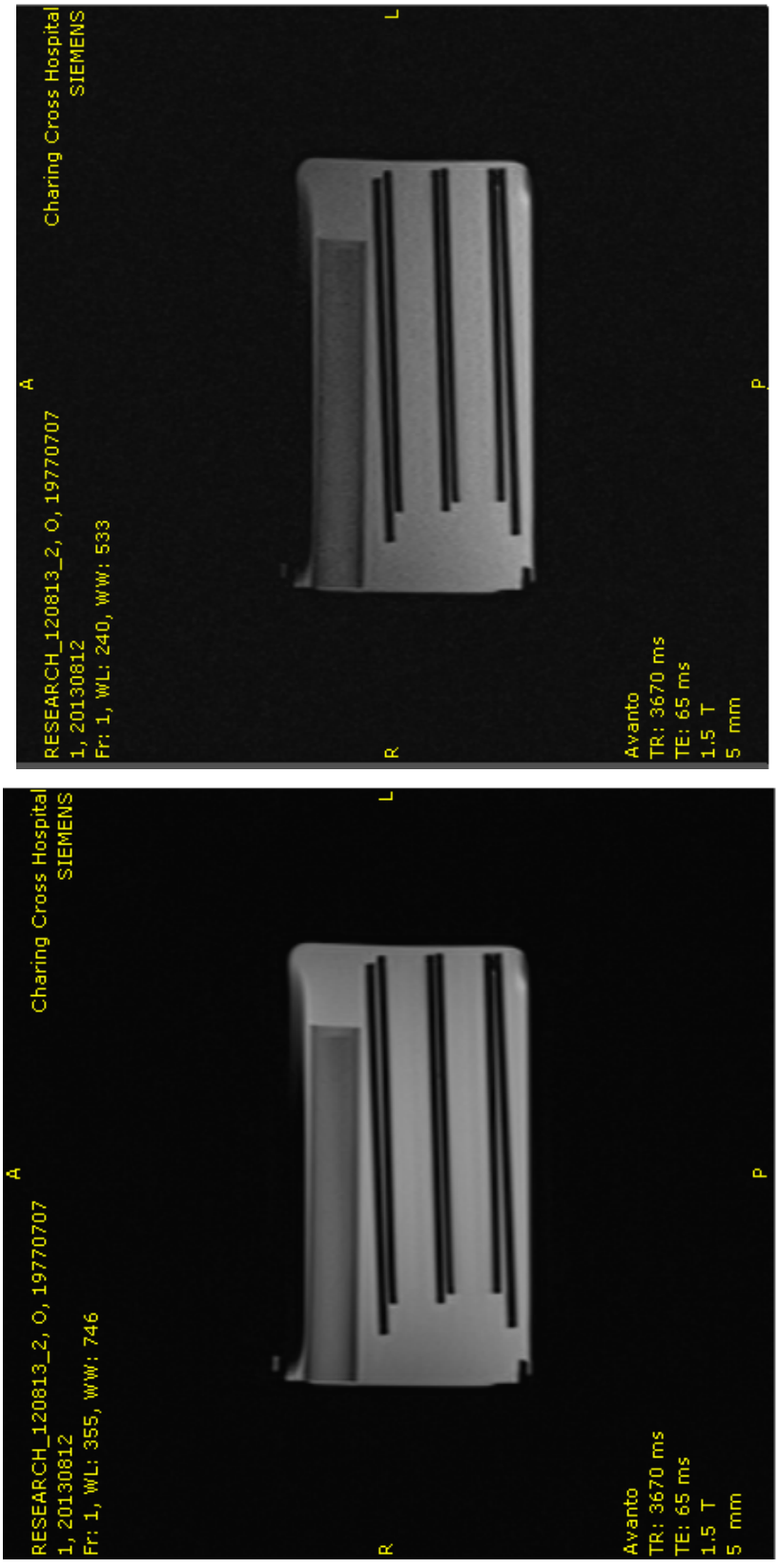


FIGURE 8.26: Transversal cross-section at the middle of the tubes phantom. (a) Proposed coil and (b) Standard coil.

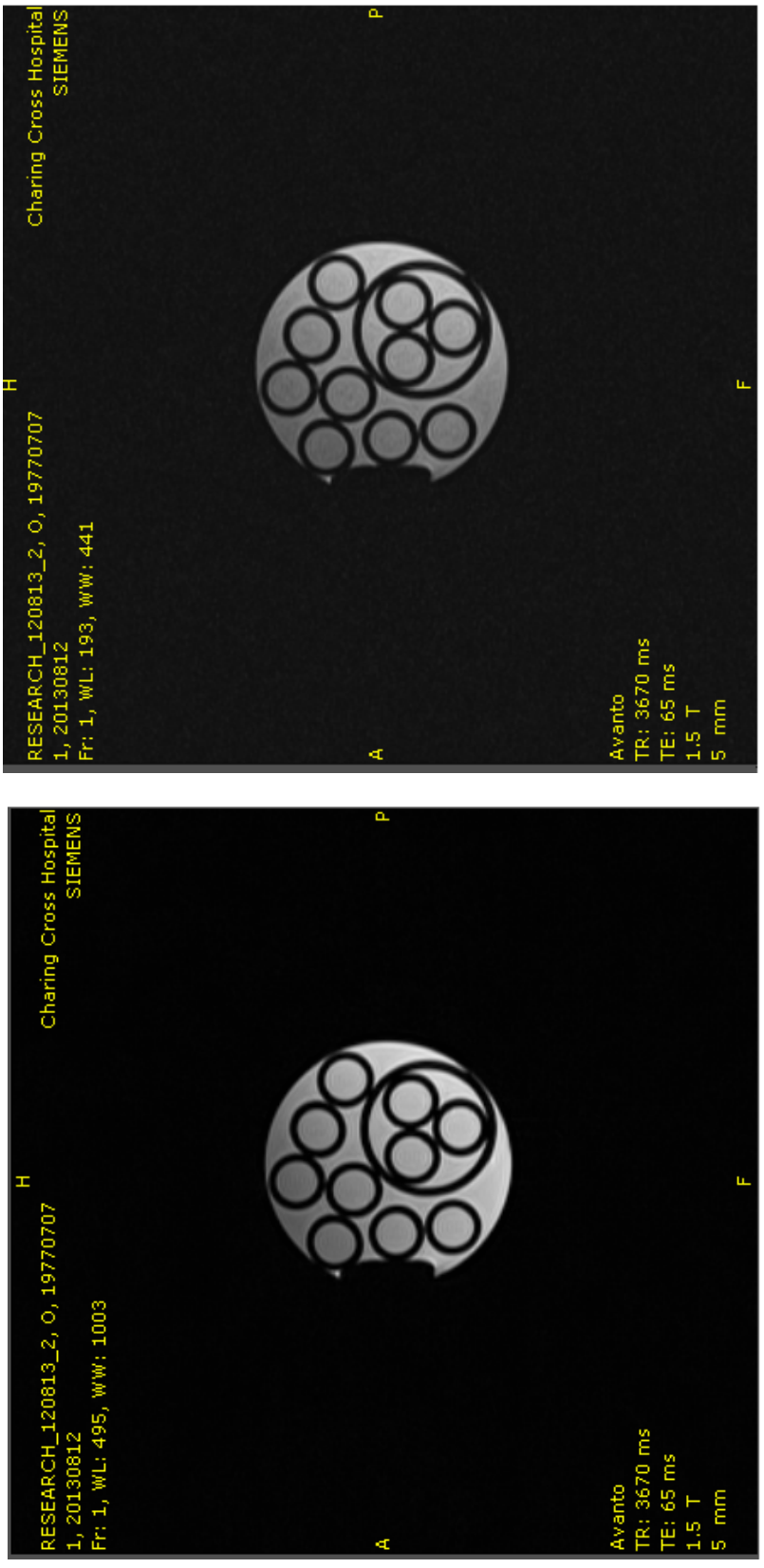


FIGURE 8.27: Sagittal cross-section at the middle of the tubes phantom. (a) Proposed coil and (b) Standard coil.

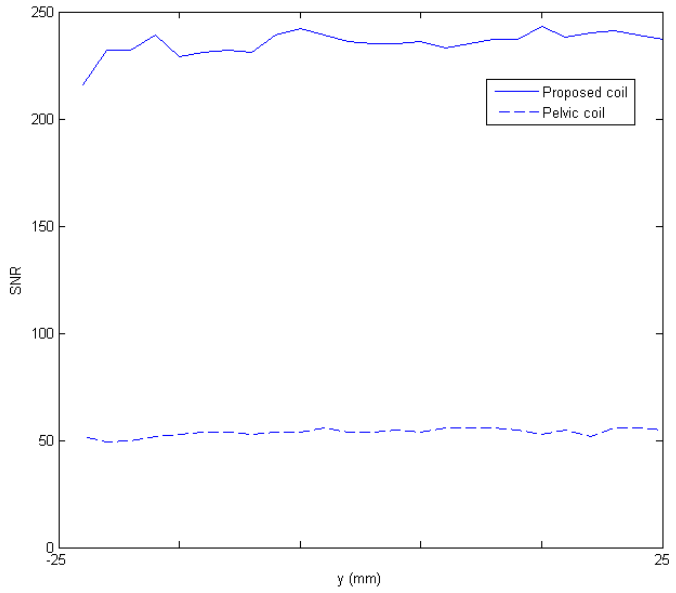


FIGURE 8.28: Signal to noise ratio. The ratio was computed for the outlined sections in the sagittal image and for both the coils.

8.6 Discussion and conclusions

This Chapter proposed a novel receiver design for imaging of the prostate while performing MRI-guided transrectal prostate biopsy intervention. The external array was designed based on the male pelvic anatomy and interventional requirements. The detector follows closely the outer contour of the body, so that higher-signal-to noise ratio is achieved, while it does not restrict mechanical movements of the manipulator and endorectal probe. In order to minimize the mutual coupling between neighbouring elements, partial overlapping of neighbouring coils and preamplifier decoupling were employed. Also, coupling of the array with the transmitter coil during RF excitation was minimized by employing passive detuning.

The proposed array and a standard pelvic array were compared in terms of sensitivity and homogeneity. Simulations showed that the magnetic field of the proposed coil is higher and more homogenous across the prostate. A prototype of the array was built and images of a prostate and tube phantom were acquired using a T_2-weighted TSE sequence. The proposed coil showed an improvement of the signal-to-noise-ratio of about four times and as a result the edges appeared more defined. These results suggest that the new design may be considered for novel detectors for imaging of the pelvic area, not only while performing prostate biopsy but also in diagnostic imaging. To this end, comparison of the proposed coil with a combination of pelvic and endorectal coil would be a next natural step.

Chapter 9

Conclusions and future work

The research presented in this thesis aimed to develop an optimized navigation system suitable for performing MRI-guided prostate biopsy. With this aim, the main objectives were identified to be a faster and more accurate localization of fiducial markers and instrument tracking, an optimized 3D graphical user interface for enhanced intra-operative image feedback, and an optimized receiver coil for improved intra-operative imaging of the suspect lesions. This Chapter outlines the achievements of the work and draws conclusions and proposals for future work.

9.1 Summary of the Achievements

9.1.1 Localization method

A novel, fast and accurate method for 3D localization of N fiducial markers using 1D projections was presented. The localization method may be employed to localize either active markers, when a single receiver channel is used, or semiactive markers. The localization method was validated using Monte Carlo simulations and experiments in 1.5 T and 2.9 T MR scanners. Sub-millimetre accuracy in localizing a marker was achieved by applying Gaussian interpolation in peak detection and by using an optimal set of reference projections to compute candidate points. A localization error better than 0.3 mm was achieved. The reliability of the method when markers move was also demonstrated and resulted in a maximum error equal to 0.7 mm for a speed anticipated during interventional procedures. The total update time, comprising acquisition of the set of 1D projections and computation, was equal to 73.7 ms, resulting in a total update rate of about 10 Hz.

9.1.2 Tracking method

A method for tracking the endorectal probe and biopsy needle in MRI-guided prostate biopsy was developed. Three semiactive markers were embedded within the probe in a known geometrical configuration and tracked by means of the proposed localization method. As the objective was to maximize the accuracy of the needle tip position, one of the markers was positioned as close to the probe tip as possible and all markers were placed reasonably far apart.

Localization of the probe and needle involved paired-point assignment of the measured points to the markers in a nominal model of the probe. The error introduced by the measurements was minimized by performing a rigid body transformation that minimizes the sum of the squared distances between the measured markers and the corresponding nominal markers. The transformation involved operations of translation and rotation, and was computed by using Singular Value Decomposition and at each update.

The targeting error when three markers were used was estimated to be smaller than 1 mm both in simulations and experiments using 2.9 T and 1.5 T MR scanners. A quantitative analysis performed using Monte Carlo simulations showed that by using 6 markers the maximum error is reduced to about 0.5 mm. It is important to underline that this analysis assumed that needle and probe were perfectly made and that there was no deflection of the needle during firing.

9.1.3 Graphical user interface

A novel 3D graphical user interface tailored for the specific application was implemented. Simplified models of the endorectal probe and biopsy needle, in a position after being fired, were superimposed onto three cross sections of the imaging volume and updated about 10 times per second. 3D display of the anatomical volume involved transverse and coronal planes, while a third plane was defined by the position of the manipulator's parallelogram mechanism and contained the probe and needle. Any of these planes may be selected by the user to be displayed or hidden.

The suggested targeting trajectory was visualized as the line connecting the remote-centre of the manipulator with the selected target. The remote-centre of motion of the manipulator was automatically computed only once at the start of the intervention. In addition, the high update rate of the localization method enabled implementation of a filtering technique. It was demonstrated that by implementing the simplest moving average filter, the fluctuations in the needle tip position can be significantly reduced.

9.1.4 Optimized receiver coil

A novel phased array receiver coil for high-quality intra-operative imaging of the prostate was designed. The prototype receiver coil array was designed to be close-fitting to the patient and wearable in a manner resembling a diaper. The coil included three trapezoidal loops tapered towards the z direction of the scanner and one butterfly coil in order to compensate for the orientation with the main magnetic field at the perineal body of the patient.

Simulations and experiments in a 1.5 T Siemens MR Scanner showed that the proposed receiver provides a significantly higher sensitivity and homogeneity over the prostatic area than a standard pelvic array coil. Acquired images of phantoms representative of the prostate showed an improvement of the SNR of about four times.

The receiver coil was meant to be employed in situ throughout the interventional procedure, for both anatomical imaging and tracking of the markers. However, as the development of the receiver coil was carried out in parallel with the development of the navigation workstation, the new receiver coil was not used in the tracking experiments. It is expected that the use of the new receiver array would further improve the SNR of the 1D projections, similarly to the demonstrated improvement in SNR when acquiring 2D images.

9.2 Discussion

In this work, semiactive markers were employed owing to their higher safety and flexibility. The miniature size of the constructed markers was such as to provide a good Q-factor while allowing for easy insertion of MR-visible material and easy fitting within small medical instruments (e.g. biopsy probe). The suitability of the markers for the clinical application was demonstrated in terms of signal amplitude in the presence of a person in the scanner, local heating and generated artefacts. The markers produced gradually less signal as the axis of the miniature solenoid was aligned with the main magnetic field; for angles higher than 60°, signal amplitude became comparable with the background noise. Such situation was avoided by designing a manipulator mechanism such that the axis of a coil is always perpendicular to the main field was employed. This solution did not introduce any limitation in the range of movements of the manipulator and avoided more complex approaches such as pairs of resonant fiducial markers [Kuehne et al., 2003].

It is important to underline that the success of the localization algorithm highly depends on the amplitude of the signal peaks against the background signal. As previously outlined, failure of the method may occur if a peak which does not correspond

to a marker is detected or if a peak which corresponds to a marker is not detected. In order to minimize these occurrences, markers should be accurately built and markers which are tracked simultaneously should have similar electrical properties, so that the parameters of the tracking sequence can be optimized for all of them at the same time. In this work, the markers were entirely built manually in order to achieve the desired high and reliable signal peaks. An improvement may be to employ spherical MR visible material rather than cubical; this would minimize inaccuracies introduced by the direction of projection.

An important result of the proposed localization method is that using 13 1D projections was shown to be optimal in terms of minimizing the localization error and maximizing the robustness, while the penalty in terms of computational time was insignificant. High update rate was achieved by using a pre-defined set of 1D projections and by avoiding cluster analysis [Flask et al., 2001]. Previously, Flask et al. [2001] achieved a computational time equal to 16 ms for three markers, while Krieger et al. [2005] reported a computational time equal to 50 ms. When 6 markers are used, the achieved computational time showed an improvement of up to a factor of 100 over existing solutions.

In the case when multiple markers are being localized, a limitation of the algorithm is that failure may occur in situations were due to symmetries peaks may merge in a number of projections. This may happen for some configurations of the fiducial markers and may be avoided by optimizing the set of the 13 projections and the fiducial configuration for the particular instrument design.

A fast update rate is essential in interventional procedures for several reasons. Firstly, it minimizes inaccuracies introduced by patient and instrument's movements. Secondly, it provides enhanced guidance of the medical instrument by allowing interleaving of tracking and visualization functionalities. Finally, it was demonstrated that by implementing even a simple moving average filter, the fluctuations in the needle tip position can be significantly reduced. The delay that was observed in a case of fast movement of the probe might be avoided by implementing more advanced filtering techniques such as the Kalman filter [Teukolsky et al., 1986].

The graphical user interface developed in this work was designed to meet the needs of the specific application that was considered. This resulted in a more natural and effective guidance than previously proposed such interfaces [Krieger et al., 2011] [Susil et al., 2006]. Further improvements of the visualization may be considered. The trajectory was computed under the assumption that the remote-centre was static during the entire procedure; however, it was noticed that the displayed probe and needle were sporadically slightly out of plane due to small movements of the remote-centre. This was attributed to a suboptimal stability of the manipulator. A solution to this issue

might be to compute and update the plane by using the three fiducial markers' coordinates only. A limitation of the graphical user interface is that it required an operator at the navigation workstation to control the display and to execute the various commands communicated by the clinician via microphones and speaker. A more efficient and less time-consuming way to carry out the procedure would be to set-up a voice recognition feature that allows the clinician to directly interact with the graphical user interface via voice commands. Overall, the graphical display may benefit from being implemented using c++, VTK or some other environment that is better suited than Matlab for real-time applications.

With regard to the general research aim, it can be concluded that the development of an optimized navigation system suitable for performing MRI-guided prostate biopsy has been successful and that the implemented components provide a basis for other applications in the area of MRI-guided intervention. Integration of the tracking method, visualization software, MR compatible manipulator and the hospital MRI system was completed to a pre-clinical level. The system was judged by the relevant clinical staff at the Royal Marsden Hospital (Institute of Cancer Research, Sutton, London, UK) to be compatible with the clinical needs.

Safety is a main requirement in interventional procedures and the use of semiactive markers for instrument tracking avoided safety hazards that may arise from cabling. Also, no significant rise in the temperature of the marker was observed when running imaging or tracking sequences. With regard to the safety of the positioning device, accidental firing of the needle was avoided by introducing the biopsy gun only when the probe was aligned with the target. Compatibility with anatomical imaging was also investigated and the artefacts generated by the marker closest to the probe tip were considered acceptable by the clinical staff.

The pre-clinical targeting trials were successfully performed and demonstrated the ability to complete the biopsy procedure inside the magnet, without the need to withdraw the scanner table from the magnet bore, a limitation common to many reported systems [Beyersdorff et al., 2005] [Engelhard et al., 2006] [Krieger et al., 2011]. The clinical staff quickly gained sufficient familiarity with the device and with the graphical user interface, such that trials with patients are now being planned. The time taken to complete a targeting procedure was about 5 minutes, lower than the time reported for previously proposed systems [Beyersdorff et al., 2005] [Engelhard et al., 2006] [Krieger et al., 2011]. The total procedure time was about 15 minutes, which is similar to the time needed for a standard TRUS procedure which lasts on average about 20 minutes. In terms of accuracy, the targeting error was estimated to be about 1 mm.

9.3 Suggestions for future research

The achievements of this thesis not only provide contributions to the MRI field but also a guide for future investigations. The major suggestions for future research are outlined below.

Further development work for the prototype receiver coil is necessary in order to allow patient trials. In the first instance this would involve the design and construction of an appropriate ergonomic casing that will enable it to be used comfortably and safely. The standard verification of safety in terms of potential heating during imaging must also be carried out. Following this, further work on improving the ergonomics and performance will probably be required. The coil will perform best if it is designed to provide a tight fit to the patient and this may be ensured through appropriate design and the choice of preferably soft materials for the casing. Ideally, the coil should also be flexible and adjustable to accommodate patients of different sizes. In this case, a method for adequate tuning of the coil in situ is needed.

In the current procedure, verification images are acquired only before and after firing the biopsy needle. If a movement of the lesion is observed, then the clinician interactively selects the new position of the target and the trajectory is automatically adjusted accordingly. A significant improvement to the navigation would be to introduce intra-operative target tracking. This would entail development of a fast and accurate imaging sequence for interleaving target and instrument tracking and development of a method for automatic target identification.

The interventional system was tested at a pre-clinical level. Additional issues are expected to arise in trials with patients, which did not arise in phantom trails. Pre-clinical trials were performed using anatomical models made of soft materials, while in a clinical case the actual properties of the real tissues may cause a deviation of the needle from the expected trajectory. This is an important issue which needs further detailed investigation. In addition, the suggested needle trajectory may be optimized to avoid nerves and other anatomical structure. Further detailed development work is also anticipated in relation to the probe itself. This may involve development of a fully reusable or a disposable probe. A reusable probe would be designed for easy cleaning and sterilization, as well as being fully waterproof. On the other hand, a disposable probe would be very attractive from the practical point of view. The main challenge here is seen to be the reproducibility and quality control in the manufacture of the in-built fiducial markers.

There are many other interventional procedures that would potentially benefit from the work presented in this thesis. While the graphical user interface was specific for the application, the tracking method, owing to its safety and flexibility, may be employed for accurate and fast instrument tracking in other delicate procedures such as ablations

or biopsies of lungs, breast or other organs. Also, the proposed coil design may be employed and optimized for diagnostic imaging of the male and female lower abdominal areas.

9.4 Outcomes of this research

F. Galassi, D. Brujic, M. Rea, M. Ristic. *3D fast and accurate tracking of* N *markers from 1D projections.* MAGMA Journal. *Revisions to be made.*

F. Galassi, J. McGinley, M. Ristic, N. Desouza and D. Brujic. *Design of a receiver array for MRI-guided transrectal prostate biopsy.* ISMRM, 2013.

M. Rea, D. McRobbie, F. Galassi, D. Brujic and M. Ristic. *Phase-Encoded Resonant Marker Identification and Tracking.* ISMRM, 2012.

F. Galassi, D. Brujic, M. Rea, P. Ferreira, N. Desouza and M. Ristic. *Quantification of the targeting error in MRI-guided biopsy using Monte Carlo simulations.* ESMRMB, 2012.

D. Brujic, F. Galassi, M. Rea, P. Ferreira, N. Desouza and M. Ristic. *Analysis of localisation accuracy of multiple wireless coils in interventional MRI*, 9th International Interventional MRI Symposium, 2012.

D. Brujic, F. Galassi, M. Rea, M. Ristic. *A novel algorithm for fast 3D localization of N fiducial markers from 1D projections.* ISMRM, 2012.

Appendix A

Derivation of the RF Signal

The RF signal acquired at each 1D projection is given by the transversal component of the magnetization vector at time TE:

$$M_{TE_{xy}} = \sqrt{M_{TE_x}^2 + M_{TE_y}^2} \tag{A.1}$$

In order to assess $M_{TE_{xy}}$ over a set of 1D projections, the evolution of the magnetization vector M over repeated RF pulses was formulated by applying matrix formalism.

The RF pulse causes nutation of the magnetization vector M about the x axis of an angle α. This effect might be represented by multiplication of the initial magnetization vector by the matrix $\mathbf{R}_\alpha$:

$$\mathbf{R}_\alpha = \begin{bmatrix} 1 & 0 & 0 \\ 0 & cos(\alpha) & sin(\alpha) \\ 0 & -sin(\alpha) & cos(\alpha) \end{bmatrix}.$$

Consequent to RF nutation, T_1 and T_2 relaxation processes occur. The components of the magnetization vector M at time t may be computed by applying Bloch equations [Hargreaves et al., 2001]:

$$M_z(t) = M_z(0)(1 - \exp(-\frac{t}{T_1})) \tag{A.2}$$

$$M_{xy}(t) = M_z(0)(1 - \exp(-\frac{t}{T_2})) \tag{A.3}$$

Therefore, relaxation over a period τ can be represented by a multiplication of M by the matrix C_τ, where

$$\mathbf{C}(\tau) = \begin{bmatrix} \exp(-\frac{\tau}{T_2}) & 0 & 0 \\ 0 & \exp(-\frac{\tau}{T_2}) & 0 \\ 0 & 0 & \exp(-\frac{\tau}{T_1}) \end{bmatrix}$$

and an addition of the vector

$$\mathbf{D}(\tau) = (\mathbf{I} - \mathbf{C}(\tau)) \begin{bmatrix} 0 \\ 0 \\ M_0 \end{bmatrix}.$$

It was found that using this formulation, the magnetization at the 1D projection k and just after the RF nutation is:

$$\mathbf{M}_{k_{aRF}} = \mathbf{R}_\alpha \mathbf{M}_k; \tag{A.4}$$

the magnetization at time TE is:

$$\mathbf{M}_{k_{TE}} = \mathbf{P}(TE)\mathbf{T}(TE)\mathbf{M}_{k_{aRF}} + \mathbf{D}(TE); \tag{A.5}$$

the magnetization at time TR just before the RF pulse is:

$$\mathbf{M}_{k_{TR}} = \mathbf{P}(TR - TE)\mathbf{C}(TR - TE)\mathbf{M}_{k_{TE}} + \mathbf{D}(TR - TE) \tag{A.6}$$

.

Assuming perfect spoiling, the transverse component of the magnetization vector is null just before each RF pulse. However, perfect spoiling is an ideal situation which is difficult to reach in practice and a spoiling factor s may therefore be introduced. In this case, at the next RF excitation (*k+1*), M_k in Equation A.4 becomes:

$$\mathbf{M}_{k+1} = \mathbf{M}_{k_{TR}} \begin{bmatrix} s \\ s \\ 1 \end{bmatrix}.$$

Appendix B

Magnetic Field Calculation

The magnitude of the magnetic field produced by a straight wire $\overrightarrow{AB}$ shown in Figure B.1 can be expressed as:

$$
\begin{aligned}
|\mathbf{B}| &= \frac{\mu_0 I}{4\pi}\int_A^B \frac{|d\mathbf{l}\times(\mathbf{r}-\hat{\mathbf{r}}')|}{|\mathbf{r}-\mathbf{r}'|^2} = \frac{\mu_0 I}{4\pi}\int_A^B \frac{cos\gamma|d\mathbf{l}|}{|\mathbf{r}-\mathbf{r}'|^2} \\
&= \frac{\mu_0 I}{4\pi}\int_{-\gamma_1}^{\gamma_2} \frac{(cos\gamma)^3\rho d\gamma}{(cos\gamma)^2\rho^2} = \frac{\mu_0 I}{4\pi\rho}\int_{-\gamma_1}^{\gamma_2} cos\gamma d\gamma \\
&= \frac{\mu_0 I}{4\pi\rho}(sin(\gamma_2)+sin(\gamma_1))
\end{aligned}
\tag{B.1}
$$

where $(\mathbf{r}-\mathbf{r}')$ is the distance from the current element $d\mathbf{l}$ to the field point P, ρ is the normal distance between P and the wire, γ_1 is the angle between r_a and ρ, and γ_2 is the angle between r_b and ρ. r_a and r_b are the distances from the point P to the two extreme points of the wire A and B, respectively.

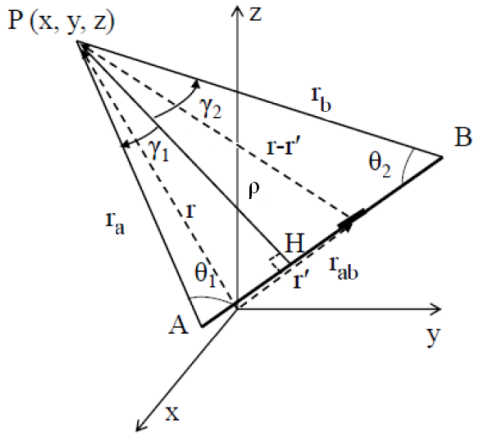


FIGURE B.1: Current-carrying wire arbitrarily oriented.

By applying the Law of Cosine [Pickover, 2009] to the triangle $P\hat{A}B$:

$$cos(\theta_1) = \frac{r_{ab}^2+r_a^2-r_b^2}{2r_{ab}r_a}; \quad cos(\theta_2) = \frac{r_b^2+r_{ab}^2-r_a^2}{2r_{ab}r_b} \tag{B.2}$$

and using the relation between *sine* and *cosine*

$$sin(\gamma_1) = sin(\tfrac{\pi}{2} - \theta_1) = cos(\theta_1); \quad sin(\gamma_2) = sin(\tfrac{\pi}{2} - \theta_2) = cos(\theta_2) \tag{B.3}$$

equation B.4 was expressed in terms of distance vectors:

$$|\mathbf{B}| = \frac{\mu_0 I}{4\pi}\left(\frac{r_{ab}^2 + r_a^2 - r_b^2}{2(r_{ab})(r_a)} + \frac{r_{ab}^2 + r_b^2 - r_a^2}{2(r_{ab})(r_b)}\right) \tag{B.4}$$

Since each element $\mathbf{I}d\mathbf{l}$ is a vector with the same direction as $\overrightarrow{r_{ab}}$, the direction of the magnetic field $\mathbf{B}$, e_B, generated by each element current at point P was obtained by computing the cross product of the vectors $\overrightarrow{r_a}$ and $\overrightarrow{r_{ab}}$ [Zhou et al., 2012]:

$$\mathbf{e_B} = \frac{\vec{r_a}\times\vec{r_{ab}}}{|\vec{r_a}\times\vec{r_{ab}}|} = \begin{vmatrix} \mathbf{e_x} & \mathbf{e_y} & \mathbf{e_z} \\ x_B - x_A & y_B - y_A & z_B - z_A \\ x_P - x_A & y_P - y_A & z_P - z_A \end{vmatrix} \tag{B.5}$$

which is equal to:

$$\frac{v_x}{\sqrt{v_x^2+v_y^2+v_z^2}}\mathbf{e_x} + \frac{v_y}{\sqrt{v_x^2+v_y^2+v_z^2}}\mathbf{e_y} + \frac{v_z}{\sqrt{v_x^2+v_y^2+v_z^2}}\mathbf{e_z} \tag{B.6}$$

with

$$\begin{aligned} v_x &= (y_B - y_A)(z_P - z_A) - (y_P - y_A)(z_B - z_A) \\ v_y &= (x_B - x_A)(z_P - z_A) - (x_P - x_A)(z_B - z_A) \\ v_z &= (x_B - x_A)(y_P - y_A) - (x_P - x_A)(y_B - y_A) \end{aligned} \tag{B.7}$$

Knowing the direction e_B, the three components of the magnetic field $\mathbf{B}$ were then computed as

$$\mathbf{B} = |\mathbf{B}|e_B = B_x\mathbf{e_x} + B_y\mathbf{e_y} + B_z\mathbf{e_z} = \frac{|\mathbf{B}|v_x}{\sqrt{v_x^2+v_y^2+v_z^2}}e_x + \frac{|\mathbf{B}|v_y}{\sqrt{v_x^2+v_y^2+v_z^2}}e_y + \frac{|\mathbf{B}|v_z}{\sqrt{v_x^2+v_y^2+v_z^2}}e_z$$

.

Bibliography

D. Beyersdorff, A. Winkel, B. Hamm, S. Lenk, S.A. Loening, and M. Taupitz. Mr imaging-guided prostate biopsy with a closed mr unit at 1.5 t: initial results. *Radiology*, 234(2):576–81, 2005.

K. Engelhard, H.P. Hollenbach, B. Kiefer, A. Winkel, K. Goeb, and D. Engehausen. Prostate biopsy in the supine position in a standard 1.5-t scanner under real time mr-imaging control using a mr-compatible endorectal biopsy device. *European Radiology*, 16(6):1237–1243, 2006. ISSN 0938-7994.

A. Krieger, II Iordachita, P. Guion, A.K. Singh, A. Kaushal, C. Menard, P.A. Pinto, K. Camphausen, G. Fichtinger, and L. L. Whitcomb. An mri-compatible robotic system with hybrid tracking for mri-guided prostate intervention. *IEEE Trans Biomed Eng*, 58(11):3049–60, 2011.

R.C. Susil, C. Menard, A. Krieger, J.A. Coleman, K. Camphausen, P. Choyke, G. Fichtinger, L.L. Whitcomb, C.N. Coleman, and E. Atalar. Transrectal prostate biopsy and fiducial marker placement in a standard 1.5t magnetic resonance imaging scanner. *J Urol*, 175(1):113–20, 2006.

A. De Oliveira, J. Rauschenberg, D. Beyersdorff, W. Semmler, and M. Bock. Automatic passive tracking of an endorectal prostate biopsy device using phase-only cross-correlation. *Magnetic Resonance in Medicine*, 59(5):1043–1050, 2008.

A. Krieger, R. C. Susil, C. Menard, J. A. Coleman, G. Fichtinger, E. Atalar, and L.L. Whitcomb. Design of a novel mri compatible manipulator for image guided prostate interventions. *IEEE Trans Biomed Eng*, 52(2):306–13, 2005.

G. Thormer, N. Garnov, M. Moche, J. Haase, T. Kahn, and H. Busse. Simultaneous 3d localization of multiple mr-visible markers in fully reconstructed mr images: proof-of-concept for subsecond position tracking. *Magn Reson Imaging*, 30(3):371–81, 2012.

C. Flask, D. Elgort, E. Wong, A. Shankaranarayanan, J. Lewin, M. Wendt, and J. L. Duerk. A method for fast 3d tracking using tuned fiducial markers and a limited

projection reconstruction fisp (lpr-fisp) sequence. *J Magn Reson Imaging*, 14(5):617–27, 2001.

G. Pompili, A. Munari, P. Rigamonti, and G. Cornalba. Mri anatomy of the anorectal region. In M. Tonolini and G. Maconi, editors, *Imaging of Perianal Inflammatory Diseases*, pages 9–19. Springer Milan, 2013.

H. Jarnum, L. Knutsson, M. Rundgren, R. Siemund, E. Englund, H. Friberg, and H. Larsson. Diffusion and perfusion {MRI} of the brain in comatose patients treated with mild hypothermia after cardiac arrest: A prospective observational study. *Resuscitation*, 80(4):425–430, 2009.

T. Henzler, G. Schmid-Bindert, S.O. Schoenberg, and C. Fink. Diffusion and perfusion {MRI} of the lung and mediastinum. *European Journal of Radiology*, 76(3):329 – 336, 2010.

P. Moore. Mri-guided congenital cardiac catheterization and intervention: the future? *Catheter Cardiovasc Interv*, 66(1):1–8, 2005.

K.J. Mortele, K. Tuncali, V. Cantisani, S. Shankar, E. vanSonnenberg, C. Tempany, and S.G. Silverman. Mri-guided abdominal intervention. *Abdom Imaging*, 28(6):756–74, 2003.

K. Reither, F. Wacker, J.P. Ritz, C. Isbert, C.T. Germer, A. Roggan, M. Wendt, and K.J. Wolf. [laser-induced thermotherapy (litt) for liver metastasis in an open 0.2t mri]. *Rofo*, 172(2):175–8, 2000.

S.L. Lee, M. Lerotic, V. Vitiello, S. Giannarou, K.W. Kwok, M. Visentini-Scarzanella, and G.Z. Yang. From medical images to minimally invasive intervention: Computer assistance for robotic surgery. *Computerized Medical Imaging and Graphics*, 34(1): 33–45, 2010.

H. Busse, R. Trampel, W. Grunder, M. Moche, and T. Kahn. Method for automatic localization of mr-visible markers using morphological image processing and conventional pulse sequences: feasibility for image-guided procedures. *J Magn Reson Imaging*, 26(4):1087–96, 2007.

C.H. Kuo and J.S. Dai. Robotics for minimally invasive surgery: A historical review from the perspective of kinematics. *International Symposium on History of Machines and Mechanisms, Proceedings of Hmm 2008*, pages 337–354, 2009.

A. Jemal, F. Bray, M.M. Center, J. Ferlay, E. Ward, and D. Forman. Global cancer statistics. *CA: A Cancer Journal for Clinicians*, 61(2):69–90, 2011.

J.A. Lane, F.C. Hamdy, A. Martin, E.L. Turner, D.E. Neal, and J.L. Donovan. Latest results from the {UK} trials evaluating prostate cancer screening and treatment: The {CAP} and protect studies. *European Journal of Cancer*, 46(17):3095 – 3101, 2010.

A.M.D. Wolf, R.C. Wender, R.B. Etzioni, I.M. Thompson, A.V. D'Amico, R.J. Volk, D. Brooks, C. Dash, I. Guessous, K. Andrews, C. DeSantis, and Robert A. Smith. American cancer society guideline for the early detection of prostate cancer: Update 2010. *CA: A Cancer Journal for Clinicians*, 60(2):70–98, 2010.

R.C. Susil, A. Krieger, J.A. Derbyshire, A. Tanacs, L.L. Whitcomb, G. Fichtinger, and E. Atalar. System for mr image-guided prostate interventions: canine study. *Radiology*, 228(3):886–94, 2003.

J.C. Presti. Prostate cancer: assessment of risk using digital rectal examination, tumor grade, prostate-specific antigen, and systematic biopsy. *Radiol Clin North Am*, 2000.

M.C. Terris. Sensitivity and specificity of sextant biopsies in the deection of prostate cancer. *Urology*, 1999.

A. Krieger, C. Csoma, II Iordachital, P. Guion, A. K. Singh, G. Fichtinger, and L.L. Whitcomb. Design and preliminary accuracy studies of an mri-guided transrectal prostate intervention system. *Med Image Comput Comput Assist Interv*, 10(Pt 2): 59–67, 2007.

M. Moche, R. Trampel, T. Kahn, and H. Busse. Navigation concepts for mr image-guided interventions. *Journal of Magnetic Resonance Imaging*, 27(2):276–291, 2008.

G. Fichtinger, P. Kazanzides, A.M. Okamura, G.D. Hager, L.L. Whitcomb, and R.H. Taylor. Surgical and interventional robotics: Part ii: Surgical cad-cam systems. *IEEE Robot Autom Mag*, 15(3):94–102, 2008.

N. Garnov, G. Thormer, R. Trampel, W. Grunder, T. Kahn, M. Moche, and H. Busse. Suitability of miniature inductively coupled rf coils as mr-visible markers for clinical purposes. *Med Phys*, 38(11):6327–35, 2011.

J. Rachinger, B. von Keller, O. Ganslandt, R. Fahlbusch, and C. Nimsky. Application accuracy of automatic registration in frameless stereotaxy. *Stereotact Funct Neurosurg*, 84(2-3):109–17, 2006.

Q. Zhang, M. Wendt, A. J. Aschoff, L. Zheng, J. S. Lewin, and J. L. Duerk. Active mr guidance of interventional devices with target-navigation. *Magn Reson Med*, 44(1): 56–65, 2000.

S. Patil, O. Bieri, P. Jhooti, and K. Scheffler. Automatic slice positioning (asp) for passive real-time tracking of interventional devices using projection-reconstruction imaging with echo-dephasing (pride). *Magn Reson Med*, 62(4):935–42, 2009.

UPMC Cancer Center. Cancer information. Technical report, University of Pittsburgh Cancer Institute, 2013.

B.N. Bloch, N.M. Rofsky, R.H. Baroni, R.P. Marquis, I. Pedrosa, and R.E. Lenkinski. 3tesla magnetic resonance imaging of the prostate with combined pelvic phased-array and endorectal coils: Initial experience. *Academic Radiology*, 11(8):863 – 867, 2004.

N. DeSouza and D. Gilderdale. A solid reusable endorectal receiver coil for magnetic resonance imaging of the prostate: design, use and comparison with an inflatable endorectal coil. Technical report, Robert Steiner Magnetic, Royal postgraduate medical school, London UK, 1996.

H. Elhawary, Z.T.H. Tse, M. Rea, A. Zivanovic, Brian L. Davies, C. Besant, N. de Souza, D. McRobbie, I. Young, and M. Lamperth. Robotic system for transrectal biopsy of the prostate: Real-time guidance under mri. *Engineering in Medicine and Biology Magazine, IEEE*, 29(2):78–86, 2010.

N. Lambert, M. Ristic, and N. Desouza. Design of a novel device for mri guided transrectal prostate biopsy. In *The 9th International MRI Symposium*, 2012.

J.P. Hornack. *The basic of MRI.* nc, 1996.

D. McRobbie. *MRI from Picture to Proton.* 2003.

M. Brown. *MRI: Basic principles and applications.* John Wiley and Sons, 2005.

S.R. Deans and S. Roderick. The radon transform and some of its applications. ..., 1983.

Wertherner. *Siemens ice programming manual.* Siemens Medical Solutions, 2006.

Zwanger. *Siemens idea programming manual.* Siemens Medical Solutions, 2006.

F. Terman. *Radio Engineers' Handbook.* NewYork and London, 1943.

H. Fujita, T. Zheng, X. Yang, M. Finnerty, and S. Handa. Rf surface receive array coils: The art of an lc circuit. *Journal of Magnetic Resonance Imaging*, 38(1):12–25, 2013.

P.B. Roemer. The nmr phased array. *Magnetic Resonance in Medicine1990*, 1990.

D.J. Hoult. The nmr receiver: A description and analysis of design. *Progress in NMR Spectroscopy*, 1978.

V. Taracila, K. Shet, and F. Robb. Preamp decoupling - eigenvalue solution approach. In *Proc. Intl. Soc. Mag. Reson. Med.*, 2008.

M. Rea, D. McRobbie, H. Elhawary, Z. Tse, M. Lamperth, and I. Young. Sub-pixel localisation of passive micro-coil fiducial markers in interventional mri. *Magnetic Resonance Materials in Physics Biology and Medicine*, 22(2):71–76, 2009.

K. Cleary and T.M. Peters. Image-guided interventions: technology review and clinical applications. *Annu Rev Biomed Eng*, 12:119–42, 2010.

Available from: http://www.macmillan.org.uk/. How prostate cancer is diagnosed.

R. Cormack and A. D'amico. Feasibility of transperineal prostate biopsy under interventional magnetic resonance guidance. *Urology*, 2000.

C. Tempany and A. D'amico. Transperineal magnetic resonance image guided prostate biopsy. *Urology*, 2000.

S.P. Di Maio and G.S. Fisher. A system for mri-guided prostate interventions. *International conference on biomedical robotics and biomechatronics*, 2006.

Transrectal prostatic ultrasound and biopsy. Technical report, 2012.

M. Wendt and F.K. Wacker. Visualization, tracking, and navigation of instruments for magnetic resonance imaging-guided endovascular procedures. *Top Magn Reson Imaging*, 11(3):163–72, 2000.

R.J. Maciunas, Jr. Galloway, R.L., J.M. Fitzpatrick, V.R. Mandava, C.A. Edwards, and G.S. Allen. A universal system for interactive image-directed neurosurgery. *Stereotact Funct Neurosurg*, 58(1-4):108–13, 1992.

R. Khadem, C.C. Yeh, M. Sadeghi-Tehrani, M. R. Bax, J.A. Johnson, J.N. Welch, E.P. Wilkinson, and R. Shahidi. Comparative tracking error analysis of five different optical tracking systems. *Comput Aided Surg*, 5(2):98–107, 2000.

S. Schmerber and F. Chassat. Accuracy evaluation of a cas system: laboratory protocol and results with 6d localizers, and clinical experiences in otorhinolaryngology. *Comput Aided Surg*, 6(1):1–13, 2001.

S.P. DiMaio, S. Pieper, K. Chinzei, N. Hata, S.J. Haker, D. F. Kacher, G. Fichtinger, C.M. Tempany, and R. Kikinis. Robot-assisted needle placement in open mri: system architecture, integration and validation. *Comput Aided Surg*, 12(1):15–24, 2007.

H.F.M. Smits, C. Bos, R. van der Weide, and C.J.G. Bakker. Interventional mr: vascular applications. *Eur Radiol*, 9(8):1488–1495, 1999.

R.A. Omary, O. Unal, D.S. Koscielski, R. Frayne, F.R. Korosec, C.A. Mistretta, C.M. Strother, and T.M. Grist. Real-time mr imaging-guided passive catheter tracking with use of gadolinium-filled catheters. *J Vasc Interv Radiol*, 11(8), 2000.

J.H. Seppenwoolde, M.A. Viergever, and C.J.G. Bakker. Passive tracking exploiting local signal conservation: The white marker phenomenon. *Magnetic Resonance in Medicine*, 50(4):784–790, 2003.

C.L. Dumoulin, S.P. Souza, and R.D. Darrow. Real-time position monitoring of invasive devices using magnetic resonance. *Magn Reson Med*, 29(3):411–5, 1993.

M.K. Konings, L.W. Bartels, H.F. Smits, and C.J. Bakker. Heating around intravascular guidewires by resonating rf waves. *J Magn Reson Imaging*, 12(1):79–85, 2000.

M. Burl, G.A. Coutts, and I.R. Young. Tuned fiducial markers to identify body locations with minimal perturbation of tissue magnetization. *Magn Reson Med*, 36(3):491–3, 1996.

Q. Zhang, M. Wendt, A. J. Aschoff, J. S. Lewin, and J. L. Duerk. A multielement rf coil for mri guidance of interventional devices. *J Magn Reson Imaging*, 14(1):56–62, 2001.

R. Luechinger, F. Duru, V.A. Zeijlemaker, M.B. Scheidegger, R. Candinas, and P. Boesiger. Heating effects of magnetic resonance imaging of the brain on pacemaker leads: Send/receive coils versus receive-only coils. *Journal of the American College of Cardiology*, 37(2):436a–436a, 2001.

ASTM. Standard test method for measurement of radio frequency induced heating on or near passive implants during magnetic resonance imaging. Technical report, 2011.

H. Tadayyon, A. Lasso, A. Kaushal, P. Guion, and G. Fichtinger. Target motion tracking in mri-guided transrectal robotic prostate biopsy. *IEEE Trans Biomed Eng*, 58(11): 3135–42, 2011.

B.A. Hargreaves, S.S. Vasanawala, J.M. Pauly, and D.G. Nishimura. Characterization and reduction of the transient response in steady-state mr imaging. *Magn Reson Med*, 46(1):149–58, 2001.

M. Bernstein, K. King, and Z. Zhou. *Handbook of MRI pulse sequences*. Academic Press, Amsterdam ; Boston, 2004.

R.B. Fisher and D.K. Naidu. A comparison of algorithms for subpixel peak detection. *Image Technology, Advances in Image Processing, Multimedia and Machine Vision*, 1996.

Saul A. Teukolsky, W.T. Vetterling Vetterling, and B.P. Flannery. *Numerical Recipes: The Art of Scientific Computing*. Cambridge University Press, 1986.

J.M. Utts and R. F. Heckard. *Statistical ideas and methods*. Thomson-Brooks/Cole, Belmont, CA, 2006.

J.F. Schenck. The role of magnetic susceptibility in magnetic resonance imaging: Mri magnetic compatibility of the first and second kinds. *Med Phys*, 23(6):815–50, 1996.

A.S. Glassner. *Graphic gems*. Academic Press, 1998.

J. Toriwaki and H. Yoshida. *Fundamentals of three-dimensional digital image processing*. New York: Springer, Belmont, CA, 2009.

R.R. Shamir, L. Joskowicz, and Y. Shoshan. Fiducial optimization for minimal target registration error in image-guided neurosurgery. *Medical Imaging, IEEE Transactions on*, 31(3):725–737, 2012.

A. Bjorck. *Numerical Methods for Least Squares Problems*, volume I. Society for Industrial and Applied Mathematics, 1996.

K. Arun, T. Huang, and S. Blostein. Least-squares fitting of two 3-d point sets. *IEEE transactions on pattern analysis and machine intelligence*, 9(5):698–700, 1987.

D.F. Rogers and J.A. Adams. *Mathematical Elements for Computer Graphics*. 1989.

Available from: http://users.forth net.gr/ath/mkanell. Sante dicom viewer software.

S. Di Luzio, G. Placidi, S. Di Giuseppe, M. Alecci, and A. Sotgiu. A novel, cylindrical, transverse gradient coil design for magnetic resonance imaging of large samples. *Meas. Sci. Technol.*, 9:16631671, 1998.

A. Kumar and P. Bottomley. Optimized quadrature surface coil designs. *Magnetic Resonance Materials in Physics, Biology and Medicine*, 21(1-2):41–52, 2008.

Available from: http://www.fastfieldsolvers.com/. Fast field solvers software.

P. Russer. *Electromagnetics, Microwave Circuit, and Antenna Design for Communications Engineering*. Artech House, 2006.

R. Blum and D. Roller. *Electricity, Magnetism and Light*. Holden Day, 1981.

R.J. Kimple, E.M. Wallen, R. Pruthi, and L.B. Marks. A simple algorithm to assess patient suitability for calypso-seed implantation for four-dimensional prostate localization. *Journal of applied clinical medical physics*, 11(1), 2010.

C.D. Constantinides, E. Atalar, and E.R. McVeigh. Signal-to-noise measurements in magnitude images from nmr phased arrays. *Constantinides, C.D. and Atalar, E. and McVeigh, E.R.*, 52:219, 2008.

T. Kuehne, R. Fahrig, and K. Butts. Pair of resonant fiducial markers for localization of endovascular catheters at all catheter orientations. *Journal of Magnetic Resonance Imaging*, 17(5):620–624, 2003. doi: 10.1002/jmri.10307.

C.A. Pickover. *The Math Book: From Pythagoras to the 57th Dimension, 250 Milestones in the History of Mathematics*. Sterling Publishing Company, 2009.

Y. Zhou, X. Changhan, H. Wang, and Y. Zhou. The calculation of the magnetic field produced by an arbitrary shaped current-carrying wire in its plane. *Advances in Intelligent Systems Research*, 2012.